Investigating the Effect of Active Wheel Positioning to Develop Efficient Power Saving Solutions

Author

Johan Samuel Frederik (Janu) Botha

Submitted in partial fulfilment of the requirements for the degree

Master's in Mechanical Engineering

In the

Faculty of Engineering, Built Environment and Information Technology (EBIT)

At the

University of Pretoria

Student Number

U15007759

Date

June 2021

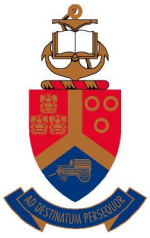

UNIVERSITEIT VAN PRETORIA
UNIVERSITY OF PRETORIA
YUNIBESITHI YA PRETORIA

vdg
Vehicle Dynamics Group

Abstract

Title: Investigating the Effect of Active Wheel Positioning to Develop Efficient Power Saving Solutions

Author: Johan Samuel Frederik Botha

Study Leader: dr. H.A. Hamersma

Department: Mechanical and Aeronautical Engineering, University of Pretoria

Degree: Master of Engineering (Mechanical Engineering)

With the growing popularity of electrically propelled vehicles, the demand has reached fever pitch. Thus, the emphasis on power saving techniques such as the possibility of saving power by actively controlling the camber angle of a vehicle, in combination with the conventional steering control of the vehicle. This study sets out to investigate the probability of using an active wheel control method to reduce the energy losses of the vehicle, without compromising the lateral dynamics of the vehicle. The active wheel control is achieved by continuously adjusting the slip angle and the camber angle of the wheels, instead of only using the traditional steering methods. Although this solution will not be the direct answer to increasing the range between recharges of an electric vehicle, it is expected that there exists a possibility to reduce the energy losses in the vehicle's tyres, which could reduce the power required to steer the vehicle, due to smaller steering inputs being required. In combination with all the systems in an electric vehicle, there exists a great potential for reducing power losses.

The aim of the camber control system is to minimise the energy losses in the vehicle, without compromising the vehicles dynamic behaviour. Therefore, the investigation will set out to determine the plausibility of camber control as a modern control system, that can assist electric vehicles to reduce the energy consumed to overcome the tyre loads during cornering.

The study sets out to investigate and fully understand the behaviour of a tyre under various slip and camber angles. To understand the behaviour of the tyre under various conditions, one should first understand the tyre being investigated. To represent the behaviour of the tyre in real world conditions, a fully validated FTyre tyre model of a Pirelli Scorpion SUV tyre is used. The tyre was validated by **Wright (2017)**. By using a tyre model to simulate the behaviour of a tyre under

real world conditions, is a cost-effective and efficient method to understand how the tyre will behave.

The camber control investigation started as a simple tyre simulation on the tyre drum test rig. These tests simulate the tyre on an artificial rolling road (drum road). The tyre slip angle, camber angle and vertical applied loads are varied to produce a clear understanding of the behaviour of the tyre.

The simulation results on the drum test rig demonstrates that a considerable energy loss reduction is present with the addition of camber angle on a single tyre. The results show that for the two different vertical load cases considered, $F_z = 3000N$ and $F_z = 6400N$ respectively, at selected lateral loads, a power loss reduction of 56.18% for load case 1 and 37.77% for load case 2 is observed. The two cases are the extreme cases with a slip angle of up to 15° and a camber angle up to -8 °. Based on these findings for a single tyre, it was determined that the investigation can be extended to full-vehicle simulations. From the simple tyre simulations, the focus was shifted to full vehicle simulations with a non-linear driver model, developed by **Botha (2011)**.

The study includes ADAMS/View multibody dynamics full-vehicle model, that will be used throughout the study to develop a mathematical control system, to actively change the camber angle. Full vehicle simulations are conducted on a fully validated MSC ADAMS vehicle model. The model is based on the Land Rover Defender 110Tdi at the Vehicle Dynamics Group (VDG). The full-vehicle model is adapted for camber control and cross validated with experimental data. Full vehicle simulations of Double Lane Change (DLC) and Constant Radius (CR) tests were conducted.

The full-vehicle simulations were used to help develop a camber controller that can actively control the camber angle of the vehicle during various handling manoeuvres. The design of this simple camber controller was based on the optimal relationship between the lateral acceleration of the vehicle and the camber angle, which yielded the greatest reduction in the energy losses in the tyres. The control method analysis the lateral acceleration of the vehicle during any dynamic driving manoeuvre and outputs the optimal camber angle that all four wheels should be. This is actively controlled during an entire dynamic manoeuvre.

The results from the simulations with the full-vehicle camber model showed that for both a CR test and a DLC manoeuvre, the friction power in the tyre can be reduced, by using camber control in addition to traditional steering control methods. For the CR test it was found that for a 13 second simulation, the total friction energy on all four wheels was reduced by $1830J$, with a percentage reduction of 4.63%. For the DLC manoeuvre, the total friction energy on all four wheels showed a $518.23J$ reduction in the friction power. The percentage reduced was 4.41%.

With the addition of the camber controller, it was found that the vehicle is laterally offset during simulations. Therefore, indicating that the steering angle can be reduced, resulting in smaller road loads that the tyre must overcome. Resultantly, this could mean less power required to steer the vehicle. Therefore, the study found that potential for reducing power losses in electric vehicles with a camber controller exists.

Dedication

Dedicated to the memory of my beloved grandparents, who always believed in my ability to be successful in the academic arena. Without your support, this achievement would be impossible. Gone but not forgotten.

Disclaimer

During the process of completing this study, many unforeseen circumstances arose that led to the initial scope of this study having to change. This is due to the worldwide pandemic experienced during the time of completing this study. Due to the pandemic, South Africa have been in some level of lockdown since the 23rd of March 2020. Therefore, due to the severity of this pandemic and the negative effects it can have on our physical health, the access to the research facilities at the University of Pretoria was suspended for most of 2020. Due to this restriction of access, the scope of this study had to continuously change. The initial plan was to develop a means of experimentally validating the tyre model considered in this study, on a drum test rig. The tyre was validated for camber angles of up to 4 ° by **Wright (2017)**, but with the drum test rig, the tyre can be experimentally validated at higher camber angles. This testing phase had to be abandoned after all the simulated work was completed, due to the lack of campus access. This simulated work has been included in this study as there are valuable information concluded from the simulated work completed.

Acknowledgements

I would like to extend a special thanks to the following people that had a direct and indirect contribution to the completion of the thesis:

- Dr. H.A. Hamersma for the guidance throughout the project and all the great feedback throughout the year.
- Prof P.S. Els for his guidance and for allowing me to be a part of the VDG group.
- My parents, Juna and Derick Botha, who continuously supported me throughout the completion of the thesis during such a difficult time.
- My fiancé, Mine Bornman, for her continuous support through all the tough times and for standing by and believing in me.
- I would like to thank Andries Peenze for his support and willingness to assist with any problem.
- I would like to thank Lafras Fritz for the friendship and support at the VDG offices and for continuously motivating me throughout the entirety of the project.

Without the support of these individuals, this thesis would have been a more difficult task.

Contents

List of Figures

List of Tables

List of Symbols

List of Abbreviations	
4WD	Four Wheel Drive
ACS	Active Camber System
APS	Dynamic Tyre Pressure System
ARzS	Additional Normal Forces Generated by External Spring, Damping and Stabilizer Forces
AWD	All Wheel Drive
AWS	All Wheel Steering
BEB	Battery Electrical Buses
CG	Centre of Gravity
CR	Constant Radius
CSC	Camber-side slip controller
DLC	Double Lane Change
DOF	Degrees of Freedom
DYC	Direct Yaw Moment Control
EBM	Extended Brush Tyre Model
FAS	Front Axle Steering
FBS	Friction Brake System
i-AWD	Individually Controlled AWD
IEM	Traction/Brake Torques Generated by Electric Motors
IFS	Individual Front Wheel Steering
IRS	Individual Rear Wheel Steering
ISO	International Organization for Standardization
LFC	Lateral Force Coefficient
LLT	Lateral Load Transfer
RAS	Rear Axle Steering
RMSE	Root Mean Square Error
SMF	Simple Magic Formula
SUV	Sport Utility Vehicle
ULP	Universal Low Profile load cell
VDG	Vehicle Dynamics Group
WFT	Wheel Force Transducer

List of Lower Case Roman Symbols		
$\Delta\psi$	Yaw angle offset	[Dimensionless]
$\Delta y_{,off}$	Lateral Offset between baseline and controller	[m]

List of Lower Case Roman Symbols

Δy_1	Lateral offset between the vehicle and the road at current position	[m]
Δy_2	Lateral offset at preview distance l	[m]
h_{cm}	Height Centre of Gravity	[m]
a_x	Longitudinal Acceleration	$[m/s^2]$
a_y	Lateral Acceleration	$[m/s^2]$
g	Gravitational acceleration ($9.8m/s^2$)	$[m/s^2]$
h	Distance of roll centre to CG	[m]
h_0	Distance between roll centre and the ground	[m]
k_ψ	Yaw Angle offset Gain	[Dimensionless]
k_l	Lateral Offset at Preview Distance Gain	[Dimensionless]
k_y	Lateral Offset Gain	[Dimensionless]
l	Preview Distance	[m]
l_f	Distance between CG and front axle	[m]
l_r	Distance between CG and rear axle	[m]
m	Vehicle Mass	[kg]
r_e	Effective Rolling Radius	[m]
s	Moment arm	[m]
t	Pneumatic Trial	[m]
t_w	Wheel Track Width	[m]
v_{slide}	Sliding velocity of the tyre	$[m/s]$
y	Side/Lateral Force (Magic Formula Tyre model)	[N]

List of Upper Case Roman Symbols

$\dot{v_x}$	Longitudinal Acceleration	$[m/s^2]$
$\dot{v_y}$	Lateral Acceleration	$[m/s^2]$
C	Cornering Stiffness of front tyres	[N/°]
C	Cornering Stiffness of rear tyres	[N/°]
K_ϕ	Roll Stiffness Coefficient	[Dimensionless]
K_{camber}	Understeer Gradient due to Camber	[Dimensionless]
R_ϕ	Roll Coefficient	[Dimensionless]
A	Frontal area of Vehicle	$[m^2]$
B	Stiffness Factor	[Dimensionless]
$B_i, were\ i = x, y, t, r$	Componential Stiffness Factor	[Dimensionless]
C	Shape Factor	[Dimensionless]
C_{ar}	Coefficient of aerodynamic resistance	[Dimensionless]
C_c	Camber Stiffness coefficient	[Dimensionless]
C_f	Cornering Stiffness of front wheel	[N/°]
$C_i, were\ i = x, y, t$	Componential Shape Factor	[Dimensionless]
C_r	Cornering Stiffness of rear wheel	[N/°]
D	Peak Value	[Dimensionless]
$D_i, were\ i = x, y, t, r$	Componential Peak Value	[Dimensionless]
E	Curvature Factor	[Dimensionless]
ΔE_{Fric}	Change in Friction Energy	[Kwh]
$E_i, were\ i = x, y, t$	Componential Curvature Factor	[Dimensionless]

List of Upper Case Roman Symbols

F_{ar}	Aerodynamic Force	[N]
$F_{friction}$	Friction force between the tyre and the road	[N]
F_{z0}	Nominal Vertical Force	[N]
F_{zi}	Inner Vertical Force	[N]
F_{zo}	Outer Vertical Force	[N]
F_x	Longitudinal Force	[N]
F_y	Lateral Force	[N]
F_z	Vertical Force	[N]
G_γ	Weighting factor related to slip ratio and camber angle	[Dimensionless]
I_ω	Wheel rotational Inertia	$[kg.m^2]$
I_z	Moment of Inertia (z-axis)	$[kg.m^2]$
K	Understeer Gradient	[Dimensionless]
K_{12}	Camber and steering angle relationship	[Dimensionless]
K_{34}	Camber and steering angle relationship	[Dimensionless]
K_D	Derivative Gain	[Dimensionless]
K_I	Integral Gain	[Dimensionless]
K_P	Proportional Gain	[Dimensionless]
L	Wheelbase ($L = l_f + l_r$)	[m]
M_x	Overturning Moment	[N.m]
M_y	Rolling Resistance Moment	[N.m]
M_z	Self-Aligning Moment	[N.m]
M_zr	Residual Self aligning moment	[N.m]
P	Power	[Kw]
P_{arl}	Aerodynamic Power Loss	[Kw]
P_{camber}	Power required to control camber angle	[Kw]
P_{cRes}	Cornering Resistance Power Loss	[Kw]
P_{Fric}	Friction Power Loss	[Kw]
$P_{Fric,all}$	Total Friction Power on all 4 Wheels	[Kw]
P_{latacc}	Lateral Acceleration Power Loss	[Kw]
$P_{latslip}$	Lateral Slip Power Loss	[Kw]
$P_{longacc}$	Longitudinal Acceleration Power Loss	[Kw]
$P_{longslip}$	Longitudinal Slip Power Loss	[Kw]
P_{rrl}	Rolling Resistance Power Loss	[Kw]
P_{Scrub}	Tyre Scrub power Loss	[Kw]
P_{wal}	Wheel Angular Acceleration Power Loss	[Kw]
P_{yal}	Yaw Acceleration Power Loss	[Kw]
P_a	Additional Power Loss	[Kw]
P_w	Power for Propelling the Wheels	[Kw]
q_{cz1}	Magic Formula tyre Coefficient	[Dimensionless]
R	Radius of curvature	[m]
R_0	Effective Radius of the tyre	[m]
$S_{sz1}, S_{sz2}, S_{sz3}, S_{sz4}$	Magic Formula tyre Coefficient	[Dimensionless]
S_h	Horizontal Shift	[°]
$S_h, wherei = x, y, t$	Componential Horizontal Shift	[°]
S_v	Vertical Shift	[N or N.m]
$S_v, wherei = x, y, t$	Componential Vertical Shift	[N or N.m]

List of Upper Case Roman Symbols

T	Torque/driving moment	[N.m]
$Total, E_{Fric}$	Change in Total Friction Energy	[Kwh]
V	Vehicle Speed	$[m/s]$
v_x	Longitudinal Velocity	$[m/s]$
v_y	Lateral Velocity	$[m/s]$
W	Work	$[J]$
W_f	Load on Front Wheels	[N]
W_r	Load on Rear Wheels	[N]
$(U_{PID})_C$	Camber Control System Output Voltage	[V]
$(U_{PID})_T$	Toe Control System Output Voltage	[V]

List of Greek Symbols

α_f	Front Slip Angle	$[rad]$
α_r	Rear Slip Angle	$[rad]$
$\ddot{\psi}$	Yaw Acceleration	$[rad/s^2]$
$\dot{\beta}$	Side-slip rate	$[rad/s]$
η	Percentage Power Saved	[%]

List of Greek Symbols

$\dot{\gamma}$	Rate of change of camber angle	$[rad/s]$
$\dot{\omega}$	Wheel Angular Acceleration	$[rad/s^2]$
$\dot{\psi}$	Yaw Rate	$[rad/s]$
ϕ	Roll Angle	$[rad]$
θ	Angular Distance	$[rad]$
θ_{Creq}	Desired Camber Angle	$[rad]$
$\theta_{Cactual}$	Actual Camber Angle	$[rad]$
θ_{Treq}	Desired Toe Angle	$[rad]$
$\theta_{Tactual}$	Actual Toe Angle	$[rad]$
α	Slip Angle	$[rad]$
δ_f	Front Steering Angle	[rad]
ε_{LuGre}	Percentage Error Dynamic Tyre Friction Model	[%]
ε_{MFtire}	Percentage Error Magic Formula Tyre Model	[%]
ε_{TMeasy}	Percentage Error TMeasy Tyre Model	[%]
$\varepsilon_{TreadSim}$	Percentage Error Tread Sim Tyre Model	[%]
γ	Camber Angle	[rad]
κ	Longitudinal Slip Ratio	[Dimensionless]
ω	Wheel Angular Velocity	$[rad/s]$
	Yaw Angle	$[rad]$
ψ_{ref}	Reference Yaw Rate	$[rad/s]$
ρ	Density of Air	$[kg/m^3]$
C_γ	Camber Stiffness	[N/°]

Chapter 1

Introduction

1.1 Background

In recent years, a noticeable increase in popularity for Sport Utility Vehicles (SUVs) has resulted in an increase in the number of fatal crashes due to rollovers. High bodied SUV type vehicles are often designed for off-road use. Thus, a compromise for on-road performance is made for better off-road performance. They are designed with soft suspension systems for ride comfort and large wheel travel to increase the mobility on rough terrain. The long-travel soft suspension also helps SUVs to traverse uneven terrain. These types of vehicles have a high rollover propensity due to their high centre of gravity.

Due to the increasing popularity of SUVs, it is expected that the fatality rate of SUVs will show a similar trend. Considering occupant death by vehicle type from 1975 to 2018, reveals exactly what was expected. The fatality of SUVs has increased as the popularity of this vehicle type has been increasing over recent years. The vehicle occupant deaths by vehicle type are illustrated in Figure 1.1. From 1975 to 2018, the number of fatal passenger vehicle crashes have decreased by almost 25% from 29,844 to 22,894 **(Insurance Institute for Highway Safety (IIHS), 2018)**.

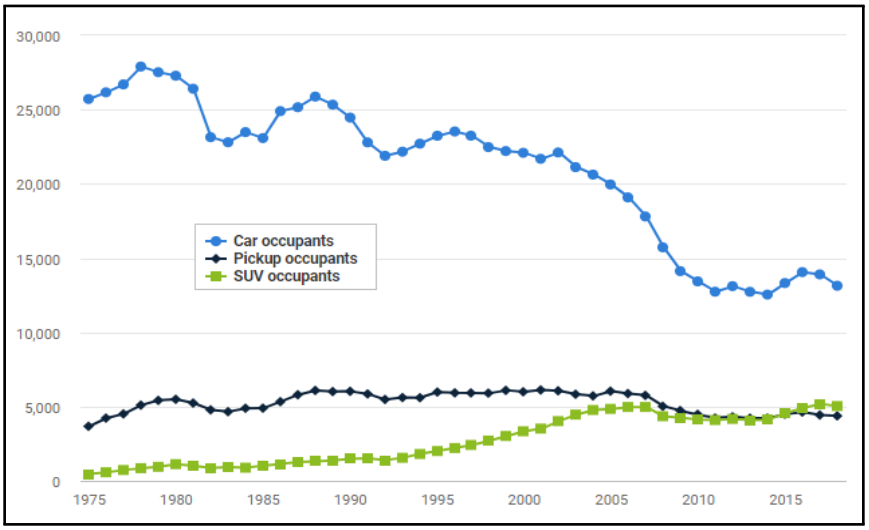

Figure 1.1: Passenger vehicle occupants deaths by vehicle type, 1975-2018 **(Insurance Institute for Highway Safety (IIHS), 2018)**

Due to an recent increase in the popularity of electrically propelled vehicles, there is an ever-growing requirement for electric vehicles to become more energy efficient. As a result of the expensive battery packs and limited driving range of electric vehicles, a new trend of energy efficient control methods has been surfacing.

Methods which include the use of direct yaw moment control (DYC) **(Sun et al., 2020)** and camber control to reduce the energy losses during cornering **(Sun et al., 2018)**. The study of actively controlling the camber angle has recently gained interest due to the possibility of reducing energy losses. This recent interest means that there is truly little information published to date. As a result of increasing popularity of the electrification of a vehicle's driveline, the investigation of actively controlling the camber angle could prove valuable in reducing the energy losses in cornering situations. Studies that utilizes DYC to improve the energy losses during cornering, have been conducted by **Sun et al. (2020)**. **Sun et al. (2020)** have found that the energy efficiency during cornering can be improved by as much as 10 %, by utilising a DYC method. The DYC method is used to minimize the tyre's slip loss and resultantly reduces the total energy consumption of the steering system to overcome the road loads in the tyres, during cornering.

Studies that investigated the camber control's contribution to the power loss during cornering have found that for higher lateral acceleration and more severe cornering manoeuvres, that a maximum power saving of 22.1 % is observed **(Sun et al., 2018)**. At lower lateral acceleration and larger constant radius corners, the power saving reduces. However, **Sun et al. (2018)** found that with the implementation of camber control, a reduction in the power losses is observed. Figure 1.2 illustrates the total power saving for the camber controller for different lateral acceleration and constant radius turns. The power consumption of the steering system of a vehicle could potentially be reduced by minimizing the power losses in the vehicle road contact area (tyres). Therefore, the investigation into power efficient cornering with camber control should be conducted in greater detail to fully explore the advantages and disadvantages of camber control.

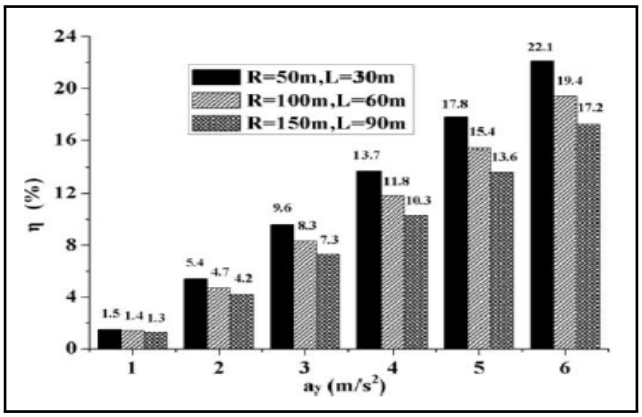

Figure 1.2: Energy Saving with Camber Control **(Sun et al., 2018)**

Thus, any power saving tactics that could potentially increase the efficiency and resultantly the electrical range, will be beneficial to investigate. This includes the method of active wheel control to improve energy efficiency during cornering, without compromising on vehicle dynamic behaviour.

During dynamic cornering manoeuvres, the vehicle and the steering system of the vehicle requires power to overcome the tyre-road forces and moments. Two proposed concepts are investigated. **Park and Sohn (2012)** investigated a method for actively changing

the camber angle on the front and rear wheels of a vehicle by using linear actuators. They proposed that by actively changing the camber angle of a vehicle will result in an improved vehicle dynamic response during cornering manoeuvres. The second proposed concept is presented by **Sun et al. (2018)** wherein active camber control is used to reduce the amount of energy losses of the vehicle during dynamic cornering manoeuvres.

1.2 Research Question

This thesis investigates energy savings through camber control by utilizing an experimentally validated non-linear FTire tyre model **(Gipser and Hoffmann, 2016)**. The investigation was conducted with an experimentally validated nonlinear ADAMS/View **(MSC Software, 2013)** multibody dynamics full-vehicle model with nonlinearities in the suspension and bushings being considered.

The question therefore is: **Can efficient cornering of an SUV be achieved using camber control?**

The novelty of this approach is the use of an experimentally validated, nonlinear vehicle model with nonlinear tyre models. The results will be compared to the results found by **Sun et al. (2018)**.

Chapter 2

Literature Study

The literature study sets out to gather information on the basics of the problem statement, and to determine the current, state-of-the-art solutions to address the problem. The literature survey starts with researching the different types of tyre models and their strengths and weaknesses. The results of which should generate an informed decision as to what tyre model would be the best to use. The effect of camber on the tyre models will also be included in the study, to fully understand the behaviour of various tyre models with regards to the problem at hand.

The effects of camber angle on the vehicle dynamic behaviour are also investigated in the literature review. A brief introduction to basic vehicle dynamic concepts is included. Finally, the literature review concludes with a case study which investigates the effects of camber angle control of the front and rear suspension, on the vehicle dynamic behaviour. By understanding the contribution of camber on a vehicles' suspension system, meaningful conclusions can be drawn on whether camber control could improve vehicle dynamic behaviour. Once the effects of camber control on the vehicle dynamics have been investigated, the literature review sets out to determine the possibility of reducing the power consumed by a vehicle with camber control implemented.

From the literature review, the basic knowledge will have been gained to guide the study of determining the power implications of active camber control on the power consumption of a vehicle during dynamic cornering manoeuvres.

2.1 Axis System

The vehicle axis system is used when referring to the dynamics of the vehicle around its axis as outlined in Figure 2.1a. From Figure 2.1a the forward direction of travel of the vehicle is along the longitudinal or x-axis. A vehicle rolls along its longitudinal axis. The direction to the side of the vehicle, perpendicular to the longitudinal axis, is referred to as the lateral axis. A vehicle experiences a pitching moment about its lateral axis. The vertical axis is defined as the axis that is vertically upwards or downwards perpendicular to the longitudinal axis. A vehicle experiences a yaw moment about its vertical axis **(Gillespie, 1992)**.

The axis system outlined in Figure 2.1b, is based on the same directions as the axis system of the vehicle, but with some slight differences. The moment experienced by a tyre about

its longitudinal axis is referred to as the overturning moment. The moment experienced about its lateral axis is referred to as the rolling resistance moment of the tyre. The moment experienced about the vertical axis is referred to as the aligning torque of the tyre. Subsequently, the positive slip angle and the positive inclination angles are also represented on the diagram for future reference **(Gillespie, 1992)**.

This axis system is used as the industry standard orientation of the axis of a vehicle. This axis system will be adhered to throughout the entirety of the paper and all its discussions **(Gillespie, 1992)**.

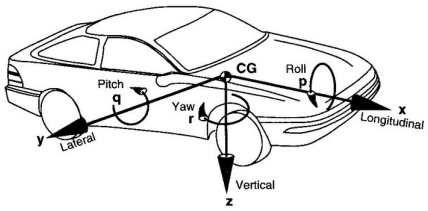

(a) Vehicle Axis System (SAE)

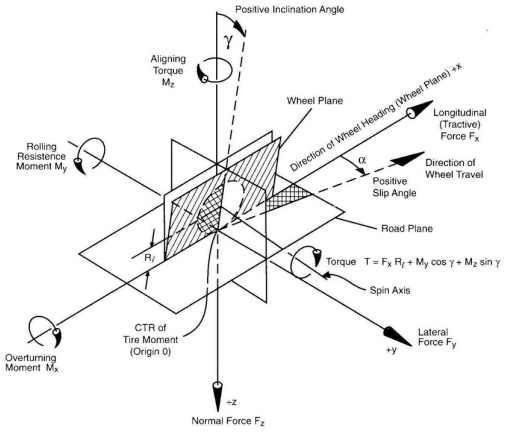

(b) Tyre Axis System (SAE)

Figure 2.1: SAE Axis System's **(Gillespie, 1992)**

2.2 Tyre Slip Angle

The tyre slip angle is defined as the angle between the heading of the tyre and the direction of travel when a rolling pneumatic tyre is subjected to cornering forces (lateral forces). This phenomenon is depicted in Figure 2.1b and Figure 2.2. **Gillespie (1992)** describes the development of the slip angle depicted in Figure 2.2. If the vehicle is travelling straight forward, then there is no development of any lateral forces on the tyre and accordingly no slip angle. Once the vehicle starts cornering, the development of lateral forces is observed. The tread elements (contact patch) of the tyre remain in the direction of its original travel (direction of travel) and are deflected sideways as observed in Figure 2.2. Thus, the lateral force builds as the lateral force starts moving towards the rear of the contact patch until the point where the lateral force acting on the tyre overcomes the frictional level available, at which point tyre slip occurs. The slip angle build up is not instantaneous but lags slightly due to the necessity of deflecting the sidewall of the tyre in the lateral direction. The lag of the side slip propagation is due to the rolling of the tyre. It typically takes a half to a full rotation of the wheel for the lateral force to reach steady state **(Gillespie, 1992)**.

2.3 Camber Angle

The camber angle is defined as the angle of inclination of a wheel inward or outwards from the body of the vehicle. Positive and negative camber angles are depicted in Figure 2.3

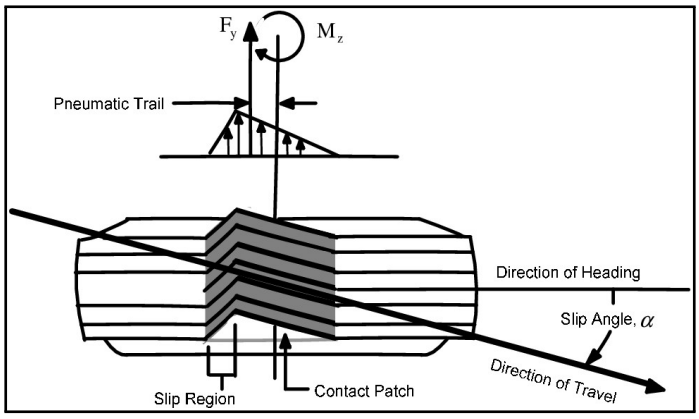

Figure 2.2: Slip Angle due to rolling tyre deformation under lateral force **(Gillespie, 1992)**

on the left and the right respectively. The camber angle on a wheel will produce a lateral force on the wheel. The lateral force is known as camber thrust. The amount of lateral force produced by the camber angle is less compared to the lateral force produced by the slip angle. **Gillespie (1992)** reports that about 4° to 6° of camber angle are required to produce the same lateral force that 1 degree of slip angle produces (this might be tyre specific). The radial tyre requires between 10° to 15° of camber angle due to the lower camber stiffness of the radial tyres. Camber angles are small on solid axis vehicles and can only contribute to about 10% to the lateral forces generated by the tyre.

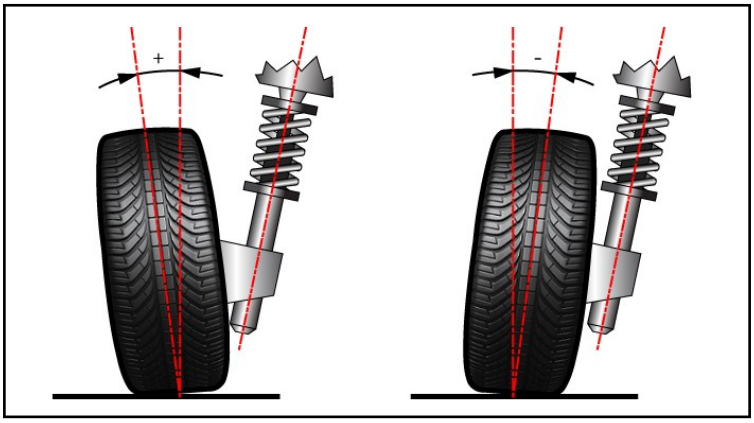

Figure 2.3: Positive and Negative Camber Angle **(González, 2019)**

Radial ply tyres are the most common types of tyres on passenger cars. The ply of the tyres can play a role in the camber stiffness coefficient C_c. The typical camber stiffness coefficients for bias-ply and radial-ply tyres are 0.018/° and 0.008/° respectively **(Smith, 2004)**. The camber stiffness coefficient can be related to the lateral force with equation 2.1.

$$F_y = C_\gamma \gamma = C_c F_z \gamma \tag{2.1}$$

The lateral forces generated by the camber angle, defined in equation 2.1 is used to compute the camber thrust. This is the contribution of the camber angle to the lateral forces on the tyre.

2.4 Tyre Models

Mathematical tyre models are extremely important methods used to capture the behaviour of a vehicle's tyre under various conditions. Mathematical tyre models are used during the development of new vehicles and are only a useful tool if the tyre model can accurately represent the actual dynamic behaviour of the tyre. **Stallmann (2014)** has described the modelling of the interaction between the tyre and the road as the single most important component of creating a simulation model. He stated that all other components of the simulation model are influenced by the forces and the moments that are generated between the tyre and the road. Therefore, to create an accurate vehicle simulation model, an accurate representation of the tyre to road contact is of the upmost importance. Over the years, a great amount of work has gone into the development of tyre models which can accurately represent the behaviour of a tyre.

Stallmann (2014) stated that there are various requirements for a tyre model for different applications. Some simulations require great accuracy and therefore a perfectly accurate tyre model. Other simulations require a fast-solving time and therefore does not require great accuracy. Figure 2.4 represents the tyre selection chart for the different tyre models in Adams **(MSC Software, 2013)**.

MD Adams	Event / Maneuver	ADAMS/ Handling Tire							Specific Models	
		PAC2002[1]	PAC-TIME[1]	PAC89[1]	PAC94[1]	FIALA[1]	5.2.1.[1]	UA Tire[1]	PAC-MC[1]	FTire
Handling	Stand still and start	+	o/+	o/+	o/+	o/+	o/+	o/+	o/+	+
	Parking (standing steering effort)	+	-	-	-	-	-	-	-	+
	Standing on tilt table	+	+	+	+	+	+	+	+	+
	Steady state cornering	+	+	o/+	+	0	0	o/+	+	o/+
	Lane change	+	+	o/+	+	0	0	o/+	+	o/+
	ABS braking distance	+	o/+	o/+	o/+	0	0	o/+	o/+	+
	Braking/power-off in a turn	+	+	0	0	0	0	0	+	o/+
	Vehicle Roll-over	+	0	0	0	0	0	0	0	+
	On-line scaling tire properties	+	-	-	-	-	-	-	-	0
Ride	Cornering over uneven roads *	o/+	0	0	0	0	0	0	0	o/+
	Braking on uneven road *	o/+	0	0	0	0	0	0	0	+
	Crossing cleats / obstacles	-	-	-	-	-	-	-	-	+
	Driving over uneven road	-	-	-	-	-	-	-	-	+
	4 post rig (A/Ride)	+	o/+	o/+	o/+	o/+	o/+	o/+	o/+	o/+
Chassis Control	ABS braking control	o/+	0	0	0	0	0	0	0	+
	Shimmy[2]	o/+	0	0	0	0	0	0	0	+
	Steering system vibrations	o/+	0	0	0	0	0	0	0	+
	Real-time	+	-	-	-	-	-	-	-	-
	Chassis control systems > 8 Hz	o/+	-	-	-	-	-	-	-	+
	Chassis control with ride	-	-	-	-	-	-	-	-	+
Dura-bility	Driving over curb	-	-	-	-	-	0	0	-	o/+
	Driving over curb with rim impact	0	-	-	-	-	0	0	-	o/+
	Passing pothole	-	-	-	-	-	0	0	-	o/+
	Load cases	-	-	-	-	-	0	0	-	o/+

-	Not possible/Not realistic
0	Possible
o/+	Better
+	Best to use

* wavelength road obstacles > tire diameter
[1] use_mode on transient and combined slip
[2] wheel yawing vibration due to supension flexibility and tire dynamic response

Figure 2.4: Selection chart for ADAMS Tyre models **(MSC Software, 2013)**

The rating scheme is used to inform the user on the performance of the tyre models in different manoeuvres. However, this rating scheme fails to inform the user about the accuracy of the tyre models. From the selection chart in Figure 2.4, it is clear that the

FTire model is able to represent all the manoeuvres in the chart. However, some better than others.

An investigation conducted by **Uil (2008)** into four different types of tyre models. The four types of tyre models investigated are the Magic Formula tyre model, TMeasy tyre model, TreadSim tyre model and the Dynamic tyre friction tyre model. The tyre models are compared based on the fit results and the extrapolation qualities of the tyre models. The longitudinal velocity and the friction levels are adjusted to analyse the extrapolation qualities of the tyre models. Two cases were investigated with all four tyre models. The cases where the camber contribution is neglected and included. The results from the test conducted by **Uil (2008)** are represented in Table 2.1 and Table 2.2.

Table 2.1: Errors of optimization results for tyre models without Camber. **Uil (2008)**

No Camber	$\varepsilon_{MFTire}[\%]$	$\varepsilon_{TMeasy}[\%]$	$\varepsilon_{TreadSim}[\%]$	$\varepsilon_{LuGre}[\%]$
Pure F_x	1.18	1.35	4.46	2.85
Pure F_y	1.33	2.12	4.50	4.85
Pure M_z	7.02	17.20	25.29	24.28
Combined Slip Characteristics (F_x)	2.56	7.12	6.33	3.84
Combined Slip Characteristics (F_y)	3.84	20.71	12.12	8.58
Number of Parameters	63	26	14	26

Table 2.2: Errors of optimization results for tyre models with Camber. **(Uil, 2008)**

Camber	$\varepsilon_{MFTire}[\%]$	$\varepsilon_{TMeasy}[\%]$	$\varepsilon_{TreadSim}[\%]$	$\varepsilon_{LuGre}[\%]$
Pure F_x	1.74	2.03	5.26	-
Pure F_y	1.48	2.79	5.38	-
Pure M_z	10.03	20.18	26.23	-
Combined F_x	2.63	7.36	5.99	-
Combined F_x	4.46	20.94	16.02	-
Number of Parameters	91	26	14	-

Uil (2008) concludes that the Magic Formula tyre model yields the best approximation for the steady-state tyre characteristics. The main advantage of the Magic Formula is its accuracy and the low computational effort required **(Uil, 2008)**. **(Uil, 2008)** makes no mention of what specific version of the magic formula tyre model was used.

2.4.1 Magic Tyre Formula

The Magic Formula is used to calculate the steady-state tyre forces and moment characteristics that are used in vehicle dynamics studies **(Uil, 2008)**. The tyre model sets out to define a set of coefficients that can accurately describe the behaviour of the tyre. The coefficients are used in equation 2.2 which can describe all the characteristics of the side force, brake force and self-aligning torque of a vehicle's tyres. The Pacejka tyre model takes the non-isotropic characteristics of a tyre into account when defining a vehicle's tyre model. Some other characteristics that were considered during the setup of the Pacejka tyre model are ply steer, conicity, rolling resistance and camber. Equation 2.2 sets out to define the Pacejka tyre model **(Pacejka et al., 1989)**.

$$y(x) = D.\sin C.\arctan\left(Bx - E[Bx - \arctan\left(Bx\right)]\right) \tag{2.2}$$

In equation 2.2, $y(x)$ is representative of the side force, braking force, or self-aligning torque. By denoting X as the slip angle (α) or longitudinal slip (κ). Thus, equation 2.2 can be written in the form of equations 2.3 and 2.4.

$$Y(X) = y(x) + S_\nu \tag{2.3}$$

$$x = X + S_h \tag{2.4}$$

Where,

- $B \rightarrow$ Stiffness Factor
- $C \rightarrow$ Shape Factor
- $D \rightarrow$ Peak Value
- $E \rightarrow$ Curvature Factor
- $S_h \rightarrow$ Horizontal Shift
- $S_\nu \rightarrow$ Vertical Shift

Coefficients B, C, D and E are graphically represented in Figure 2.5, on a graph of the lateral force (F_y) versus the slip angle (α). With equation 2.2, the behaviour of a tyre in a tyre model is described by the coefficients a_0 to a_{13} or b_0 to b_{15}. The camber angle on the wheels may result in a considerable shift of the F_y v.s. α curves, represented by the magic formula tyre model. These coefficients differ for each of the three load cases. By fully defining the properties of a tyre, one can accurately predict the behaviour of other mechanisms of a vehicle's handling and stability.

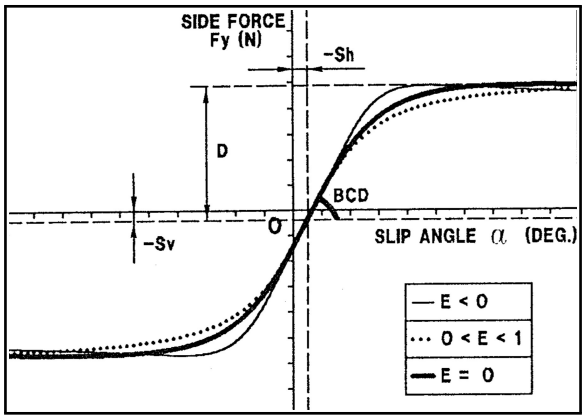

Figure 2.5: Graphical representation of coefficients in equation 2.2 **(Pacejka et al., 1989)**

The Magic Formula tyre model typically yields a graph that passes through the origin ($x = y = 0$), reaches a maximum value and then reaching a horizontal asymptote. For the case of combined slip, the Magic Formula tyre model changes slightly and includes a weighting component. The weighting factor is more related to the longitudinal slip and less related to the camber angle of the tyre.

2.4.2 FTire Model

The next tyre model to be considered is the FTire (Flexible Structure Tyre Model) tyre model. FTire is an in-and out-of-plane tyre model. FTire is also a full three-dimensional

and highly nonlinear physics-based tyre model **(Gipser and Hoffmann, 2016)**. FTire is designed to be used in multi-body dynamics simulations wherein the ride comfort or handling of a vehicle is simulated. An FTire model is constructed with three main components.

The first component is a flexible ring structure model. This structural model is used to define the damping, structural stiffness, and the inertial properties of the tyre. The belt segments and the belt element stiffnesses are illustrated in Figure 2.6. These belt segments are made of a set of flexible rings. Each flexible ring is made of a finite number of elements that are interconnected to each other with springs. Thus, allowing the in-and out-of-plane motion that FTire is known for.

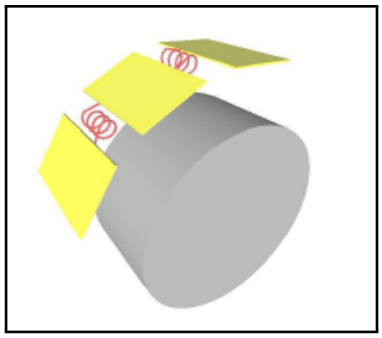

(a) In-Plane Bending Stiffness

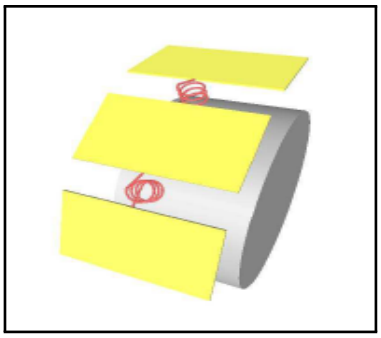

(b) Out-of-Plane Bending Stiffness

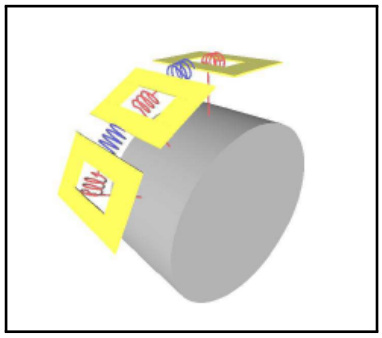

(c) Belt Circumferential Torsion and Twist Stiffness

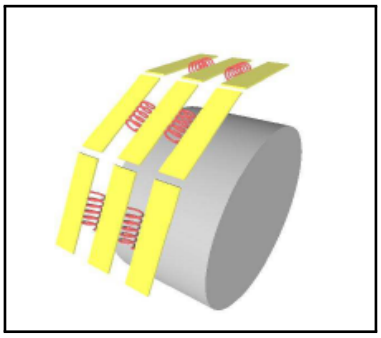

(d) Belt Lateral Bending Stiffness

Figure 2.6: FTire belt element stiffnesses **(Gipser and Hoffmann, 2016)**

The belt elements and their respective degrees of freedom is illustrated by Figure 2.7. Between 100 and 200 belt elements are used to define the tyre. Every single belt element is further associated with between 10 and 100 mass less "tread blocks". Each of these "tread block" elements and their associate degrees of freedom is described in table 2.3.

The second component is the tread model of the tyre. The tread model is the estimation of the following components of the tyre, due to its contact with the ground **(Bosch, 2016)**:

- Height of the tyre contact patch
- Friction coefficient between the tyre and the road surface
- The compliance in the tyre contact patch
- Calculation of the ground pressure in the tyre contact patch

Table 2.3: Belt elements degrees of freedom **(Bosch, 2016)**

Type of DOF	Degrees of Freedom
(a) Translational	Longitudinal displacement Lateral displacement Vertical displacement
(b) Torsional	Rotation of the circumferential axis
(c) Bending	Bending in lateral direction

- Calculation of the shear stresses in the tyre contact patch

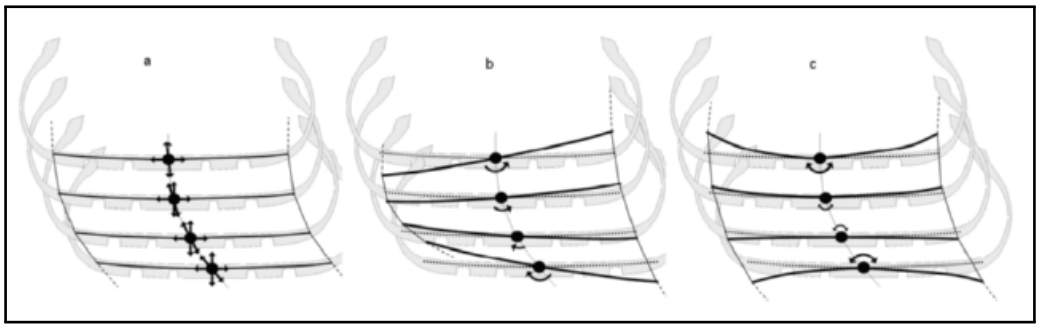

Figure 2.7: FTire belt elements degrees of freedom **(Bosch, 2016)**

The third component of the FTire model is the thermal model. The thermal model is an optional output from the FTire model. The thermal model consists of three main sections. The first is a thermodynamic calculation of the inflation pressure. The second is a heat transfer and heat generation model, with variables representing the temperature of the tyres structure and each individual contact element. Finally, the third is "rubber temperature" of the tread friction characteristics, in addition to the ground pressure and sliding velocity of the tyre **(Gipser and Hoffmann, 2016)**.

For simplicity, the FTire tyre is assumed to be separated into three distinct regions, with different thermal properties. The thermal tyre model and its three regions is illustrated in Figure 2.8. The three regions are:

- Tyre structure (sidewall, belt and air volume)
- Tread without contact patch
- Contact patch

The tyre chosen for the investigation in this study is a Pirelli Scorpion SUV tyre. Full parameterisation and validation of the Pirelli tyre model, was conducted by **Wright (2017)**. Details of the tyre will be discussed at a later stage.

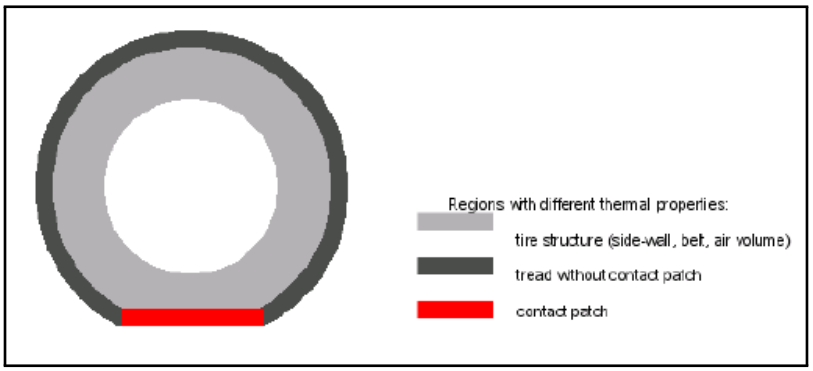

Figure 2.8: FTire thermal model **(Gipser and Hoffmann, 2016)**

2.4.3 Parameterisation of Pirelli FTire model

During the process of parameterizing the tyre, **Wright (2017)** set out to compare the results from the experimental testing with the results from the FTire tyre model. The experimental tests of the Pirelli tyre were conducted on the tyre test trailer. The test trailer is towed behind a vehicle and the slip angle and brake pressure of the trailer is controlled. For the longitudinal tyre forces, the brake pressure is gradually ramped up until the tyre is completely locked up. For the lateral tyre forces, the slip angle is changed with two electric actuators applying a positive toe angle ranging from 1 ° to 16 ° and swept back to 1 °. Thus, allowing **Wright (2017)** to gather all the necessary data to validate the FTire tyre model. The vertical, longitudinal and lateral stiffness results from the validation tests are displayed in Figure 2.9a, Figure 2.9b and Figure 2.9c respectively.

Wright (2017) validated the tyre model at $\gamma = -4°$ camber as well as $\gamma = 0°$. The correlation between the test data and the simulated data was observed to be more than sufficient for $\gamma = -4°$, **Wright (2017)** concluded. A comparison of the longitudinal and lateral test data with the simulated data is illustrated in Figure 2.10a and Figure 2.10b respectively.

2.4.4 Tyre Model Discussion

From the results presented by **Uil (2008)**, it was concluded that the Magic Formula tyre model performed the best by representing the actual behaviour of the steady-state tyre characteristics, with the smallest errors reported, although **Uil (2008)** never makes mention of what version of the Magic Formula tyre model was used. There are two main mechanisms of force generation in the tyre of a vehicle. These mechanisms are the friction and hysteresis in the tyre road contact. The bond between the tyre contact patch and the road surface results in a friction force mechanism being generated. The energy losses in the rubber of the tyre when it deforms, is known as the hysteresis in the tyre. The Magic Formula tyre model cannot represent or predict the hysteresis in the tyre **(Hamersma, 2014)**.

From the table shown in Figure 2.5, it is shown that for MSC ADAMS simulations, the FTire tyre model is best overall representative of most of the manoeuvres represented in the table. The FTire tyre model is made up of three distinct models one of which is the thermal model. The thermal model can model the thermal behaviour of the tyre, which includes the hysteresis in the contact patch. The hysteresis in the contact patch is the

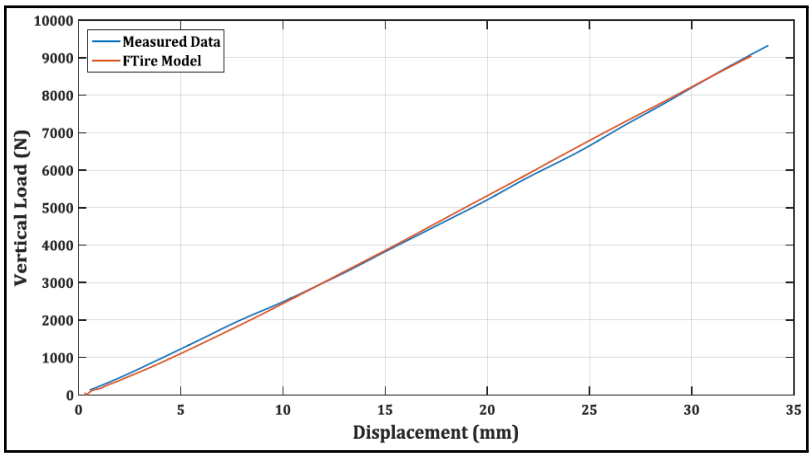

(a) Vertical Stiffness

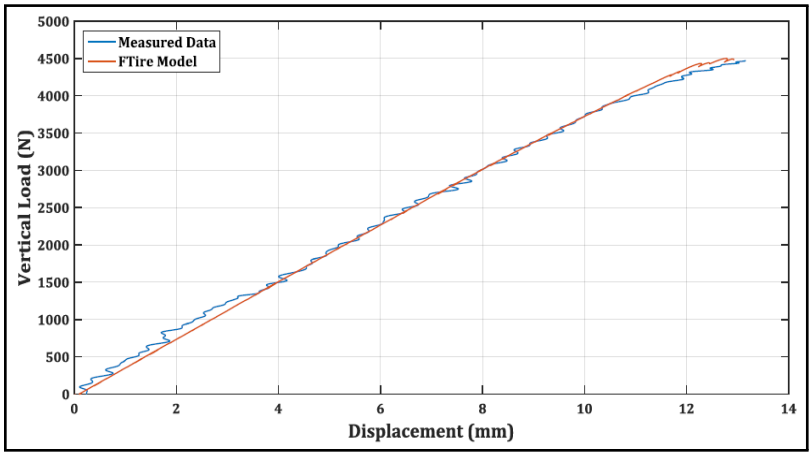

(b) Longitudinal Stiffness

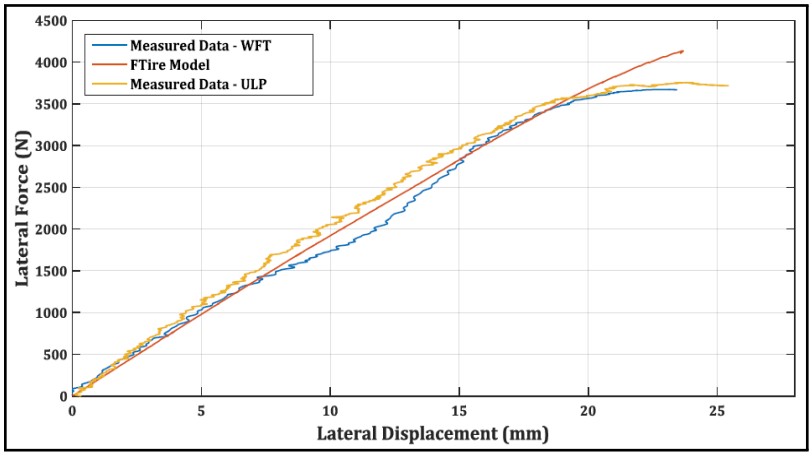

(c) Lateral Stiffness

Figure 2.9: Tyre Stiffness Validation **(Wright, 2017)**

energy losses in the rubber when it deforms during any dynamic manoeuvre. This will be extremely beneficial when modelling the power losses due to camber control.

With the availability of a fully validated FTire tyre model, which was done by **Wright (2017)**, the decision was made to make use of FTire to model the behaviour of the tyre during this study. Wright has shown that the FTire tyre model can accurately model the tyre road loads and accurately represent the behaviour of the tyre, invoking confidence in

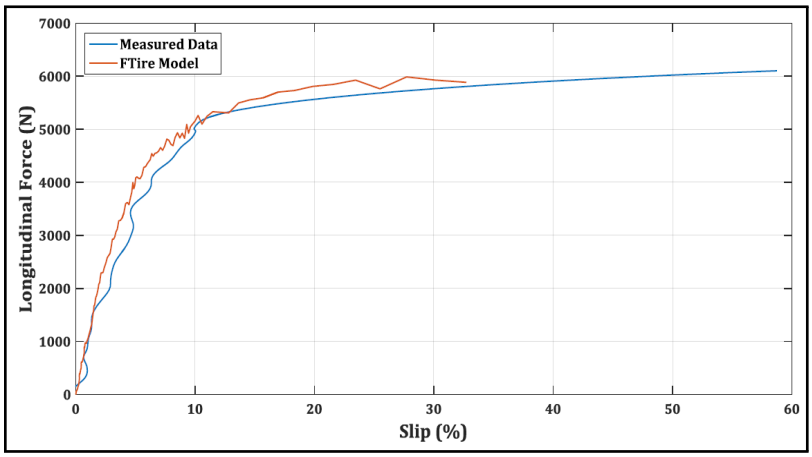

(a) Longitudinal Force versus Longitudinal Slip

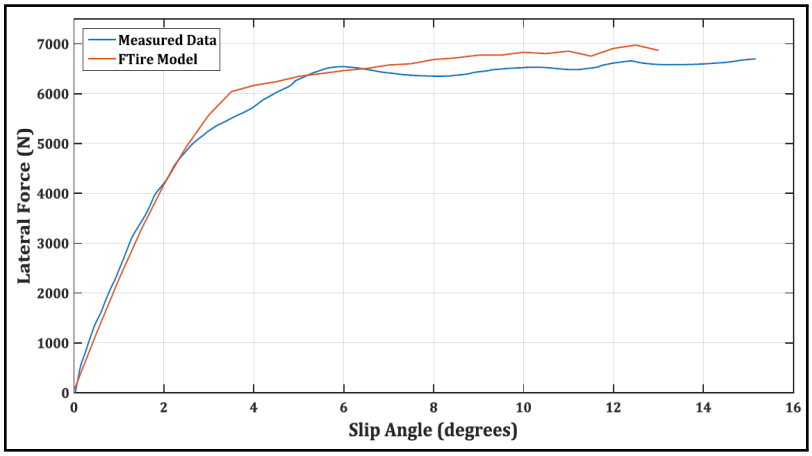

(b) Lateral Force versus Slip Angle

Figure 2.10: Tyre Longitudinal and Lateral force Validation **(Wright, 2017)**

the results that FTire will deliver.

2.5 Defining Power Losses in Tyres

The tyre models have been discussed in detail in the previous sections. The mechanisms used to calculate the power losses in the tyres with the FTire model is described in this section. These calculations form part of the built-in functionality of the FTire software and is defined by FTire as discussed below **(Gipser and Hoffmann, 2016)**.

The power loss mechanism that will be investigated in this section is the power loss due to friction between the tyre and the road interaction. The friction power loss computed by the FTire software is defined in equation 2.5. Equation 2.5 gives a bulk formulation of how the friction power loss is computed with FTire. The bulk formulation is representative of the friction power over all the nodes in the tyre tread elements.

$$P_{frict} = |v_{slide}|.|F_{friction}| \tag{2.5}$$

Where v_{slide} is sliding velocity of the tyre and $F_{friction}$ is the friction force between the

tyre and the road. A certain fraction of the power lost in the tyre tread element is to dry friction, with the remainder of the power loss heating the tyre.

2.6 Case Study: Effects of camber angle control of front suspension on vehicle dynamic behaviour

The investigation into the effects of changing the camber angle of the front suspension has been conducted by **Park and Sohn (2012)**. The paper focusses on the design and implementation of a new electronic camber adjustable suspension mechanism. The mechanism allows the operator to adjust and control the geometry of the steering system. The system controls the camber angle of the front wheels rather than the brake and driving torques to improve the cornering performance of the vehicle. The mechanism is incorporated on a double-wishbone suspension system. **Park and Sohn (2012)** developed and used a bicycle model to design the controls of the mechanism. The mechanism is designed and simulated in ADAMS/Car and MATLAB/Simulink co-simulation. The model of the mechanism was simulated with a fishhook manoeuvre and a single lane-change manoeuvre.

The concept of the mechanism is based on changing the geometry of the upper control arm of the double-wishbone suspension with a rack and pinion gear system. A rotary motor that uses the rack and pinion mechanism is used at each of the two points where the upper control arm is connected to the vehicle's chassis. The concept of the mechanism is graphically depicted in Figure 2.11. The idea is that the two arms of the upper control arm are moved outwards, resulting in an inwards movement of the top of the vehicle tyre.

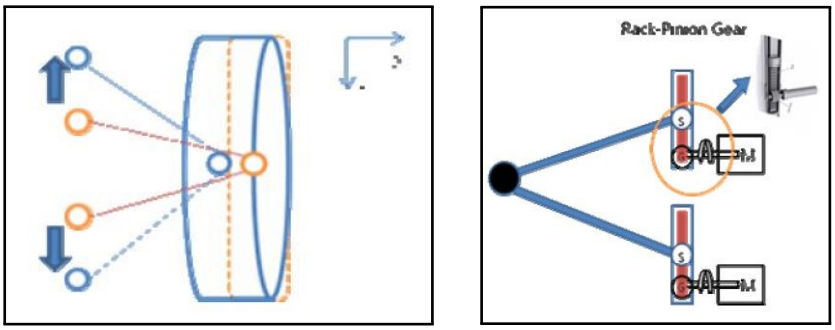

(a) Active Camber Mechanism working illustration

(b) Rack and Pinion actuator Placement

Figure 2.11: Case Study: Camber angle Adjustment Mechanism **(Park and Sohn, 2012)**

The image in Figure 2.11a illustrates the working if the mechanism. The points where the upper control arm is connected to the vehicle's frame is moved outwards, bringing the top of the upright inwards towards the chassis of the vehicle. Thus, resulting in a more negative camber angle as the top of the tyre is moved inwards towards the chassis of the vehicle. Figure 2.11b demonstrates the rack and pinion rotary motors position in the active camber mechanism.

The mechanism operates based on two inputs. The mechanism requires the steering angle and the vehicle longitudinal velocity as input to the ECU which calculates the required camber angle. Accordingly, the actuator is operated to make the required camber angle adjustments. The control system is based on the camber control strategy in Figure 2.12.

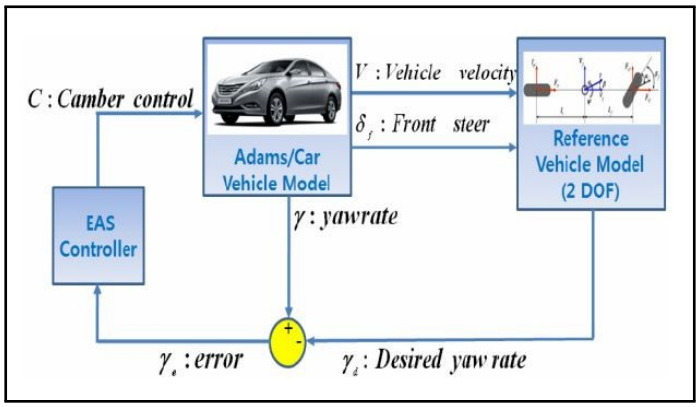

Figure 2.12: Case Study: Camber Control Strategy **(Park and Sohn, 2012)**

During steady-state cornering, the reference yaw rate is calculated with equation 2.6 by assuming steady-state conditions.

$$\dot{\psi}_{ref} = \frac{1}{\left(1 - \frac{m}{2L^2}\frac{l_f.C_f - l_r.C_r}{C_f.C_r}{V_x}^2\right)}\frac{V_x}{L}\delta_f \tag{2.6}$$

The current velocity and steering angle are used to calculate the reference yaw rate. The reference yaw rate is compared to the vehicle yaw rate and the error is minimized with a controller and used as input to the active camber mechanism. The controller is used purely for controlling the camber angle. The steering angle is given as an input to the simulation, therefore no steering controller was used. Therefore, adjusting the camber angle based on the yaw rate calculations. The control strategy is outlined in Figure 2.12.

Park and Sohn (2012) conducted a fishhook and single lane change simulation for the active camber mechanism incorporated on the front of a vehicle. The fishhook manoeuvre and the results will be considered first.

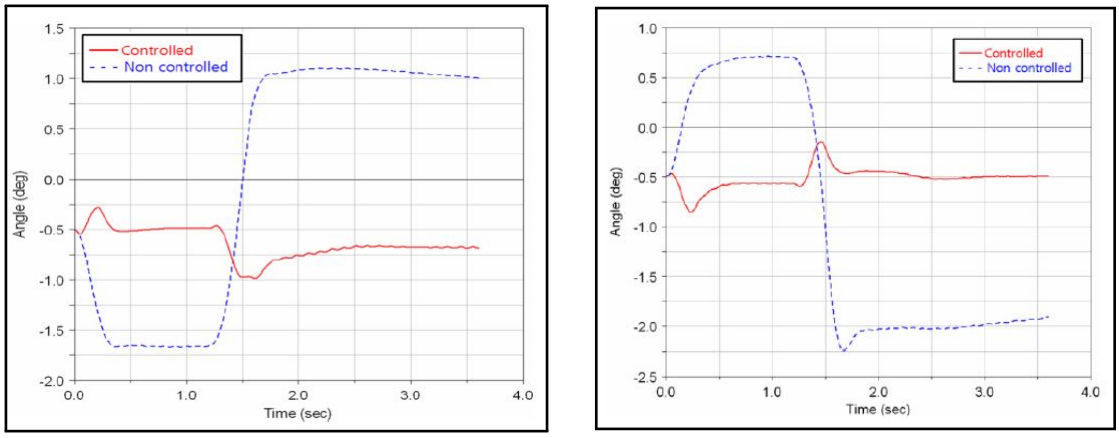

(a) Left Wheel (b) Right Wheel

Figure 2.13: Camber Angle with and without Camber Control **(Park and Sohn, 2012)**

The fishhook manoeuvre is performed by driving between $56.33km/h$ and $80.47km/h$. A rapid steering input of -270° followed by a rapid steering input of 540° in the opposite direction is induced on the vehicle. From the simulation results for the fishhook manoeuvre, **Park and Sohn (2012)** can conclude that the trajectory of the car is improved by reducing the outward drift of the vehicle. Figure 2.13 illustrates how the camber angle is

changed during the fishhook manoeuvre. The yaw rate and side slip angle of the vehicle during the fishhook manoeuvre is illustrated in Figure 2.14 and the roll angle and lateral acceleration is illustrated in Figure 2.15.

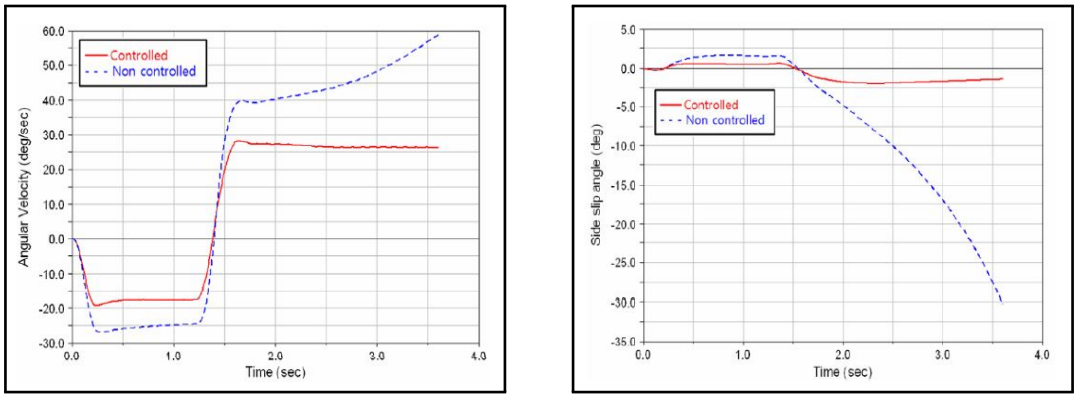

(a) Yaw Rate (b) Side Slip Angle

Figure 2.14: The yaw rate and side slip angle of the vehicle during the fishhook manoeuvre **(Park and Sohn, 2012)**

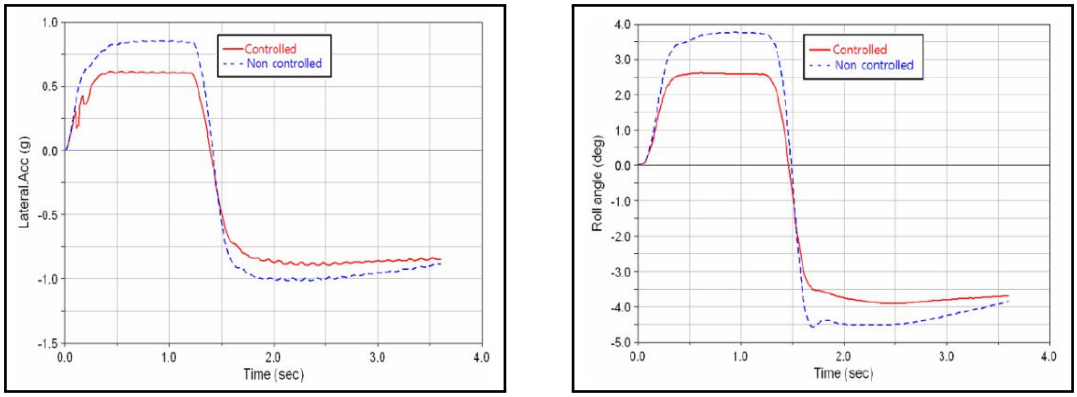

(a) Lateral Acceleration (b) Roll Angle

Figure 2.15: The roll angle and lateral acceleration of the vehicle during the fishhook manoeuvre **(Park and Sohn, 2012)**

From Figure 2.14, the yaw rate of the controlled vehicle is more stable than uncontrolled. Thus, the uncontrolled car suffers from an outward drift towards the end of the manoeuvre. Thus, resulting in the rapid increase of the sideslip angle of the uncontrolled car. However, the sideslip angle for the controlled vehicle remains constant. From Figure 2.15, the roll angle and the lateral acceleration has been decreased with the camber control mechanism. Therefore, from the results in Figure 2.14, it can be seen that the camber control mechanism was able to reduce the yaw rate and the sideslip angle and therefore increases the stability over the uncontrolled mechanism.

The next simulation to be discussed is the single lane-change manoeuvre. The single-lane change is used to evaluate the obstacle avoidance performance of a vehicle. The camber angle of the left and the right wheels during the manoeuvre is illustrated in Figure 2.16. Figure 2.16a corresponds to the camber angle on the left wheel and Figure 2.16b corresponds to the camber angle of the right wheel.

From Figure 2.16, a significant reduction in the camber angle during the lane change manoeuvre is observed to be held at a negative camber angle throughout the manoeuvre.

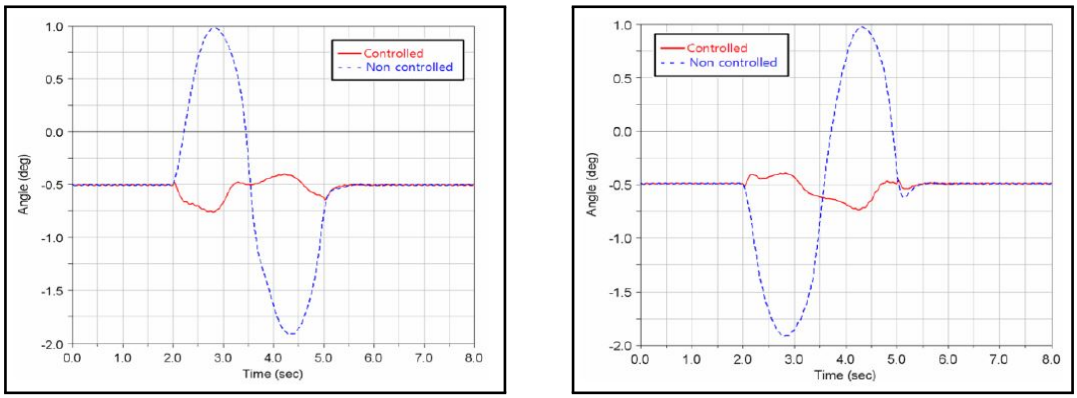

(a) Left Wheel (b) Right Wheel

Figure 2.16: Camber Angle with and without Camber Control **(Park and Sohn, 2012)**

The yaw rate and the sideslip angle for the single lane-change manoeuvre are illustrated in Figure 2.17. From Figure 2.17, the yaw rate with the camber control is reduced compared to without the camber control. The sideslip angle is reduced because of the reduced yaw rate with the camber control mechanism.

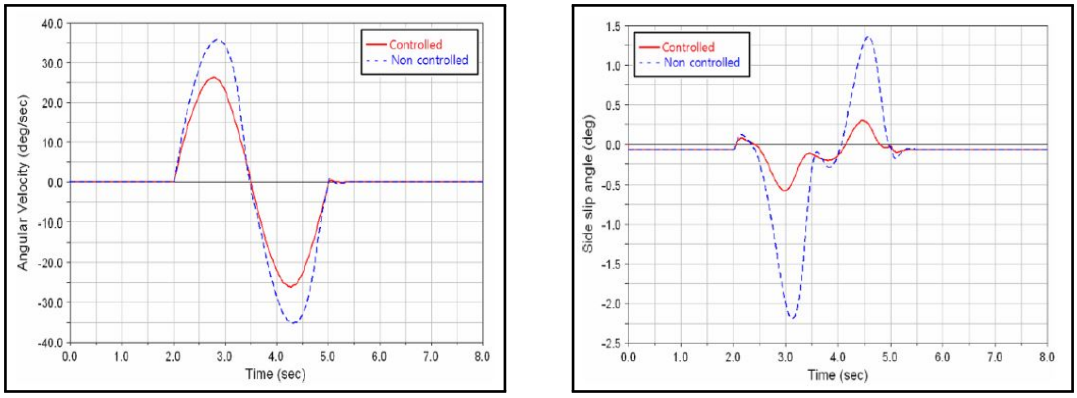

(a) Yaw Rate (b) Side Slip Angle

Figure 2.17: Yaw Rate and Side Slip Angle **(Park and Sohn, 2012)**

Figure 2.18 demonstrates that with the camber angle mechanism, the roll angle and the lateral acceleration of the vehicle are reduced. In conclusion, the ability to actively change the camber angle of the vehicle is beneficial for the stability of the vehicle because it reduces the yaw rate and the sideslip angle of the vehicle. A result of this mechanism is a reduction in the roll angle and the lateral acceleration of the vehicle.

2.7 Case Study: Active camber and toe control strategy for the double wishbone suspension system

A study conducted by **Kavitha et al. (2019)** into actively controlling the camber and toe angle of a double wishbone suspension system to improve handling characteristics of a vehicle, will be investigated in more detail. The investigation was conducted to determine whether it is possible to actively change the camber and toe angle to optimise the traction and manoeuvrability of a vehicle. **Kavitha et al. (2019)** accomplished this by utilising two telescopic arms with actuators to actively change the camber and the toe angle. A

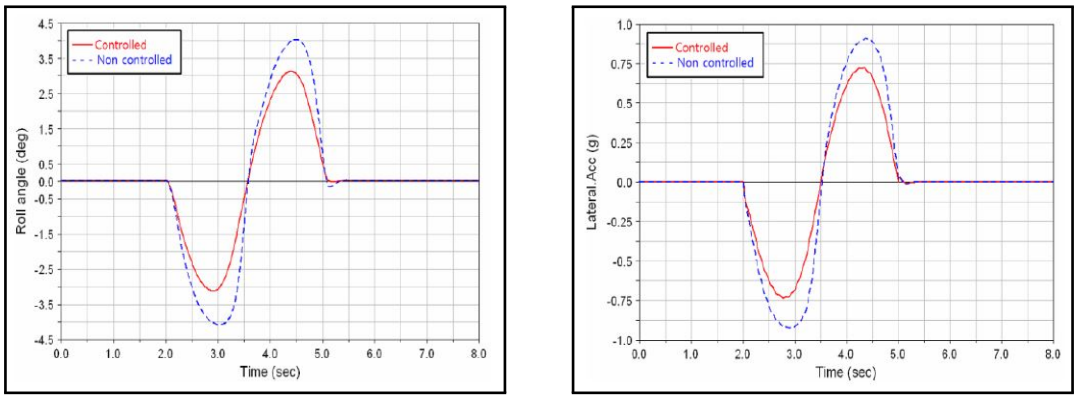

(a) Roll Angle (b) Lateral Acceleration

Figure 2.18: Roll Angle and Lateral Acceleration **(Park and Sohn, 2012)**

vehicle will experience undulations in the camber angle of the wheel when driving over a bumpy road. This phenomenon is due to the suspension geometry of a double wishbone suspension system. As the wheel travels upwards, a negative camber is induced on the wheel. As the wheel travels downwards, a positive camber is induced on the wheel. During this up and down undulation of the wheel, the toe angle is changing due to the suspension geometry of the double wishbone suspension.

Kavitha et al. (2019) developed a quarter car suspension model in SolidWorks **(Dassault Systems, 2020)**. The quarter car model is designed with a double wishbone suspension system with provisions for active camber and toe angle control. This is accomplished by means of actively changing the length of the tie rod and by extending or retracting the upper a-arm. The camber angle is changed by varying the length of the a-arm and the toe angle is changed by varying the length of the tie rod. This is accomplished by using a pair of servo motors, one in the tie rod and one in the a-arm. The retracted and extended a-arm and tie rod designs are illustrated in Figure 2.19.

The camber and toe angles are actively controlled by measuring the camber angle and the toe angle with three sensors. These sensors feed the actual camber and toe angle data into two PID controllers where the desired values are compared to the actual values. The camber and toe angles are changed accordingly, to optimise the suspension geometry for maximum traction over the uneven road surface. The desired camber and toe angles where set as 0 °. This was chosen to optimise the camber and toe angle during cornering for optimal contact area between the tyre and the road. This however remains affected by the suspension geometry.

The simulation and experimental testing were conducted on a sinusoidal road with 150mm amplitude bumps. This is artificially simulated by a hydraulic actuator. The active suspension geometry response for the camber and the toe angle is illustrated in Figure 2.20.

From the simulation results, the maximum camber angle for the passive suspension geometry setup was recorded as 2.8° and 1.151° for the active suspension geometry setup. This reduction in the camber angle results in an optimised tyre road contact area over a bumpy road. The maximum toe angle for the passive suspension geometry setup was recorded as -0.6° and -0.023° for the active suspension geometry setup. This reduction results in an optimised contact patch area for maximum traction. The active suspension geometry system therefore showed a 58% improvement in camber angle characteristics and 96% in

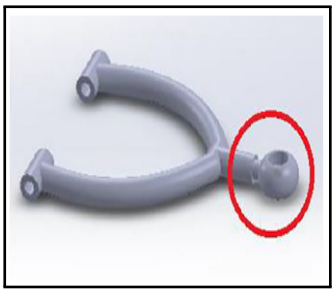

(a) Retracted Upper A-arm

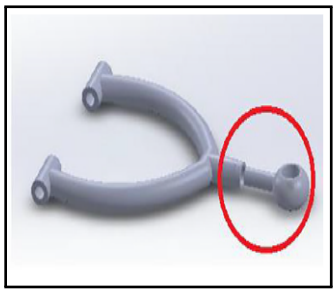

(b) Extended Upper A-arm

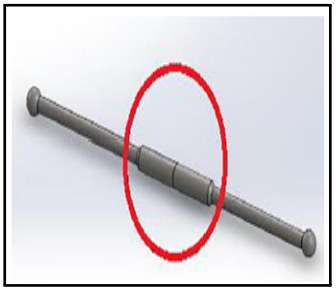

(c) Retracted Tie Rod

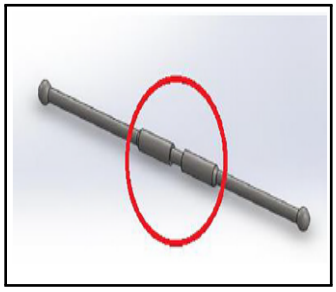

(d) Extended Tie Rod

Figure 2.19: Active Suspension Geometry **(Kavitha et al., 2019)**

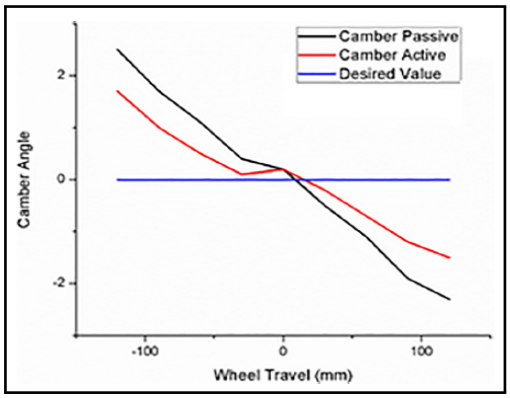

(a) Camber Angle Response

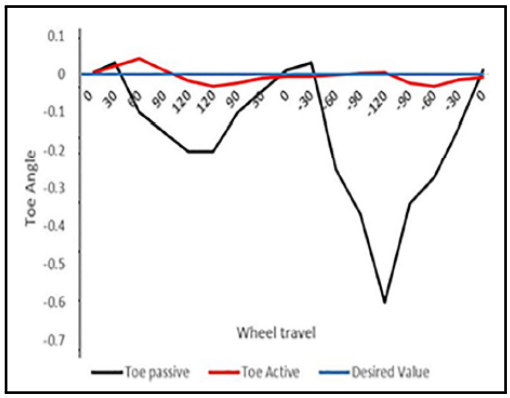

(b) Toe Angle Response

Figure 2.20: Active Suspension Geometry Response **(Kavitha et al., 2019)**

toe angle characteristics when comparing the controlled and uncontrolled results to the desired values.

By utilising active camber and toe angle control methods, **Kavitha et al. (2019)** was able to optimise the contact patch area between the tyre and the road. The system is designed to actuate only when changes are experienced in the system, minimising the energy required for actuation.

2.8 Case Study: Exploiting over-actuation to reduce the tyre energy losses

A study conducted by **Davari (2017)** wherein the possibility of reducing the energy losses during vehicle manoeuvres, by over-actuation was investigated. **Davari (2017)** proposed that there are four main resistive forces for a vehicle to overcome in order to improve the energy efficiency of the vehicle. The four resistive forces are: aerodynamics, inertia, inertial friction and rolling resistance. **Davari (2017)** proposed the use of over actuation methods to reduce the rolling resistance forces and resultantly improve the energy efficiency of the vehicle.

Davari (2017) developed a non-linear Extended Brush Tyre Model (EBM) that can be used for energy studies, with regards to the rolling losses in the tyre. The EBM developed has a flexible carcass, allowing the effects of wheel alignment (slip and camber angle in this case) to be considered during simulations. **Davari (2017)** stated that a vehicle is considered to be over-actuated when the number of actuators that can be controlled is more than the number of states that should be controlled. By having more than one actuator to control a state creates a redundancy in the system and provides a safety mechanism if an actuator fails, another can be used to perform the same function.

Davari (2017) suggests that the lateral force can be controlled by a number of different methods. Direct control of the tyre slip angle, the vertical load, longitudinal force or by direct control of the tyre camber angle. The lateral force generated because of slip and camber angle is illustrated by Figure 2.21. By considering a desired lateral force as a reference force (illustrated by the reference plane in Figure 2.21), the desired lateral force can be maintained by various combinations of slip and camber angles. From Figure 2.21, as the camber angle increases, the desired lateral force can be maintained even at smaller slip angles. Thus, intuitively, it can be stated that the slip loss in the tyre is a function of the slip angle which can be reduced by adding more camber and reducing the slip angle. Therefore, resulting in a reduction in the sliding losses in the tyre **(Davari, 2017)**.

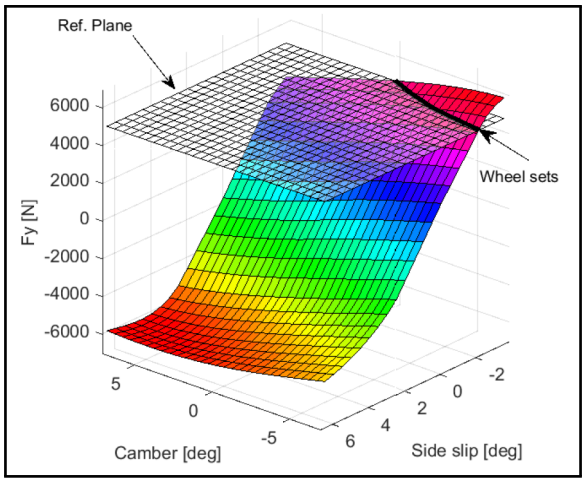

Figure 2.21: Lateral force generated in a vehicle tyre with actuation of the slip and camber angle **(Davari, 2017)**

By developing an algorithm to find the optimal camber and slip angle values to reduce the rolling losses of the vehicle, **Davari (2017)** was able to find the optimal camber and slip angle values that produced the desired minimum rolling losses. The challenge was to find the optimal combination of the actuators that would produce a desired lateral

force. This is because the lateral force is affected by several external variables. The combination of camber and slip angles at various vehicle speeds that produce a similar lateral force is demonstrated in Figure 2.22. At each longitudinal speed, there is a few different combinations of slip and camber angles that will produce the same lateral force.

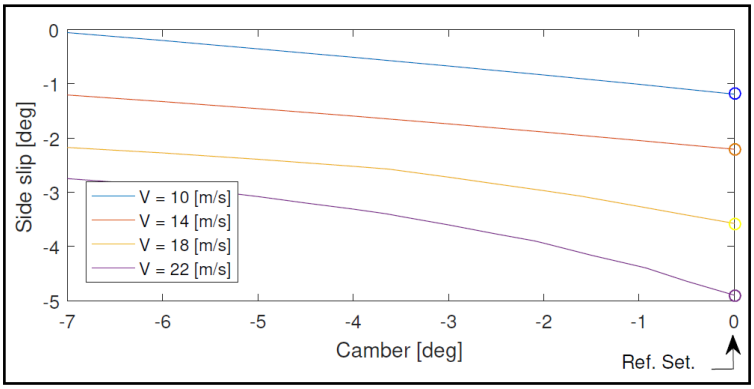

Figure 2.22: Influence of vehicle speed, camber and slip angle at the same lateral force **(Davari, 2017)**

Several different rolling loss elements where considered by **Davari (2017)**. Each rolling loss element is affected differently by changing the camber and the slip angle. After analysing all the best possible combination of camber and slip angles at different speeds, **Davari (2017)** found the optimal combinations of camber and slip angles at the different speeds, that resulted in the minimum rolling losses. It was found that the maximum camber angle at all four speeds provided the greatest savings, illustrated in Figure 2.23a. This however does not mean that the camber angle should be passively set to a constant $-7°$. As the vehicle speed is increased, the slip angle was increased to negotiate the turn. Resultantly, the total power loss also increased, illustrated in Figure 2.23b. This is due to the slip loss increasing as the slip angle is increased.

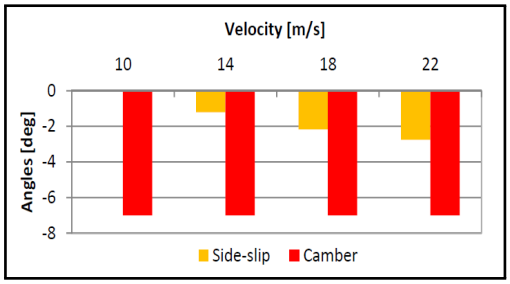

(a) Comparison of optimal camber and slip angles at various velocities.

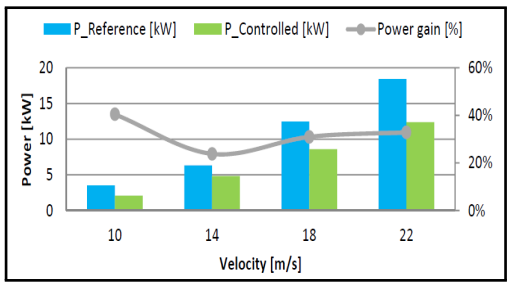

(b) Power saving (gain) of each optimal camber and slip angle combination at various velocities

Figure 2.23: Optimal camber and slip angle combinations and resultant power gains **(Davari, 2017)**

The vehicle used for the study was able to change its camber angle to generate a lateral force in the tyre. Therefore, a camber-side slip control (CSC) strategy was proposed. In a simulation environment with the CSC implemented, **Davari (2017)** was able to reduce the rolling resistance loss by 60%, while maintaining path tracking capabilities. The reduction in the energy consumed is measured by the amount of power used by the in-wheel motors. Therefore, by following the same path at constant speeds, the difference in power consumed by the in-wheel motors between the controlled and uncontrolled strategies can be compared.

By utilising the CSC control strategy, **Davari (2017)** was able to distribute the tyre forces more evenly resulting in a development of greater lateral forces, proving beneficial when driving at the limit. Experimental results showed that over actuation resulted in a reduction in the energy consumption by about 13% for a circular path and 10% for a single lane change, at $10km/h$. Therefore, over actuation has proven as a possible control strategy to reduce the energy consumed.

2.9 Case Study: The energy efficiency of implementing camber control

A recent study conducted by **Sun et al. (2018)** into the possibility of improving the power efficiency of vehicles by implementing camber control was investigated for this section of the thesis. They investigate the amount of power that can be saved by implementing a camber control method. This investigation is conducted by studying the effects of changing the camber angle will have on the forces and the moments of the tyres, under various driving conditions. **Sun et al. (2018)** use the magic tyre formula for combined slip and camber angle simulations to compute the forces and moments acting between the tyres and the road. The calculations for the power loss during cornering is formulated with equations derived from a two-track yaw-plane model.

$$T - M_y cos\gamma - M_z sin\gamma - F_x R_0 = I_w \dot{\omega} \tag{2.7}$$

Sun et al. (2018) has defined the power for propelling the wheels P_w, expressed in equation 2.8. The power of propulsion is expressed as the sum of the products of the driving moment and angular velocity of each wheel.

$$P_w = \sum_{i=1}^{4} T_i.\omega_i \tag{2.8}$$

After all the substitutions for all the components where completed, equation 2.8 is transformed into equation 2.9.

$$P_w = P_{arl} + P_{rrl} + P_{long\ slip} + P_{lat\ slip} + P_{long\ acc} + P_{wal} + P_{yal} + P_{lat\ acc} + P_a \tag{2.9}$$

Where,

$$P_{arl} = F_{ar} V_x \tag{2.10}$$

$$F_{ar} = \frac{1}{2} C_{ar} \rho\ A {V_x}^2 \tag{2.11}$$

$$P_{rrl} = \sum_{i=1}^{4} \left(M_{yi} cos\gamma_i + M_{zi} sin\gamma_i\right) \omega_i \tag{2.12}$$

$$P_{long\ slip} = \sum_{i=1}^{4} F_{xi} K_i V_i \tag{2.13}$$

$$P_{lat\ slip} = \sum_{i=1}^{4} \left(-F_{yi} \alpha_i\right) V_x \tag{2.14}$$

$$P_{long\ acc} = m\dot{V}_x V_x \tag{2.15}$$

$$P_{wal} = \sum_{i=1}^{4} I_w \dot{\omega}_i \omega_i \tag{2.16}$$

$$P_{yal} = I_z \ddot{\psi}\dot{\psi} \tag{2.17}$$

$$P_{lat\ acc} = m\dot{V}_y V_y \tag{2.18}$$

$$P_a = (F_{y1}\alpha_1 - F_{y2}\alpha_2 + F_{y3}\alpha_3 - F_{y4}\alpha_4)\left(\frac{t_w}{2}\dot{\psi}\right) - (F_{x1}\delta_f + F_{x2}\delta_f)\left(V_y + \dot{\psi}l_f\right) \tag{2.19}$$

The required power for controlling the camber angles of each wheel is computed as the sum of the products of the overturning moment M_{xi} and the derivative of the camber angle $\dot{\gamma}_i$. The power loss is not considered when the product is smaller than zero. Lastly, the power loss during cornering is defined as the sum of the power loss of the wheels and the camber angle, as illustrated in equation 2.21 **(Sun et al., 2018)**.

$$P_{camber} = \sum_{i=1}^{4} M_{xi}\dot{\gamma}_i \ (M_{xi}\dot{\gamma}_i < 0,\ i = 1, 2, 3, 4) \tag{2.20}$$

$$P_{all} = P_w + P_{camber} \tag{2.21}$$

To investigate the contribution of the camber angle to the power saving of a vehicle during cornering, **Sun et al. (2018)** designed a path and a driver model to follow the path at reference velocity. The vehicle is assumed to follow the path at a constant velocity. The torque on all four wheels is assumed to be equal. The range for the camber angles are $[-15°, 15°]$ and for the steering angles $[0°, 25°]$. The camber angle on the front and the rear wheels are also assumed to be equal, such that $\gamma_1 = \gamma_2$ and $\gamma_3 = \gamma_4$. The driver model is illustrated in equation 2.22. Δy_1 is the lateral offset between the vehicle and the road at the current position. Δy_2 is the lateral offset at the preview distance l and $\Delta\psi$ is the yaw angle offset. k_y, k_l and k_ψ are the corresponding gains for each input.

$$\delta_f = k_y \Delta y_1 + k_\psi \Delta\psi + k_l \Delta y_2 \tag{2.22}$$

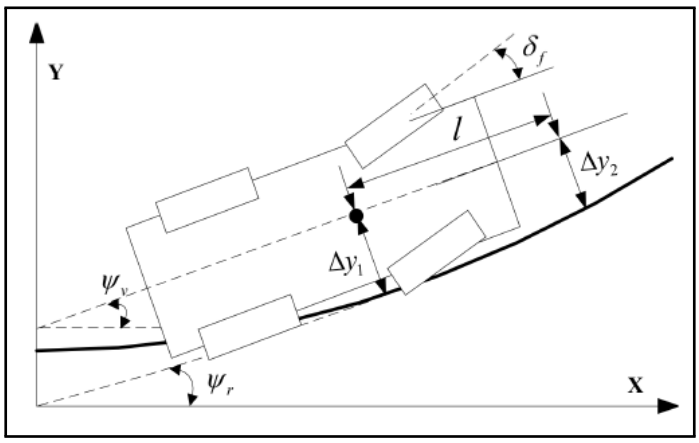

Figure 2.24: Vehicle Steering Controller **Sun et al. (2018)**

The relationship between the camber angles and the front steering angle is illustrated in equation 2.23 and 2.24. K_{12} and K_{34} are coefficients used to determine the relationship between the camber and steering angles. The inputs to the camber angles on the front and the rear are given in equations 2.23 and 2.24 respectively.

$$\gamma_1 = \gamma_2 = \begin{cases} K_{12}\delta_f, & |K_{12}\delta_f|15^\circ \\ \sin(K_{12}\delta_f).15^\circ, & else \end{cases} \tag{2.23}$$

$$\gamma_3 = \gamma_4 = \begin{cases} K_{34}\delta_f, & |K_{34}\delta_f|15^\circ \\ \sin(K_{34}\delta_f).15^\circ, & else \end{cases} \tag{2.24}$$

The relationship between K_{12} and K_{34} is as follows: If K_{12} and K_{34} are greater than zero, the camber of the front and the rear wheels are in the same direction. Otherwise, they are in opposite directions. The greater the K_{12} and K_{34} values are, the more power is required for camber control, illustrated in Figure 2.25 (d) **(Sun et al., 2018)**.

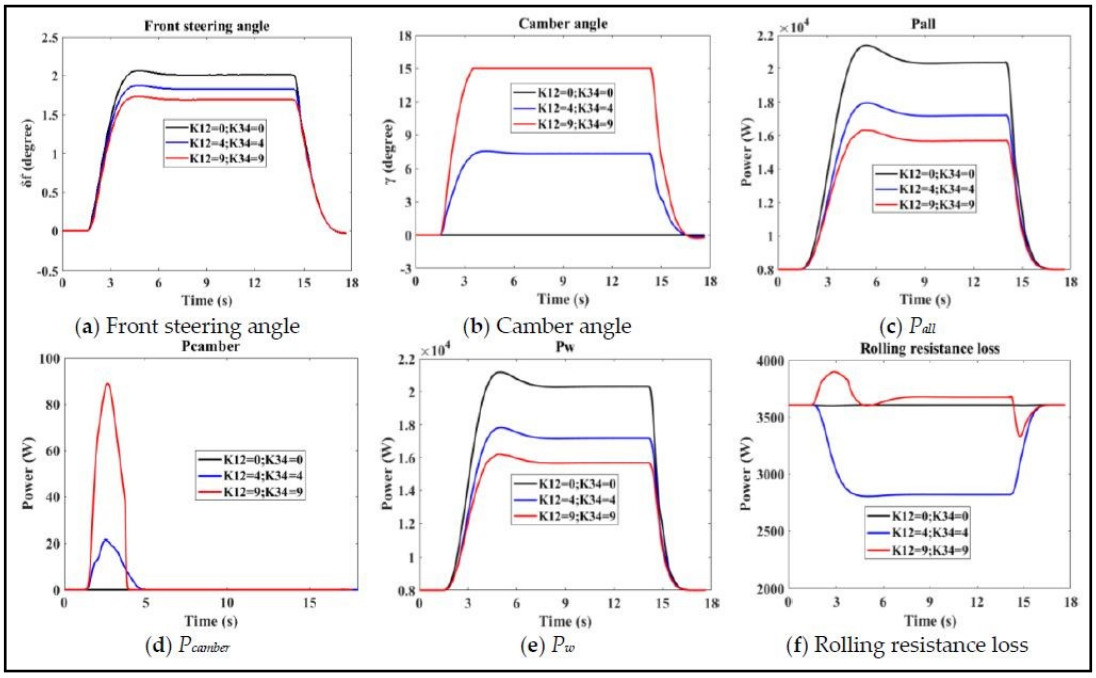

Figure 2.25: Simulation results showing steering and camber angles as well as power losses from **Sun et al. (2018)**

Sun et al. (2018) have found that although camber control costs power to operate, the total power loss is still reduced with camber control. Figure 2.25 and Figure 2.26 represent the simulation results with $R = 100m$ and $V_x = 88.18km/h$. Figure 2.25 demonstrates in (d) that the camber requires power to control. It also shows that the greater the K_{12} and K_{34} values are, the more power is required to control the camber. Also from (b), it is clear that the higher the K_{12} and K_{34} values, the greater the camber angle on the wheels. From (c), it can be seen that the total power loss is decreased as the K_{12} and K_{34} values are increased and consequently the camber angles are increased. A reduction in power loss is observed in (e), (g), (h), (i), (j) and (l) in Figure 2.25 and Figure 2.26.

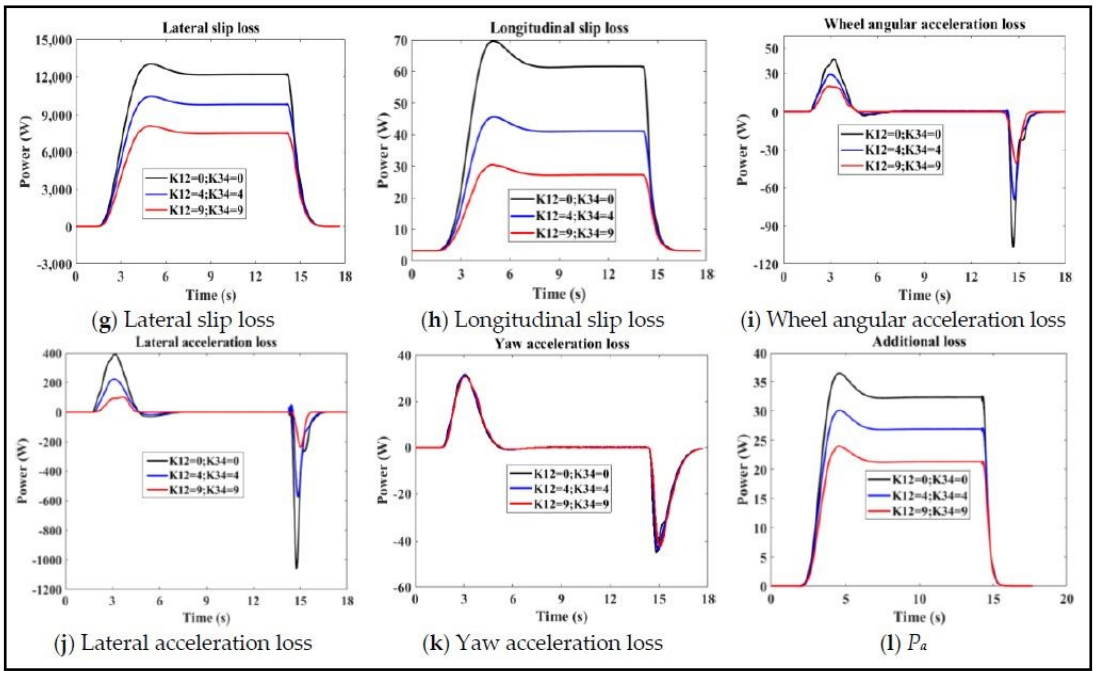

Figure 2.26: Simulation results showing steering and camber angles as well as power losses from **Sun et al. (2018)** Continued

2.10 Case Study: Motion Modelling and Control Strategies of Over-Actuated Vehicles

A study conducted by **Edrén (2014)** on the effects of utilising the ability of over-actuating a vehicle in order to investigate the effect on the performance, safety and efficiency will be discussed in more detail. By using optimal control of actuators for controlling the camber and the steering angle of the wheels, a significant improvement in the efficiency, performance and safety of the vehicle during evasive manoeuvres are observed.

Edrén (2014) made use of several tyre models for various different aspects of the investigation. The magic formula tyre model was used in many levels of complexity. The brush tyre model was used in a numerical model to physically describe the forces in the tyre at large camber angles. Finally, to study the effect of the camber angle on the tyre forces, a multi-line brush tyre model was developed. The multi-line brush tyre model comprises of three longitudinal contact lines that contains fifty bristles with varying stiffness, depending on the direction of the load in the bristles. The sum of the vector forces and torques on all the bristles equates to the resultant forces and torques acting on the tyre. The multi-line brush tyre model incorporates a flexible lateral carcass for load sensitivity. Finally, a Simple Magic Formula (SMF) tyre model was constructed to behave in a comparable manner to the multi-line brush tyre model. The SMF was developed to take the lateral slip angles, longitudinal forces and the camber angles as inputs and returns the lateral forces as the outputs.

Three distinct vehicle models where developed and used during the study. A simple particle model, where all vehicle mass is assumed to be central with no rotational degrees of freedom being experienced by the vehicle model. The second is the intermediate model with six degrees of freedom which includes the contribution of the springs, dampers and anti-roll bars. Finally, the third model used is a fully validate full vehicle model. The vehicle was

modelled and simulated in Dymola. The vehicle includes full suspension kinematics and compliances in the bushings and the material deflections experienced when cornering.

To explore the energy efficiency due to over actuation, a Consumer Union, double lane change manoeuvre was selected as the evasive manoeuvre. The vehicle was driven through the evasive manoeuvre where optimisation is used to control the individual steering angles and wheel torques. The study was conducted to determine which combination of an over-actuated vehicle delivers the greatest mechanical power saving. The results from the energy efficient cornering as found by **Edrén (2014)**, is shown in Table 2.4. Six vehicle configurations with various combinations of the following actuator configurations was tested: Front Axle Steering (FAS), Four Wheel Drive (4WD), All Wheel Drive (AWD), Individually controlled AWD (i-AWD), All Wheel Steering (AWS) and Rear Axle Steering (RAS).

Table 2.4: Results Relating to Energy Efficient Cornering **(Edrén, 2014)**

Configuration	**Actuator Configuration**	**Consumed Energy or Cost [J]**	**Difference Relative to the Highest Consumed Energy [%]**
A	FAS + 4WD	4312.4	0
B	FAS + i-AWD	4302.7	-0.226
C	FAS + RAS + 4WD	3940.3	-9.443
D	FAS + RAS + i-AWD	3939.8	-9.456
E	AWS + 4WD	3868.7	-11.467
F	AWS + i-AWD	3861.9	-11.666

2.11 Case Study: Influence of Active Subsystems on Electric Vehicle Behaviour and Energy Characteristics

The study of the influence of active subsystems on electric vehicle behaviour and its energy characteristics was investigated by **Shyrokau et al. (2014)**. The investigation was aimed at determining the potential impact of each vehicle subsystem on the vehicle dynamic behaviour for both steady-state and transient vehicle behaviour. **Shyrokau et al. (2014)** also set out to determine the total energy consumption and energy losses due to the individual demands on the vehicle energy, from each of the individual subsystems. The subsystems included in this investigation is:

- Individual Front Wheel Steering (IFS)
- Individual Rear Wheel Steering (IRS)
- Traction/Brake Torques Generated by Electric Motors (IEM)
- Friction Brake System (FBS)
- Active Camber System (ACS)
- Dynamic Tyre Pressure System (APS)
- Additional Normal Forces Generated by External Spring, Damping and Stabilizer Forces (ARzS)

A control system was developed by **Shyrokau et al. (2014)** that uses a reference generator for the vehicle dynamics controller, which compares the actual vehicle dynamic behaviour to the reference desired vehicle dynamic behaviour, to determine the desired control demand. The control demand is distributed between the vehicle subsystems and wheels, converting them to reference actuator signals during the control allocation of the control demand. Simple control algorithms are used for the individual actuator control.

Three different tests were conducted by **Shyrokau et al. (2014)**. A slowly increasing steer test, a step steer test and a sine sweep test. The energy characteristics for the slow increasing steer test is depicted in Figure 2.27. The energy characteristics for the step steer test is depicted in Figure 2.28 and finally, the energy characteristics for the sine sweep test is depicted in Figure 2.29.

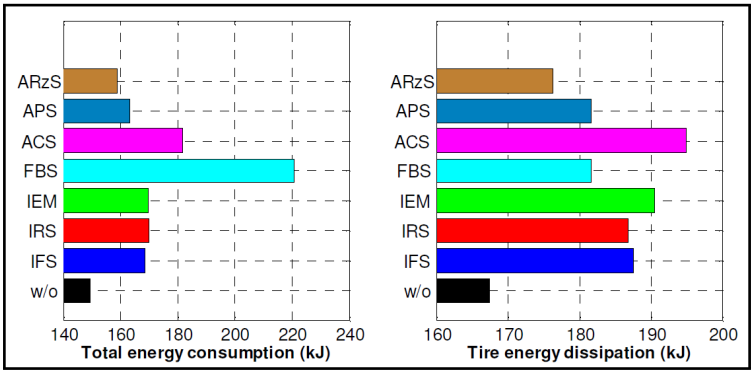

Figure 2.27: Energy Characteristics of the Slow Increasing Steer test by **Shyrokau et al. (2014)**

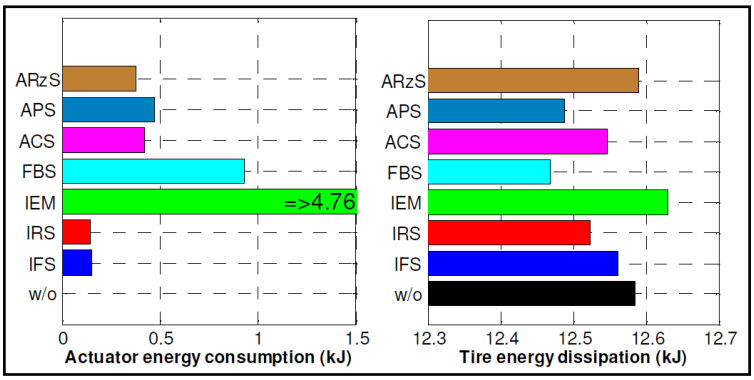

Figure 2.28: Energy Characteristics of the Step Steer test by **Shyrokau et al. (2014)**

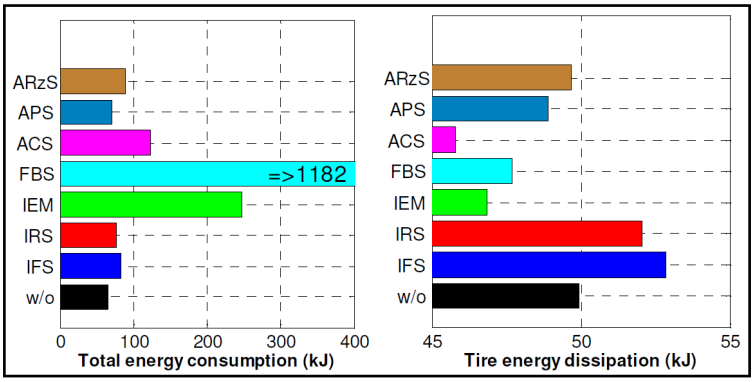

Figure 2.29: Energy Characteristics of the Sine Sweep test by **Shyrokau et al. (2014)**

The results of the slowly increasing steer test from Figure 2.27 indicate that the FBS has the highest maximum total energy consumed of $221kJ$ and ACS indicated the highest energy dissipation in the tire at $195kJ$. For the step steer test, indicated in Figure 2.28, the results indicate that the highest actuator energy is consumed with IEM at $4.7kJ$ and the lowest for IRS with $0.14kJ$. The IEM indicated the highest tyre energy dissipated at $12.64kJ$. Finally, the results for the sine sweep steer test, depicted in Figure 2.29, indicate that the FBS resulted in the highest total energy consumed at $400kJ$ and IFS indicated the highest energy dissipated at $53kJ$.

With a subjective assessment of the influence of each individual subsystem on the energy efficiency, it was concluded that the IFS and the IRS yielded the most favourable results (with the least amount of energy consumed). The ACS was mentioned as a neutral, no effect subsystem when considering the energy consumed. When considering the tyre energy losses, the FBS showed the most favourable results and again, the ACS was considered a neutral, no effect subsystem **(Shyrokau et al., 2014)**.

2.12 Case Study: Assessing the Impact of Cornering Losses on the Energy Consumption of Electric City Buses

In an investigation conducted by **Beckers et al. (2020)**, the impact of cornering losses on the energy consumption of Battery Electrical Buses (BEB) was investigated. The investigation was done because conventional control algorithms do not consider energy losses which occur during cornering of a vehicle on curvy roads. **Beckers et al. (2020)** set out to model, investigate and asses the additional energy consumption during steering of a BEB.

Based on the findings, a nonlinear cornering model was developed which can consider the additional energy losses during cornering. The model uses large steering inputs, load transfers and a MF tyre model. The results obtained from various constant radius test at various vehicle velocities indicated that the cornering resistance and the tyre scrub of the rear tyres contributed additional energy losses which are not accounted for in conventional energy prediction models. The cornering resistance power and the tyre scrub power losses are illustrated in equation 2.25 and 2.26 respectively **(Beckers et al., 2020)**.

$$P_{cRes} = \sum_{i=3}^{6} F_{x,i}\nu_{x,i} \tag{2.25}$$

$$P_{scrub} = \sum_{i=3}^{6} F_{x,i}(-\nu_{x,i} + r_{e,i}\omega_i) \tag{2.26}$$

The results from the investigation into the amount of power losses due to the cornering resistance forces and the tyre scrub is graphically depicted in Figure 2.30a and Figure 2.30b respectively. These results are displayed for varying conditions of cornering radii and vehicle velocity.

The combined losses between the cornering resistance loss and the tyre scrub loss are the combined cornering loss (P_{loss}). The combined cornering loss is defined as the power required from the vehicle's motor to overcome the losses. A validation of the vehicle

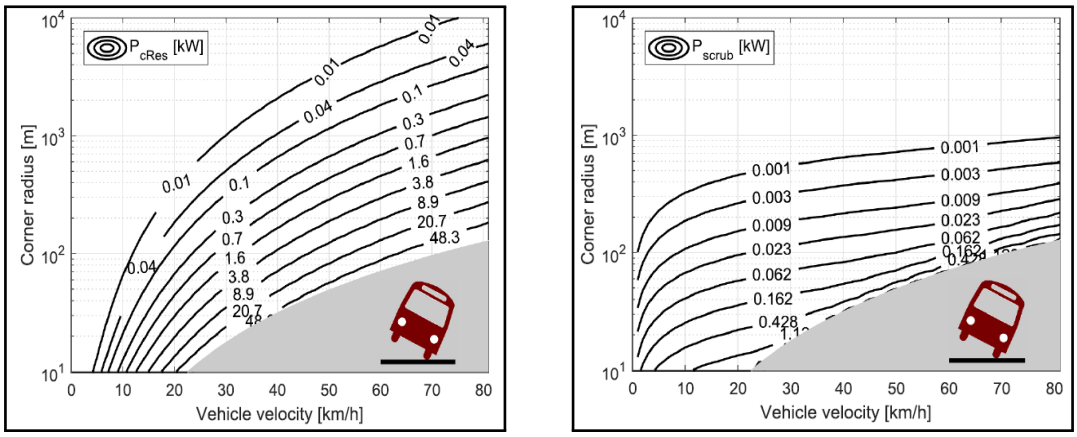

(a) Cornering Resistance Power Loss

(b) Rear Wheel Tyre Scrub

Figure 2.30: Resulting Energy Losses **(Beckers et al., 2020)**

model was done with full scale vehicle tests and the results indicated an average deviation of $0.8kW$ between the vehicle model and the measured data. Finally, after experimental testing was concluded, **Beckers et al. (2020)** found that the combined cornering losses equates to 3.1 % of the BEB's total powertrain losses. This number increases to 5.8 % when routes that cross city centres are being considered. **Beckers et al. (2020)** concluded that cornering losses should be considered when modelling the energy consumption predictions of a vehicle.

2.13 Case Study: Integrated Vehicle Control of an In-Wheel-Motor Vehicle to Optimize Vehicle Dynamics and Energy Consumption

In a brief investigation conducted by **Hirano (2012)** into the integrated control for optimized vehicle dynamics and energy consumption, the author set out to develop an integrated control method for controlling the driving/braking torque, steering angle and the camber angle of each individual wheel of an in-wheel-motor vehicle. The author merely set out to create a template for control. The energy to control the steering and camber angle actuation was not considered in this study. The simulation model consists of a vehicle model and a driver model for path following purposes. The vehicle model is enabled for individual control of the steering and the camber angle and includes a three-dimensional multibody dynamics model of the vehicle suspension and the vehicle body. The driver model is able to calculate the required steering, driving and braking torques.

No real simulation studies were conducted by **Hirano (2012)** since this model is only created as a baseline model that can be used for further investigations. The tentative path following results showed that there is considerable improvement necessary for the vehicle to follow a desired trajectory and be usable in any sensible manner.

2.14 Discussion of Current Camber Control Solutions

As previously discussed, the research on camber control methods is limited with little information available. Solutions presented by **Park and Sohn (2012)** and **Sun et al. (2018)** was discussed in the previous sections. The control methods presented by **Park and Sohn (2012)** and **Sun et al. (2018)** are two quite different approaches to controlling the camber angle of a vehicle.

Park and Sohn (2012) aimed their investigation on improving the vehicle's dynamic handling, by utilizing a yaw rate control strategy. The control strategy takes a reference yaw rate and the actual vehicle yaw rate and compares the two and computes the error. The camber controller is designed to change the camber angle on the front wheels to minimize the error between the reference yaw rate and the actual yaw rate. The desired camber angle is calculated with the actual steering wheel angle and the vehicle velocity. This control strategy is setup to change the geometry of the vehicle suspension system to ensure that the camber angle on the front wheels is continuously kept negative. Figure 2.13 and Figure 2.16 illustrated the effectiveness of the camber control strategy for a fishhook and single lane change manoeuvre respectively.

Kavitha et al. (2019) proposed active camber and toe angle control to optimise the contact patch area between the tyre and the road. They proposed that by using a set of actuators, each individually controlling either the camber or the toe angle during driving on uneven roads, they will be able to optimise the contact area between the tyre and the road. **Kavitha et al. (2019)** designed two separate PID controllers to optimise the suspension geometry when driving over undulating terrain. Therefore, improving the lateral dynamic behaviour of the vehicle. The controller is designed to actuate only when necessary, minimising the energy required for actuation.

Kavitha et al. (2019) showed promising results in improving the camber and toe angle over rough terrain, but little mention was made with respect to how this controller would affect the vehicle's power consumption. This controller however was designed to primarily improve the vehicle stability, rather than reducing the power losses. The possibility of adapting this control strategy for power loss investigations is particularly good due to the simple design of the system.

The process of reducing the rolling losses in the tyres of a vehicle by means of over actuation was proposed by **Davari (2017)**. **Davari (2017)** developed a camber-side slip (CSC) controller that can actively control the slip and camber angles of a vehicle, to minimise the rolling losses. An Extended Brush Tyre Model (EBM) was developed to aid the investigation and to accurately simulate the behaviour under different camber and slip angle conditions. **Davari (2017)** found that there is a number of different methods to generate a lateral force in the tyre. By exploring alternative ways to develop a lateral force in the tyre, **Davari (2017)** was able to reduce the rolling losses in the vehicle tyre.

Davari (2017) accomplished this by actively actuating the slip angle and the camber angle of the vehicle. From the tyre level simulations, it was seen that to maintain a certain lateral force in the tyre, the camber angle can be increased and resultantly, the slip angle decreased. By decreasing the slip angle, a reduction in the sliding losses of the tyre is experienced. The optimal combination of camber and slip angle at various speeds was determined and a complex controller was designed. **Davari (2017)** was able to generate a power saving of more than 12% and 6% for a circular constant curve test at 10 kph and 20 kph respectively. A power saving of 10% and just over 2% was experienced

during a single lane change manoeuvre at 10 kph and 20 kph respectively.

The camber control strategy presented by **Sun et al. (2018)** takes a very different approach. The aim of the study was to reduce the power losses in a vehicle with the help of camber control. Therefore, it is expected that the camber control strategy differs to that presented by **Park and Sohn (2012)**. **Sun et al. (2018)** initially started with a simple gain multiplier as a camber input. The simple gain multiplier control strategy was evaluated with three gain values. The gain values on the front and the rear wheels were kept identical for these tests. The path used for the analysis is kept constant.

The initial simulation analysis by **Sun et al. (2018)** was used as a proof of concept. The simulations showed promising results. Based on their initial findings, **Sun et al. (2018)** took the proof of concept, and used it to develop a method to actively control the camber angle on the wheels. By using a mathematical vehicle model, **Sun et al. (2018)** developed a more comprehensive test to determine and investigate the simulation results at various parameters. The investigation was extended to three different constant radius paths with 6 lateral accelerations on all three paths. By evaluating the percentage of energy saved, **Sun et al. (2018)** was able to determine the optimal relationship between camber angle and lateral acceleration. This newfound relationship was used as the input to the camber controller. The percentage power saved can be computed by equation 2.27.

$$\eta = \frac{\int P_{all}(0,0)dt - \int P_{all}(K_{12}, K_{34})dt}{\int P_{all}(0,0)dt} \times 100\% \tag{2.27}$$

The optimal values are illustrated in Figure 2.31. The power saving results from the simulations was illustrated in Figure 1.2. From the simulation results, **Sun et al. (2018)** concluded that the higher the lateral acceleration is, the greater the power loss reduction is.

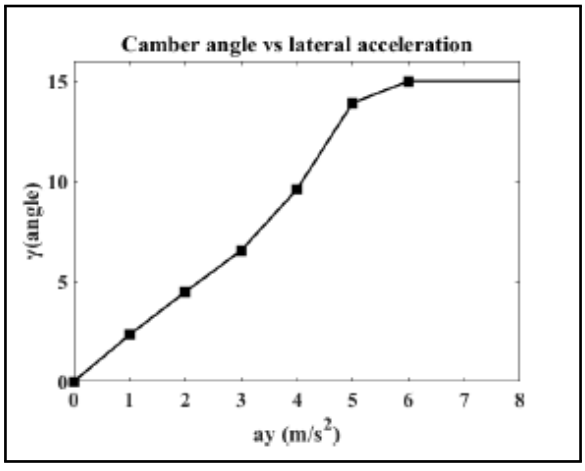

Figure 2.31: Camber Angle versus Lateral Acceleration **(Sun et al., 2018)**

The investigation by **Edrén (2014)** was included because of the vast number of various combinations of over-actuated control strategies that where investigated. The combination of all wheel steering and individually controlled all-wheel drive resulted in the highest reduction in the energy consumption of 11.666 %.

An investigation into the influence of the active subsystems on electric vehicle behaviour was completed by **Shyrokau et al. (2014)**. **Shyrokau et al. (2014)** set out to inves-

tigate the impact of each individual vehicle subsystem on the power losses during steady-state and transient cornering conditions. From the investigation, it can be concluded that the power losses in each subsystem is heavily dependent on the type of manoeuvre being considered with the ACS scoring a neutral score in the subjective analysis of the results.

The investigation into the impact of the cornering losses on the energy consumption of BEB's was conducted by **Beckers et al. (2020)**. **Beckers et al. (2020)** found that the contribution of the cornering resistance power losses and the tyre scrub power losses resulted in a noticeable contribution to the powertrain losses. **Beckers et al. (2020)** concluded that a powertrain loss of 3.1 % for the BEB was observed and that value increases to 5.8 % when travel across city centres are considered.

2.15 Conclusion

From the literature review, the state-of-the art solutions to the research question was discussed in more detail. It is concluded that the behaviour of the tyre will directly impact the camber angle and resultantly the power losses caused by the addition of the camber angle. From literature, it is evident that there is limited information on the effect of camber angle on the power loss in the tyre. However, from the limited literature, the possibility of utilising the camber angle to reduce the power loss in tyres should be further investigated.

The literature survey has shown that there are promising research projects, which tackled the problem of investigating a method of controlling the camber angle, to improve vehicle dynamic behaviour and to reduce the power loss in the tyre. The challenge with the camber control investigation, other than finding literature, is to fully understand the vehicle tyre being used for the investigation. A more in-depth investigation into the vehicle tyre model that will be used in this study will be described in more detail in the chapter 3.

Chapter 3

Tyre Simulations

The simulation work is used as the first step to a proof of concept. The investigation of camber control on the lateral dynamics and power efficiency of a vehicle is initially conducted on a tyre level. To know how a vehicle will respond to a camber change, the effects must first be investigated on a tyre level. If tyre level simulations show promising results, there is a good chance that the full vehicle simulations will follow suit.

3.1 Tyre

The tyre used throughout the simulations is the Pirelli Scorpion Verde 235/55 R19 105V all-season tyre. The tyre simulations were conducted with a nominal tyre pressure of 2.5 bar. The tyre is considered directional due to its asymmetric tread pattern. The tyre model used for the simulations is based on a parameterized FTire model of the Pirelli Scorpion tyre. The parametrization of the tyre was done by **Wright (2017)**. During this process, **Wright (2017)** had to parametrize the two main components of the tyre model, namely, the structural model and the tread-road contact model. The parametrisation is done by acquiring test data from the tyre, to identify specified parameters in the FTire tyre model. **Wright (2017)** used FTire/fit software to parametrise the tyre. **Gipser and Hoffmann (2016)** have recommended tests that should be used for the parameterisation of a tyre. The recommended tests were executed by **Wright (2017)**.

3.2 Drum Test Rig

The parameterization process and the results were discussed in section 2.4.3. The investigation into camber control and the vehicle dynamic response and power efficiency thereof, requires a tyre model that is fully validated with trustworthy data. Therefore, after careful consideration, it was concluded that the Pirelli Scorpion tyre validated by **Wright (2017)** will yield results that accurately represent the behaviour of the tyre in real life situations. With a trusted tyre model, the process of simulating the behaviour of the tyre under various camber angle and slip angle conditions can commence. For the purposes of investigating the tyre behaviour, a simulated drum test rig was designed. It is important to note that the drum test rig simulations were initially designed to be experimentally validated on the actual drum test rig. This however was never executed due

to the pandemic and the lockdown experienced during the completion of this study.

A drum test setup was designed to simulate the actual drum test rig of the Vehicle Dynamics Group (VDG). The actual validation of the simulated data is outside the scope of this thesis, but the model will enable future validation of a tyre on the drum test rig. A drum test rig also enables the testing of a tyre in a controlled laboratory environment. Thus, allowing for all year testing irrespective of weather, test facility availability and a mobile test rig to test at test facilities.

The purpose of the drum test rig is to design a tool that can simulate the tyre in a controlled environment, which can be replicated with real world tests. The drum test rig was designed in SolidWorks **(Dassault Systems, 2020)** and imported into MSC ADAMS **(MSC Software, 2013)** for multibody dynamics simulations. The model is developed purely to simulate the tyre behaviour on a drum test rig, as accurately as possible.

The ADAMS model of the Drum test Rig consisting of 6 rigid bodies and a tyre. The entire drum test rig has five Degrees of Freedom (DOF). The graphical topology in Figure 3.1 illustrates the connections of the different bodies with the various joints used. The back plate is constrained to ground with a translational joint allowing movement in the vertical direction. This is to allow the drum and ultimately the tyre to move in the vertical axis onto the actual drum. The pivot plate is connected to the back plate with a revolute joint. This allows the pivot plate and all the bodies connected to it to pivot around the x-axis to simulate the effects of camber angle. The upper and lower arms are connected to the pivot plate with fixed joints. This ensures that the tyre is mounted in a fixed position and ensures that the entire wheel assembly with the pivot plates moves as one to a specified camber angle. The upright is connected to the upper and lower arms with a single revolute joint. The revolute joint allows for rotation around the z-axis to simulate the effect of steering the wheel.

Finally, the wheel and tyre are connected to the upright with a revolute joint, allowing for rotation around the y-axis, enabling the wheel to roll freely. The drum is connected to ground with a revolute joint allowing rotation in the y-axis. Two motions and one force are imposed on the model. The slip and camber angle inputs are controlled with motions taking inputs from SIMULINK **(Mathworks, 2020)**. The motion controlling the camber and slip angles each remove one DOF, bringing the model's DOF's down to three. A vertical applied force on the back plate, is used to simulate the effects of changing the vertical load on the tyre. The rotational speed of the drum was set to 10 rad/s.

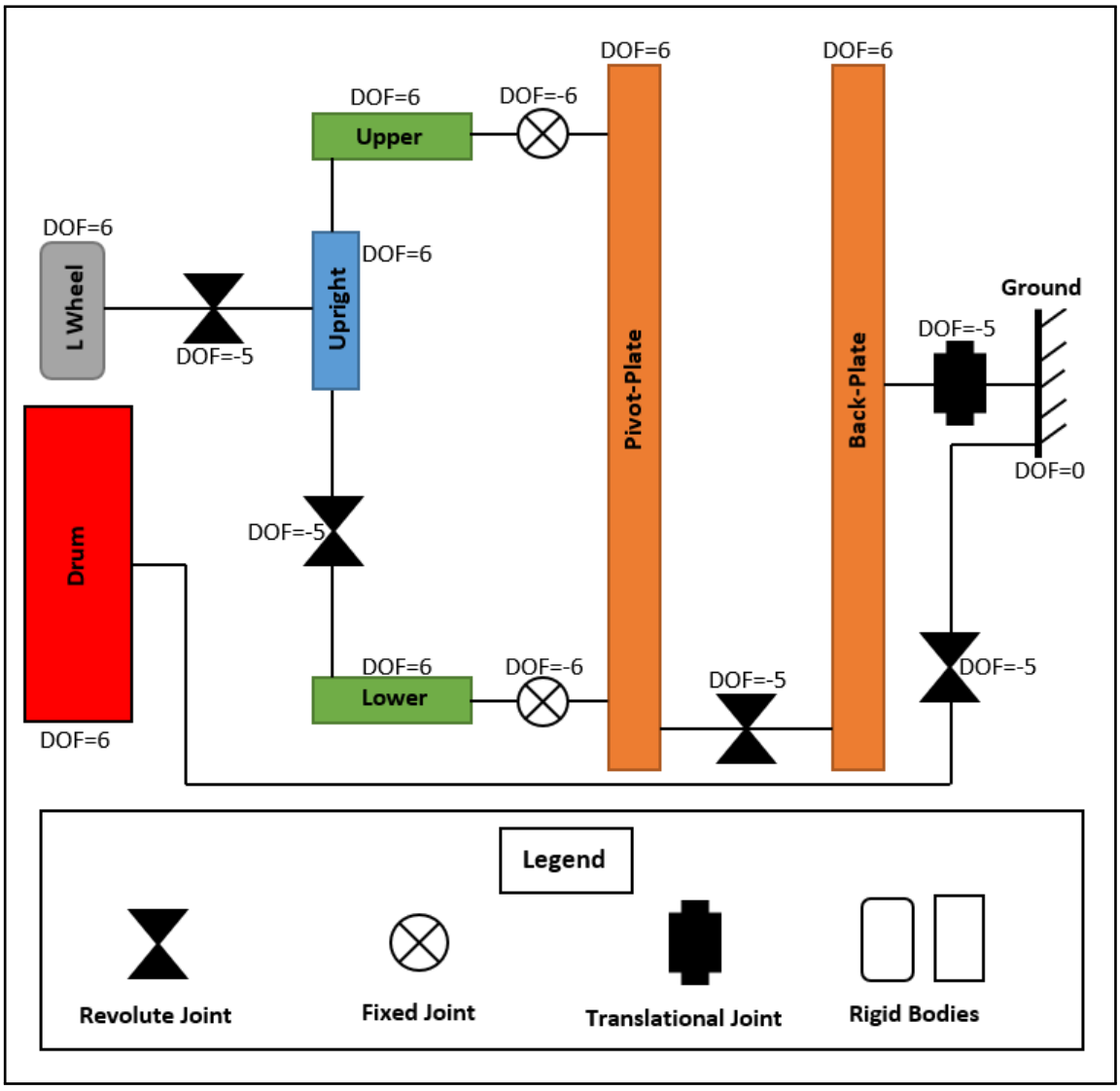

Figure 3.1: Schematic diagram of the Drum test Rig

The type of motion and the Degrees of Freedom for the different bodies are listed in Table 3.1. The number of DOF's in Table 3.1 are calculated without the motion for the camber and slip angles, which removes 2 DOF's for the L Wheel, 2 DOF's for the upright and finally removes 1 DOF for the upper, lower and the pivot plate.

Table 3.1: Degrees of Freedom without motion defining camber and slip angle

Bodies	Degrees of Freedom	Types of Motion
L Wheel	4	translation along z-axis, rotation around x-axis, rotation around z-axis and rotation around y-axis
Upright	3	translation along z-axis, rotation around x-axis and rotation around z-axis
Upper, Lower and Pivot-plate	2	translation along z-axis, rotation around x-axis
Back-plate	1	translation along z-axis
Drum	1	rotation around y-axis

3.2.1 Drum Test Rig Simulations

The design and setup of the drum test rig was discussed in 3.2. The simulation process will allow the testing of the Pirelli tyre at various conditions. The test conditions are listed in Table 3.2. The drum rotational speed is kept constant throughout the testing. The vertical applied load was chosen to get a clearer idea of the behaviour of the tyre under different loads. The slip angle and camber angle ranges are chosen such that the effects of camber and slip angle are clearly visible in the simulation results.

Table 3.2: Simulation Conditions

Test Parameter	**Value**
Drum Rotational Speed	10 $[rad/s]$
Drum Diameter	1.6 $[m]$
Drum Road Longitudinal Speed	3.71 $[m/s]$
Camber Angle (γ)	0° to −8°; in −1° increments
Slip Angle (α)	0° to 15°; in 1° increments
Vertical Applied Load (F_z)	3500N and 6850N

A graphical topology of the Adams and MATLAB/Simulink co-simulation is illustrated in Figure 3.2.

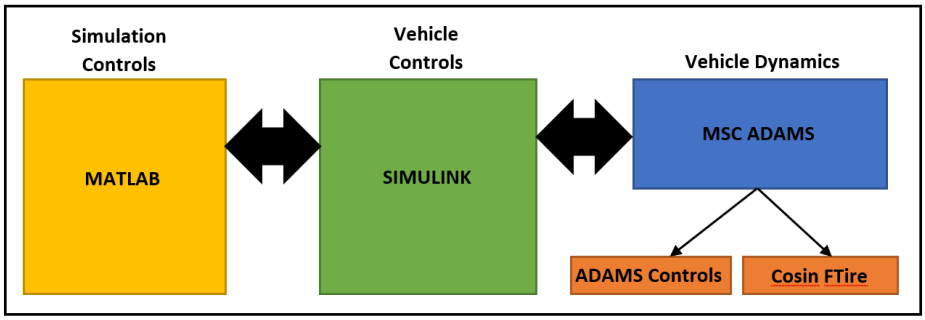

Figure 3.2: Adams and MATLAB/Simulink co-simulation

The co-simulation is conducted in three main components with feedback between all three the main components of the co-simulation. The first component is MATLAB. MATLAB is used to setup the desired simulation variables and to initialize and start the simulation process. MATLAB is also used to load the necessary variables into the workspace. The Simulink simulation controls are initialized from the MATLAB script. Simulink is used to provide the necessary controls for the simulation model. Simulink is also used to initialize and control the MSC Adams multibody dynamics simulation. Adams uses Cosin FTire as the 3rd party software to simulate the response of the tyre.

3.2.2 Drum Simulation Results

Finally, the drum simulation conditions in Table 3.2 was used to conduct multiple simulations with the drum test rig. The nature of the FTire drum road is such that it requires two inputs that define the rotational speed of the drum road. For the purposes of the simulations, the speed is kept unchanged for all the drum simulations that was completed. The speed profile of the drum, and resultantly, the wheel is graphically depicted in Figure 3.3. This speed profile is shown for $\gamma = 0$ ° and $\alpha = 0$ °.

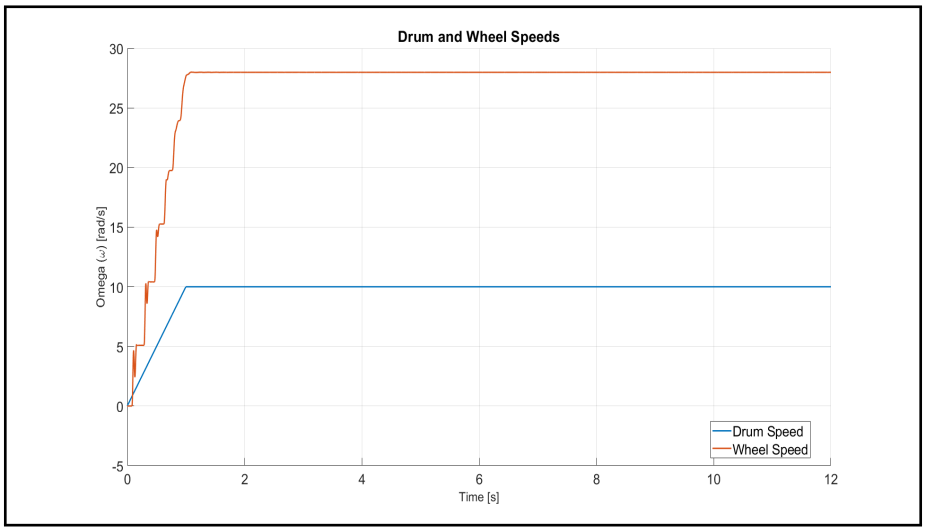

Figure 3.3: Speed profile of drum road and wheel

The simulation was conducted with a left sided wheel turning left (left hand corner) with negative camber imposed on the wheel. Figure 3.4 illustrates the wheel cornering simulation conditions.

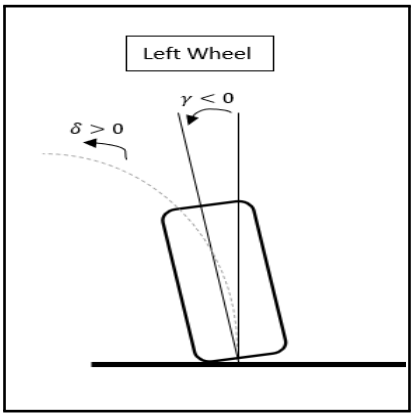

Figure 3.4: Wheel simulation cornering conditions (Front View of a Single Tyre)

With the simulation setup completed, all the simulations in Table 3.2 are completed. The two vertical load cases in Table 3.2 will be investigated in more detail. Vertical load case one is $3500N$ and vertical load case two is $6850N$.

Vertical Load Case 1

The first set of simulation results to be investigated is the case of the vertical applied load of $3500N$. This load case is chosen to simulate a low-speed cornering manoeuvre with a small weight transfer onto the wheel. This will help in understanding the behaviour of the tyre at low speed and small load transfer conditions. The graph in Figure 3.5 illustrates the lateral force developed on the wheel for three distinct camber angles. The three camber angle conditions that will be considered are chosen to be $\gamma = [0°, -3°, -6°]$. These values are chosen such that a clear distinction between the different cases can be made. Figure 3.5 demonstrates that as camber is changed to be more negative (increased camber), the higher the lateral force being generated by the tyre will be, as expected.

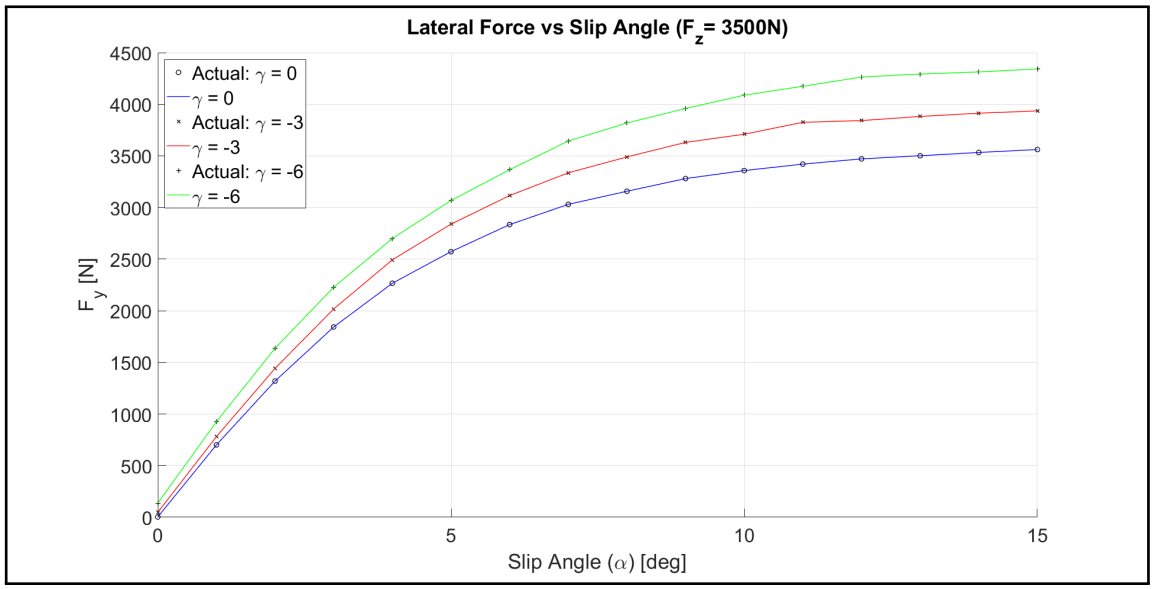

Figure 3.5: Lateral Force versus slip angle for $F_z = 3500N$

As discussed in section 2.5, the cosin FTire software generates an output file with the power loss in the contact patch. A fraction of the power loss in the contact patch is made up of the friction in the tread elements and the remainder is the power lost in the tread elements due to material damping. For this study, the focus was on the friction power between the tyre and the road. From the simulation results a picture is formed with the power loss due to friction. Figure 3.6 demonstrates the friction power loss FTire output for varying slip angle α and three camber angle γ conditions. From Figure 3.6, the friction power loss in the tyre increases as the slip angle is increased. More so, the friction power loss is increased due to the increases in camber angle.

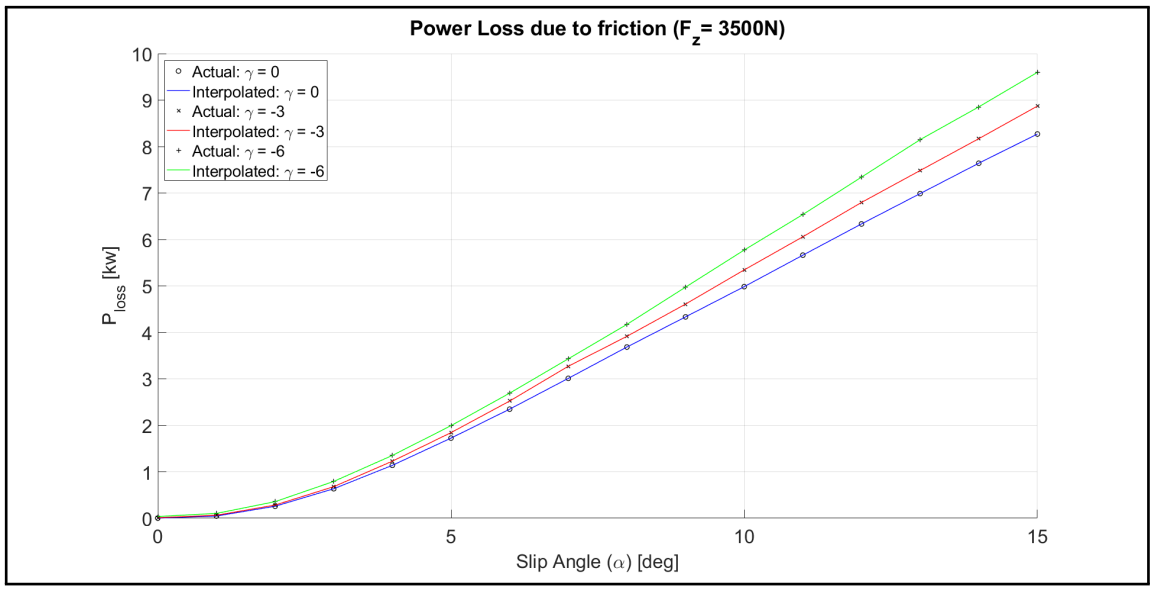

Figure 3.6: Friction power loss versus slip angle for $F_z = 3500N$

The idea of the drum simulations is to determine if the power loss in the tyres can be reduced during cornering conditions. Therefore, it is of the utmost importance to know that for the vehicle to negotiate a turn at a desired lateral acceleration, the tyres should develop a lateral force that keeps the vehicle on the desired path. Figure 3.7 represents

the same data as in Figure 3.6, but by adding the lateral force on the x-axis, the data can be displayed in a more relevant fashion.

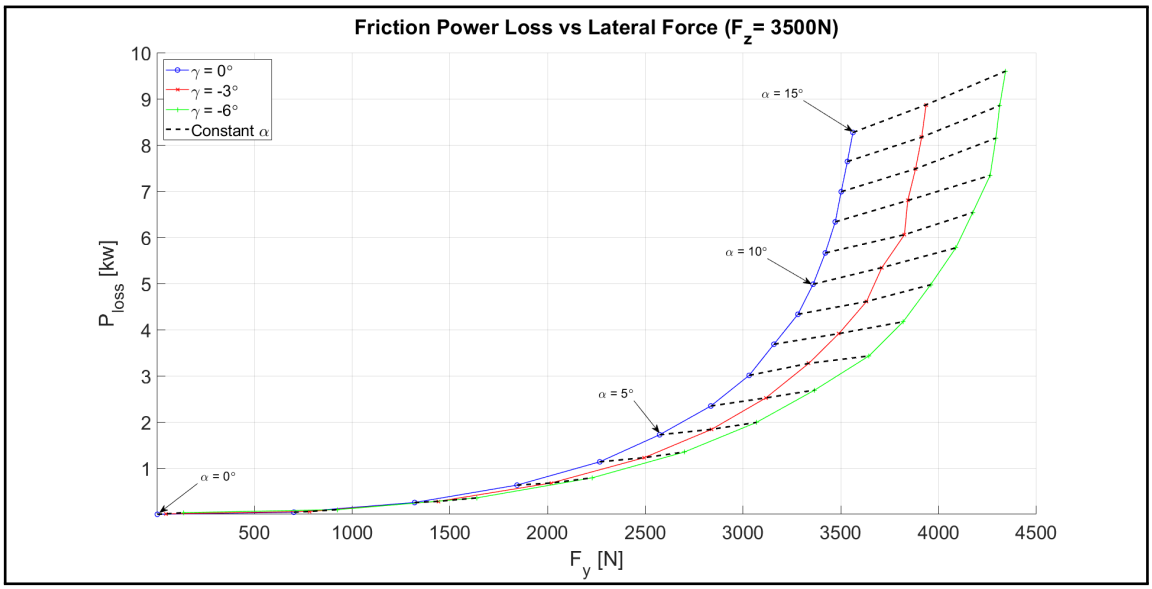

Figure 3.7: Friction power loss versus lateral force for $F_z = 3500N$

From Figure 3.7, the friction power loss versus the lateral force can be investigated. Upon closer investigation of Figure 3.7, it can be seen that for each lateral force, there is a number of different combinations of slip angles and camber angles that are capable of delivering a desired lateral force. The black dashed lines in Figures 3.7 and 3.8 represent the constant slip angle values (between 0° and 15°). By normalising the lateral force in the graph represented in Figure 3.7, a different representation of the data is achieved. The normalisation of the lateral force yields the Lateral Force Coefficient (LFC) (F_y/F_z) of the tyre road interaction. The LFC is analogous to the friction coefficient. Figure 3.8 illustrates the Friction Power loss versus the LFC.

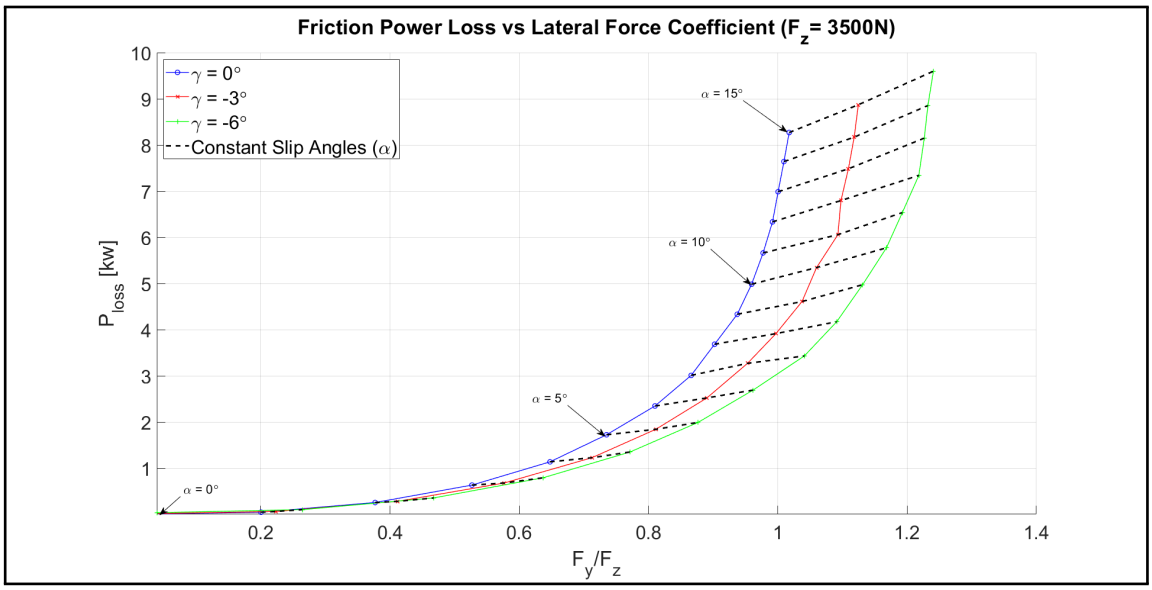

Figure 3.8: Friction power loss versus LFC for $F_z = 3500N$

Figure 3.8 demonstrates that as the camber angle is increased (more negative), the LFC value is increased. The graph of the friction power loss versus the LFC, represented by

Figure 3.8, shows that with the increase in camber angle, an increase in the LFC is observed. As with Figure 3.7, it is evident in Figure 3.8 that there are multiple combinations of slip angle and camber angle that will result in the same LFC, but at a reduced friction power loss.

The case represented in this chapter is the case of a single tyre. The simulation results demonstrate good potential for reducing power losses, but if the investigation is extended to a full vehicle investigation, the effects of the inner wheel and the outer wheel will counteract one another to some extent. This is due to all wheels having a negative camber angle. The key is that the friction power being saved by the outside wheels are greater than the friction power increase on the inside wheels.

Considering $3500N$ of lateral force for example, there is a great possibility of reducing the friction power loss in the tyre. Figure 3.9 illustrates the combinations of slip angles and camber angles that are possible to deliver the required $3500N$ lateral force and the corresponding friction power in the tyre. Figure 3.9 is valuable in demonstrating that for a constant lateral force of $3500N$, as the camber angle is increased, the corresponding slip angle can be reduced in order to maintain the same lateral force of $3500N$ being developed by the tyre. Therefore, Figure 3.9 demonstrates that as the camber is increased, the slip angle is decreased and the friction power developed in the tyre is also reduced.

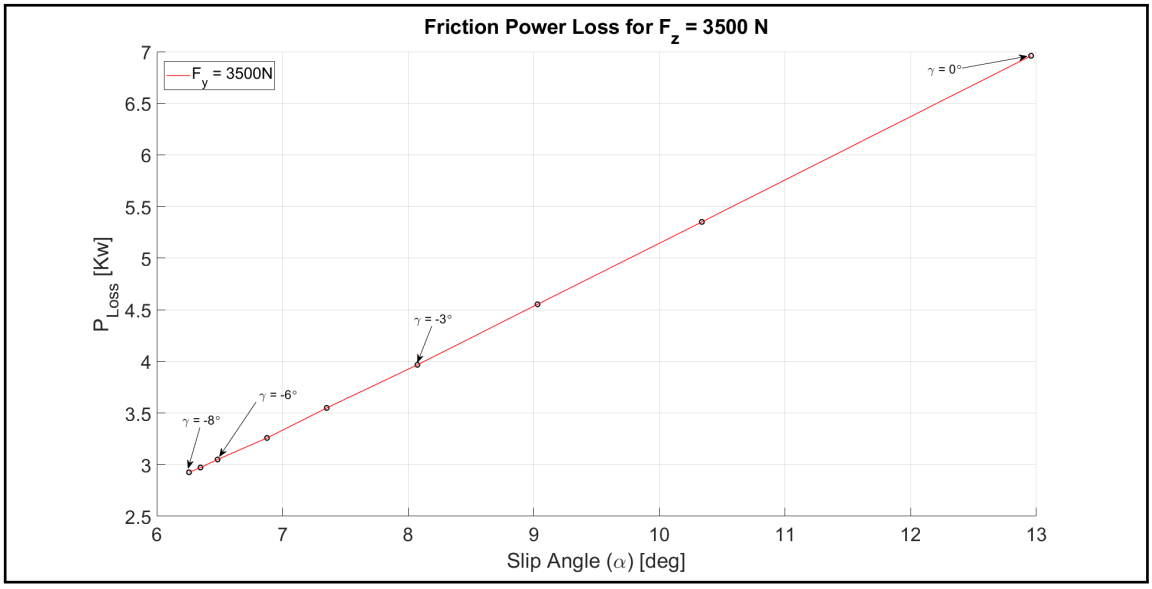

Figure 3.9: Friction power loss reduction for $F_y = 3500N$

The overall friction power loss for $F_y = 3500N$ is reduced as shown in Table 3.3. From Figure 3.9 a maximum saving of 57.96% is observed at $\gamma = -8°$. These saving values represented in Table 3.3 are only for a single lateral force on a single tyre. This was done to demonstrate the capabilities of camber control and the advantages thereof.

Table 3.3: Friction power loss reduction at $F_y = 3500N$ for vertical load of $F_z = 3500N$

Slip Angle (α) [°]	**Camber Angle** (γ) [°]	P_{frict} $[kW]$	**% Saving**
12.96	0	6.960	0
8.074	-3	3.967	43
6.484	-6	3.050	56.18

Vertical Load Case 2

The second load case to be considered is for a vertical load of $6850N$. This load case is chosen to simulate the wheel around a constant radius turn at higher speeds resulting in a greater load transfer on the wheel. Thus, creating a clear picture of the behaviour of the tyre at higher loads. The same three camber angle conditions will be compared as in vertical load case 1.

Figure 3.10 illustrates the lateral forces for vertical load case 2 and for the three camber angles being considered. The same trend as with vertical load case 1 is visible, wherein the increase in the camber angle results in a higher lateral force being generated by the tyre.

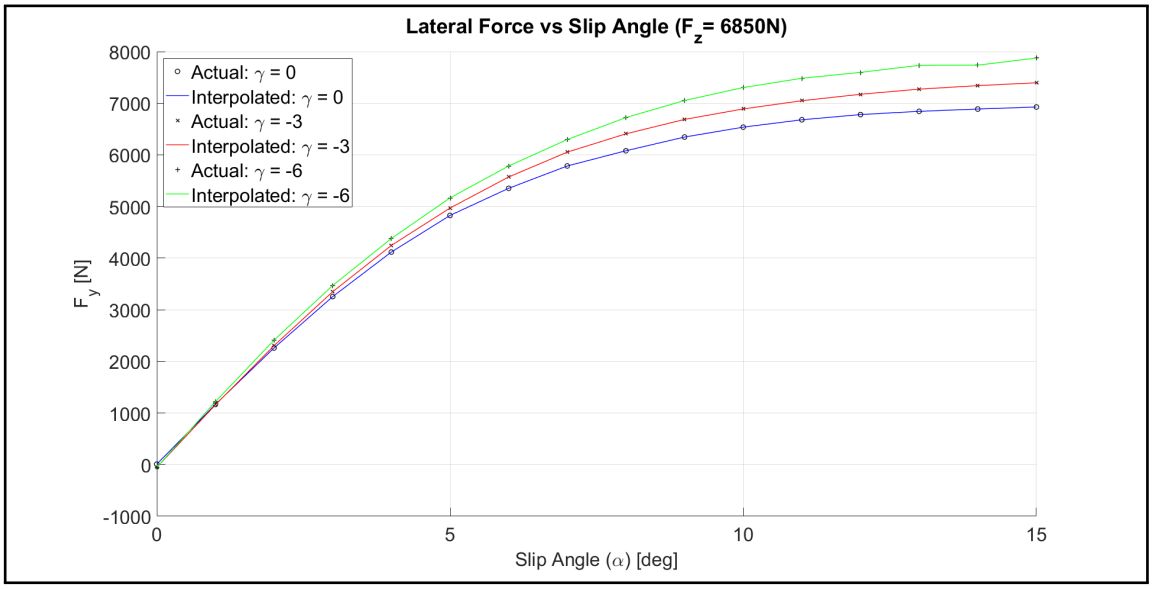

Figure 3.10: Lateral force versus slip angle for $F_z = 6850N$

The friction power loss against the slip angle is illustrated in Figure 3.11. As with vertical load case 1, the same trend appears for vertical load case 2. This trend demonstrates an increase in the friction power loss as the slip angle and the camber angle of the wheel is increased. At higher camber angles, the difference becomes even more clear, and the friction power losses increases. Similarly with vertical load case 1, however, the graph in Figure 3.11 is represented in a different and more relevant way.

Figure 3.12 shows the friction power loss versus lateral force for vertical load case 2. The trend of the graphs in Figure 3.12 can be directly compared to the trend of the graphs in Figure 3.7. However, the friction power lost is increased for vertical load case 2 compared to load case 1. This increased power loss is due to the increased vertical load on the tyre resulting in an increase in forces and moments produced by the tyre.

The data can be represented differently to produce Figure 3.12. Figure 3.12 demonstrates that for higher lateral forces, the possibility of reducing the friction power loss also increases. Considering a lateral force of $6800N$ for example. Figure 3.12 clearly shows that the friction power loss can be reduced at $6800N$ of lateral force, by increasing the camber angle and reducing the slip angle. The dashed black lines represent the constant slip angles.

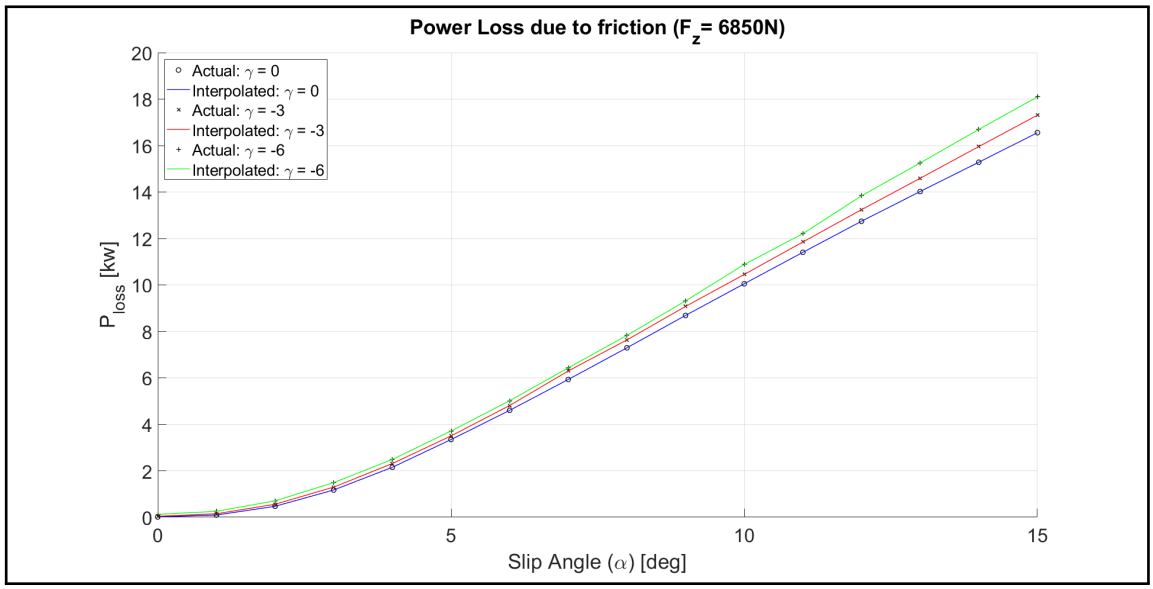

Figure 3.11: Friction power loss versus slip angle for $F_z = 6850N$

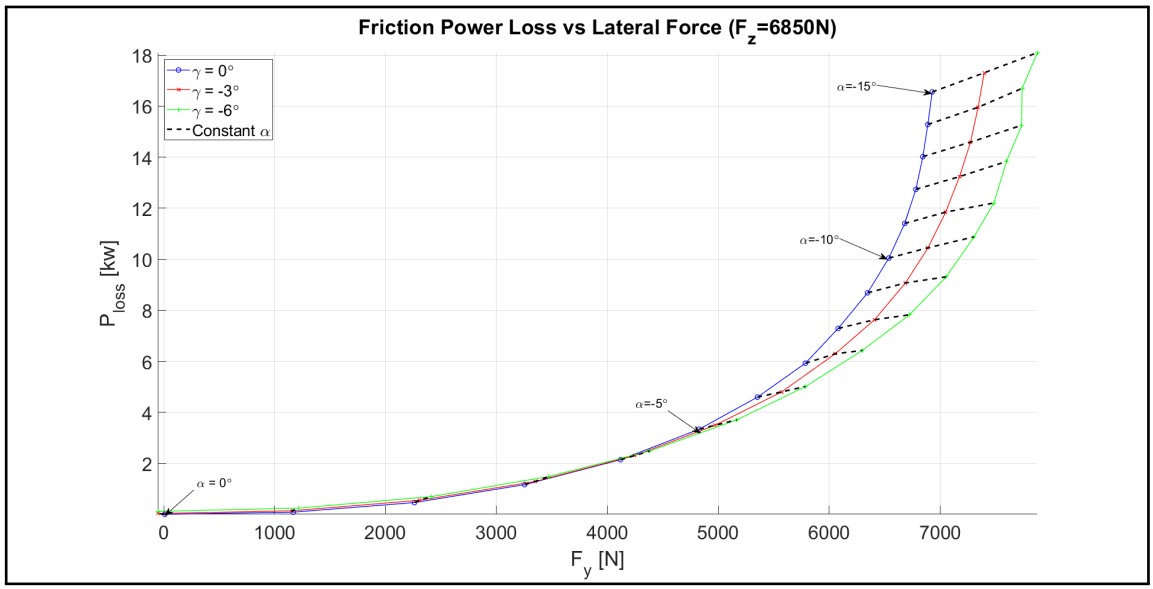

Figure 3.12: Friction power loss versus lateral force for $F_z = 6850N$

By normalising the lateral force, Figure 3.13 is produced. Figure 3.13 illustrates the graph of the friction power versus the Lateral Force Coefficient (LFC). With this graph, as the camber is increased (more negative), the higher the LFC becomes at larger slip angle values. The LFC values for vertical load case 2 are smaller than those for vertical load case 1. This is expected when the lateral force was normalised.

Figure 3.14 visually shows the reduction in friction power loss as the camber angle is increased and the slip angle decreased. It is important to note that Figure 3.14 only illustrates the results for a single case at $F_y = 6800N$. These values will vary depending on the lateral force and the normal force experienced on the tyre. Take Figure 3.13 and Figure 3.8 for example, the normal force acting on the tyre plays a great role in the development of the lateral force of the tyre, and consequently, the amount of friction power losses that can be reduced.

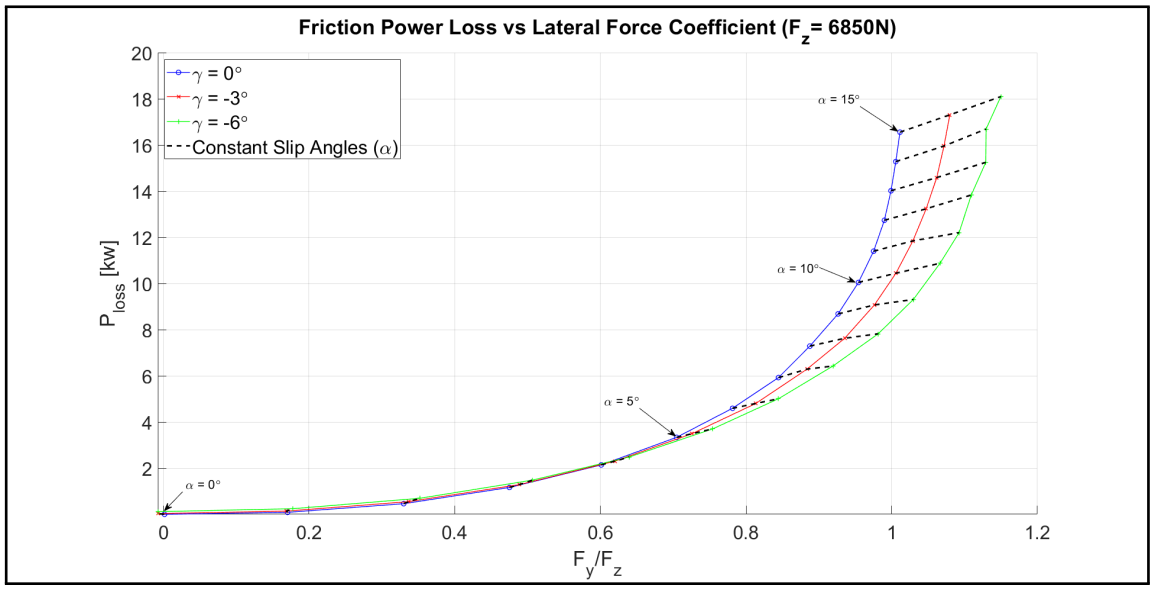

Figure 3.13: Friction power loss versus LFC for $F_z = 6850N$

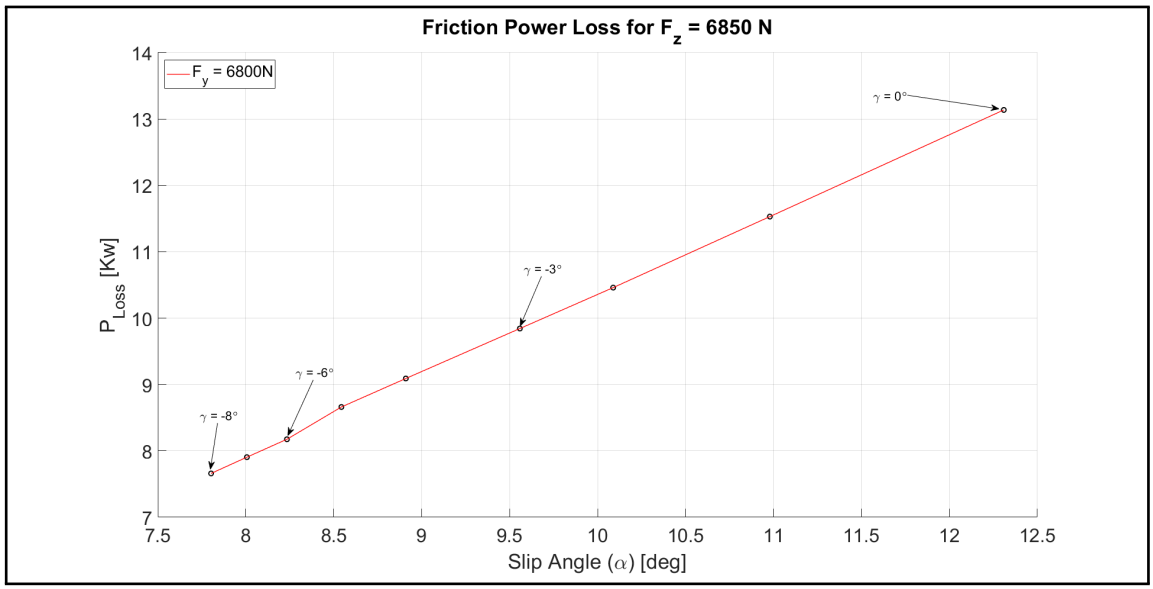

Figure 3.14: Friction power loss reduction for $F_y = 6800N$

The friction power loss reduction for $F_y = 6800N$ shows a maximum reduction of 41.69 % at $\gamma = -8°$. Table 3.4 demonstrates more friction power loss reduction statistics. The values represented in Table 3.4 are for a single lateral force on a single tyre only and was done to demonstrate the possibilities of using camber control to reduce friction power losses in tyres, especially at higher vertical forces.

Table 3.4: Friction power loss reduction at $F_y = 6800N$ for vertical load of $F_z = 6850N$

Slip Angle (α) [°]	**Camber Angle (γ) [°]**	P_{frict} $[kW]$	**% Saving**
12.31	0	13.14	0
9.558	-3	9.843	25.07
8.234	-6	8.175	37.77

3.3 Conclusion

From the simulation results, on a single tyre, the possibility to reduce the power loss with camber control is promising with good results. Between vertical load case 1 and load case 2, it was shown that as the lateral force demand increases, the power loss reduction possibilities increase. The possibility of reducing the power loss is clearer at higher slip angles, which simulates a more severe cornering manoeuvre. The same trends are clear throughout both vertical load cases. As expected, with the addition of camber angle, a higher lateral force can be produced by the tyre. This phenomenon is evident on the outside loaded wheel during cornering.

Also, with the addition of camber angle, the slip angle can be reduced resulting in a reduction of the power loss in the tyre. This would be extremely beneficial for electric vehicles because the power demand from the steering system can be reduced, resulting in a more efficient electric vehicle.

The result from this chapter is very promising and the study will therefore be extended to include a full vehicle study. This will be beneficial to replicate the results on a full non-linear vehicle model. It is expected that the results for a full vehicle might differ than the results represented in this chapter for a single tyre. This is expected due to the negative camber angle on all four wheels which will result in a counteracting phenomenon when negotiating a corner. The idea is that the power savings on the outside loaded wheel will be more beneficial than what will be experienced on the inside, unloaded wheel.

Chapter 4

Full Vehicle Model

Moving on from the tyre level simulations in section 3, the next step is to introduce the vehicle model which will be used for full vehicle simulations. The concept of camber control must be implemented on a full vehicle to assess its feasibility. This section will introduce the basic physics upon which a vehicle's dynamic behaviour is based. Thereafter, a full non-linear vehicle model, with a non-linear driver model is introduced and discussed in more detail. Once the familiarization of the vehicle model is complete, the cross-validation is completed. The cross-validation will be used to validate the full vehicle model with the addition of camber control, with existing test data. This will also ensure confidence within the simulation results due to the validity of the simulation models being used.

4.1 Vehicle Dynamics Introduction

The investigation into the road-holding capabilities or 'handling' of a vehicle is conducted to improve occupant safety, or to improve the road holding capabilities of the vehicle. The roadholding of a vehicle must be validated to prove that the vehicle can perform as expected during cornering manoeuvres. One method to prove the roadholding of a vehicle is by means of a constant radius test. The other, is by means of a Double Lane Change (DLC) manoeuvre.

For this study, the handling of the vehicle will be subdivided into two sections, namely, steady-state handling and dynamic handling. For steady-state handling, a simple constant radius (CR) test will be proposed. For dynamic handling, a severe double-lane-change (DLC) manoeuvre is proposed **(Cronjé and Els, 2010)**.

The CR test is conducted by driving around a circle of constant radius at increasing speed. The yaw rate, steer angle and lateral acceleration is measured, to determine the understeer gradient of the vehicle. Figure 4.1 graphically depicts the constant radius test.

The dynamic handling test is conducted with a DLC manoeuvre. The severe double lane change manoeuvre is defined as the dynamic manoeuvre in which a vehicle is driven from its initial lane, into another lane parallel to the original lane. The vehicle is then manoeuvred back into its initial lane without exceeding the track boundaries set out by **ISO3888 (2018)**. The **ISO3888 (2018)** documentation has defined a standard test for the severe double-lane-change manoeuvre that is used to measure the road-holding capabilities of a vehicle. The severe double-lane-change manoeuvre is often used for the

Figure 4.1: Nissan leaf Constant Radius Test **(Loveday, 2013)**

subjective evaluation of a vehicle's dynamics and transient road-holding abilities. The severe lane-change manoeuvre is used to assess a closed-loop system. The cone layout of the DLC manoeuvre is demonstrated in Figure 4.2.

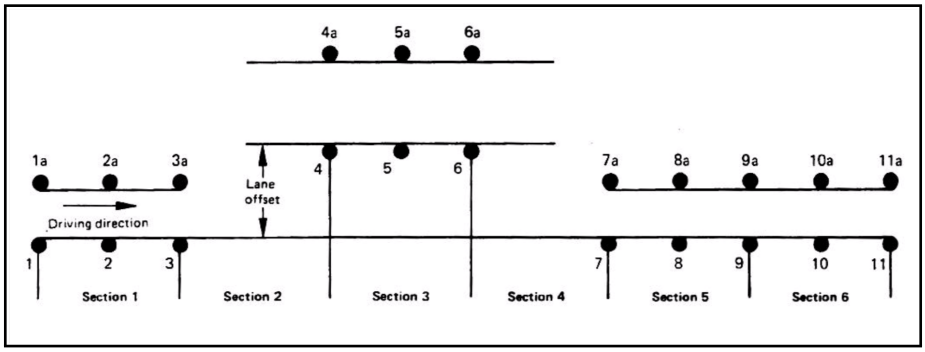

Figure 4.2: Cone placement for marking double-lane-change track **(ISO3888, 2018)**

4.2 Full Non-Linear Vehicle Model

The full vehicle model is developed and extensively validated by **Thoresson et al. (2009)**, **Uys et al. (2007)** and **Cronjé and Els (2010)**. The vehicle model is developed to be an accurate representation of the actual vehicle and is based on a Land Rover Defender 110 Tdi. MSC Adams was used to create the fully non-linear vehicle model. The model was originally developed with 16 degrees of freedom. The vehicle model utilizes the fully validated FTire tyre model. The vehicle body is modelled as two rigid bodies with a torsional spring connecting the bodies. The torsional spring helps to capture the torsional stiffness of the vehicle chassis. The $4S_4$ suspension system, developed by **Els et al. (2007)** is incorporated into the model with MATLAB/Simulinbk co-simulation. The vehicle's suspension is attached to a solid axle with vertically mounted suspension struts. The model also includes non-linear bump stops and bushings for greater validity, over the full range of suspension travel.

The vehicle model is equipped with a driver model that is used for path following with longitudinal demand (drive) forces. The driver and drive force models were developed by **Botha (2011)** and **Hamersma (2014)** respectively. The Adams vehicle model is illustrated in Figure 4.3.

The basic vehicle parameters are shown in Table 4.1. The vehicle model will be used as

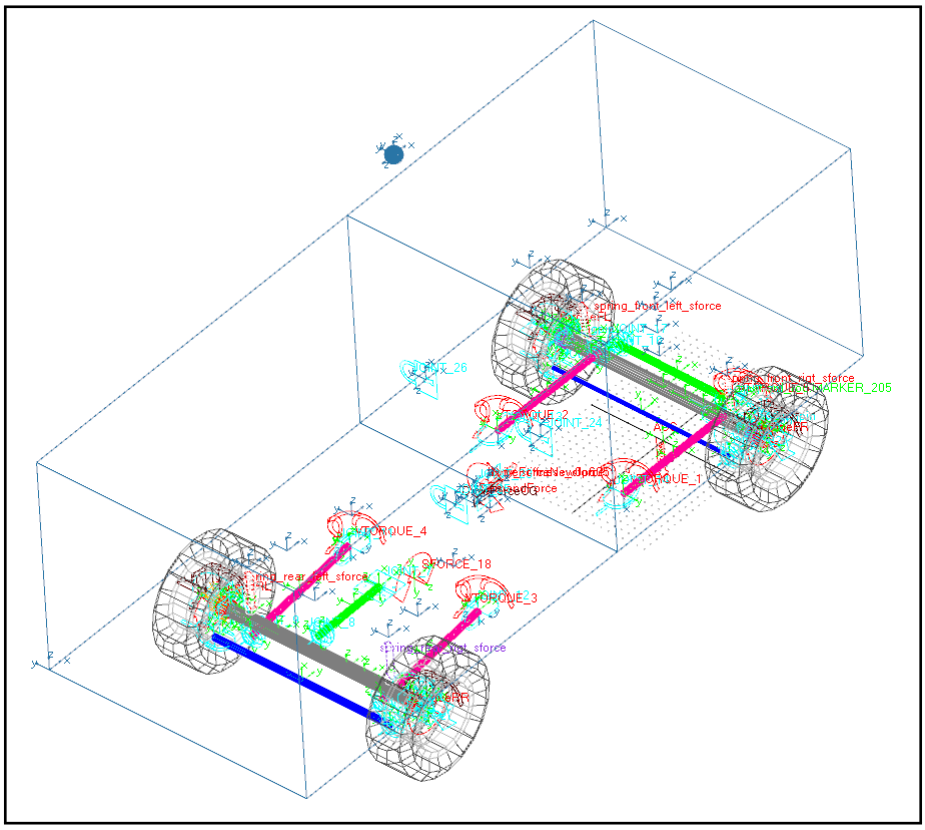

Figure 4.3: Wireframe view of full vehicle model

a baseline model for the development of the camber control model. The baseline model utilizes the full non-linear vehicle model with one single change. The baseline model incorporates the Michelin FTire tyre model instead of the Pacjeka tyre model.

Table 4.1: Simulation model vehicle parameters

Parameter	Value	Unit
Total Vehicle Mass	2047	kg
Sprung Mass	1582	kg
Longitudinal axis total mass moment of inertia	839	kgm^2
Lateral axis total mass moment of inertia	2471	kgm^2
Vertical axis total mass moment of inertia	2057	kgm^2
Distance from CG to front axle	1.55	m
Distance from CG to rear axle	1.25	m
Front and rear track width	1.49	m
Distance between front suspension struts	1.01	m
Distance between rear suspension struts	0.97	m
Total vehicle width	1.86	m

4.2.1 Full Vehicle Camber Model Layout

The schematic diagrams in Figure 4.4 and Figure 4.5 demonstrates the layout of the front and rear suspension respectively, for the camber model. The layout of the front suspension retains the geometry of the baseline model, however, with the added camber control DOF.

The camber is controlled with a small camber arm connected to the steering arm with a revolute joint. The steering arms are connected to the steering link and the front axle of the vehicle. The front axle is connected to the body with two leading arms and a Panhard rod.

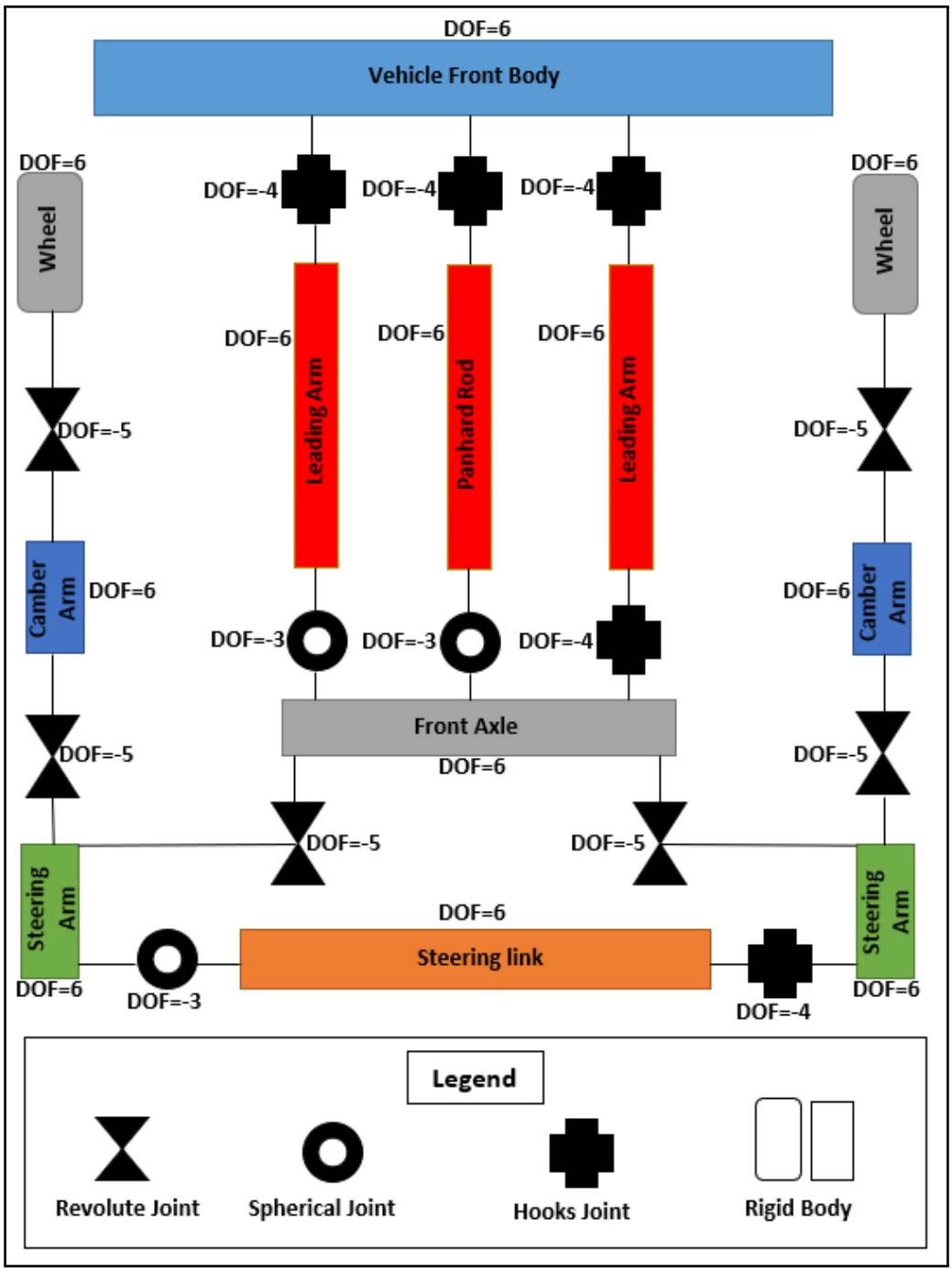

Figure 4.4: Front schematic diagram (With Camber DOF)

The layout of the rear suspension utilizes the same camber control methods as the front suspension. The front body is connected to the rear with a revolute joint. Control of the camber is thanks to the camber arms at the rear which are connected to the steering arms. The steering arms are connected to the rear steering link and the rear axle. The rear axle is connected to the rear body with two trailing arms and an a-arm.

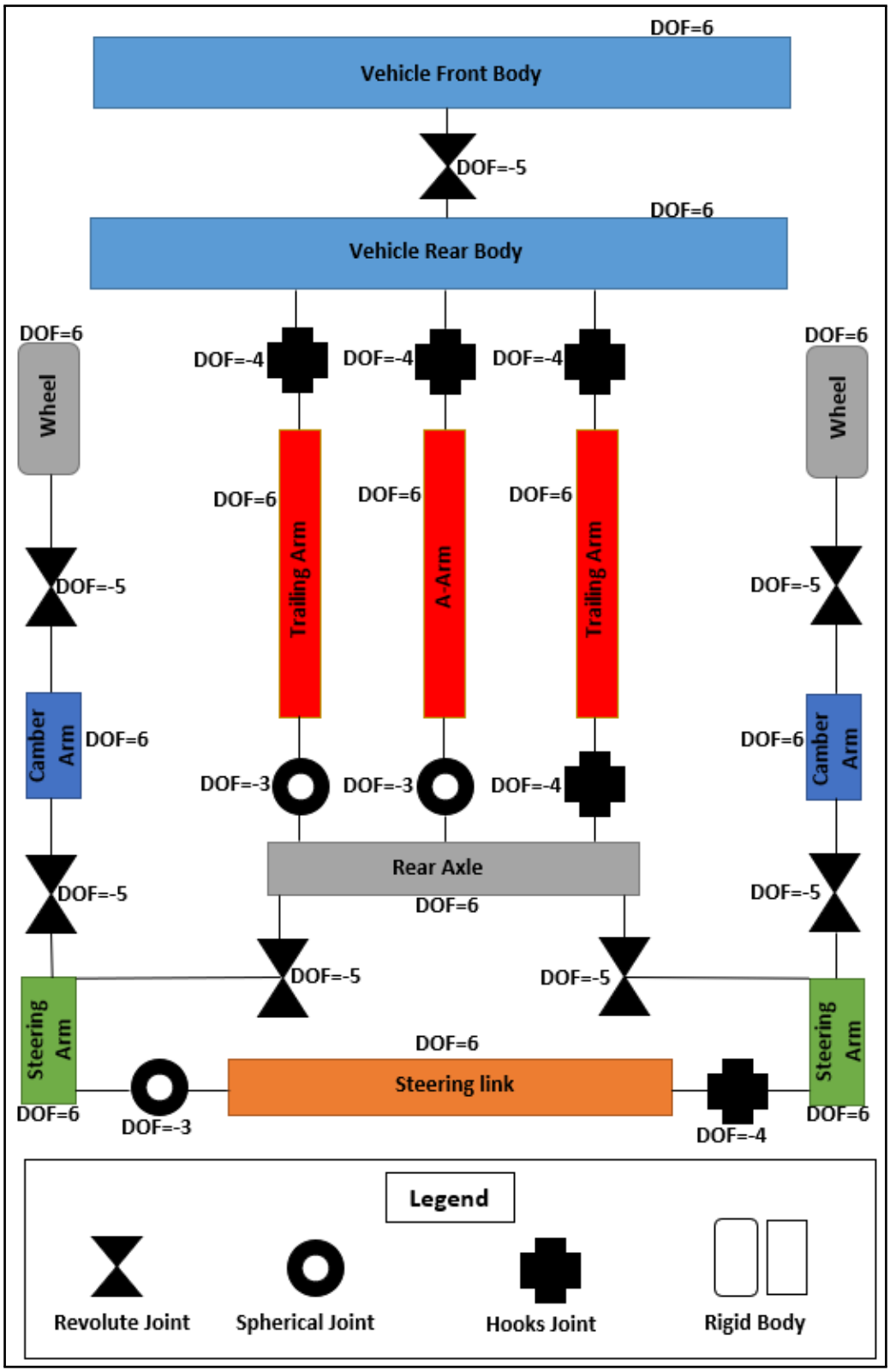

Figure 4.5: Rear schematic diagram (With Camber DOF)

The newly developed non-linear full vehicle model with the added camber DOF will be referred to as the camber model from this point onward.

4.3 Full vehicle validation

For the full vehicle model validation tests, the vehicle model in section 4.2, the baseline model, is used with a fully validated Michelin LTX AT2 FTire model, validated by **Bosch (2016)**. This model is the closest representation to the vehicle model used by **Peenze (2020)**. The validation is done by comparing the simulation model results to the experimental results gathered by **Peenze (2020)**. The better the correlation between the experimental data and the simulated data, the more confidence will be in the model to represent true vehicle dynamic behaviour.

The validation tests were conducted for a DLC manoeuvre at speeds of 50, 60 and 70 km/h. The Root Mean Square Error (RMSE) and the percentage of the data samples below the RMSE is illustrated in Table 4.2. The vehicle speed, yaw rate, lateral acceleration, roll angle and roll rate for both the soft and the hard suspension settings are graphically depicted in Figure 4.6 and 4.7 respectively. These results are shown for the vehicle travelling at 70 km/h.

Table 4.2: RMSE (% below) for DLC validation results

Vehicle Speed $[km/h]$	**Suspension Setting**	**Yaw Rate** $[deg/s]$	**Lateral Acceleration** $[m/s^2]$	**Roll angle** $[deg]$	**Roll Rate** $[deg/s]$	**Average % below RMSE**
50	Soft	2.959	0.6423	0.6124	1.500	-
		(76.01%)	(68.70%)	(67.01%)	(76.65%)	72.09%
	Hard	3.456	0.7211	0.4376	1.151	-
		(76.43%)	(72.78%)	(70.96%)	(73.48%)	73.41%
60	Soft	2.654	0.5788	0.9959	2.511	-
		(77.71%)	(77.19%)	(71.80%)	(73.88%)	75.15%
	Hard	3.715	0.8980	0.4976	1.636	-
		(77.85%)	(69.51%)	(70.11%)	(72.74%)	72.55%
70	Soft	2.308	0.6161	1.475	3.113	-
		(72.26%)	(61.83%)	(74.57%)	(78.88%)	71.885%
	Hard	2.393	0.7861	0.6418	1.535	-
		(70.20%)	(71.45%)	(67.66%)	(78.40%)	71.83%

The lower the RMSE value, the better the correlation between the experimental data and the simulated data will be. The higher the percentage of the absolute errors below the RMSE value, the better the correlation between the two data sets will be. The percentage of absolute error below the RMSE will be more than acceptable if it is greater than 70%. These are the metrices upon which the accuracy of the simulated model will be determined. Visually, the correlation between the experimental data and the simulated data is incredibly good for both the soft and the hard suspension settings.

The slight discrepancies between the two data sets can be attributed to various little issues such as the use of an imperfect driver model that varies slightly from an actual driver's inputs. Un-modelled friction within the suspension system that is due to years of service. The magnitude and time lag discrepancies could be contributed by the vehicle's speed not being held constant throughout the manoeuvre.

In general, considering the percentage of absolute errors below the RMSE value, most

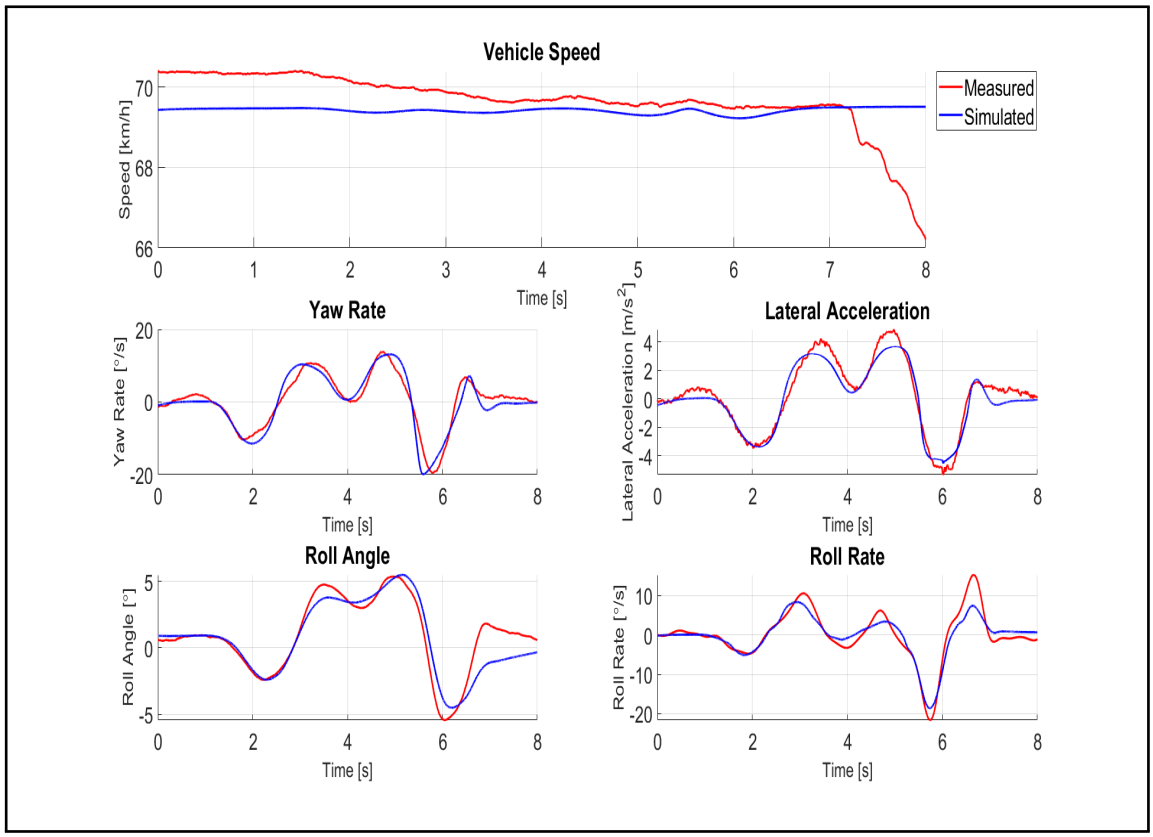

Figure 4.6: 70 km/h soft suspension setting validation

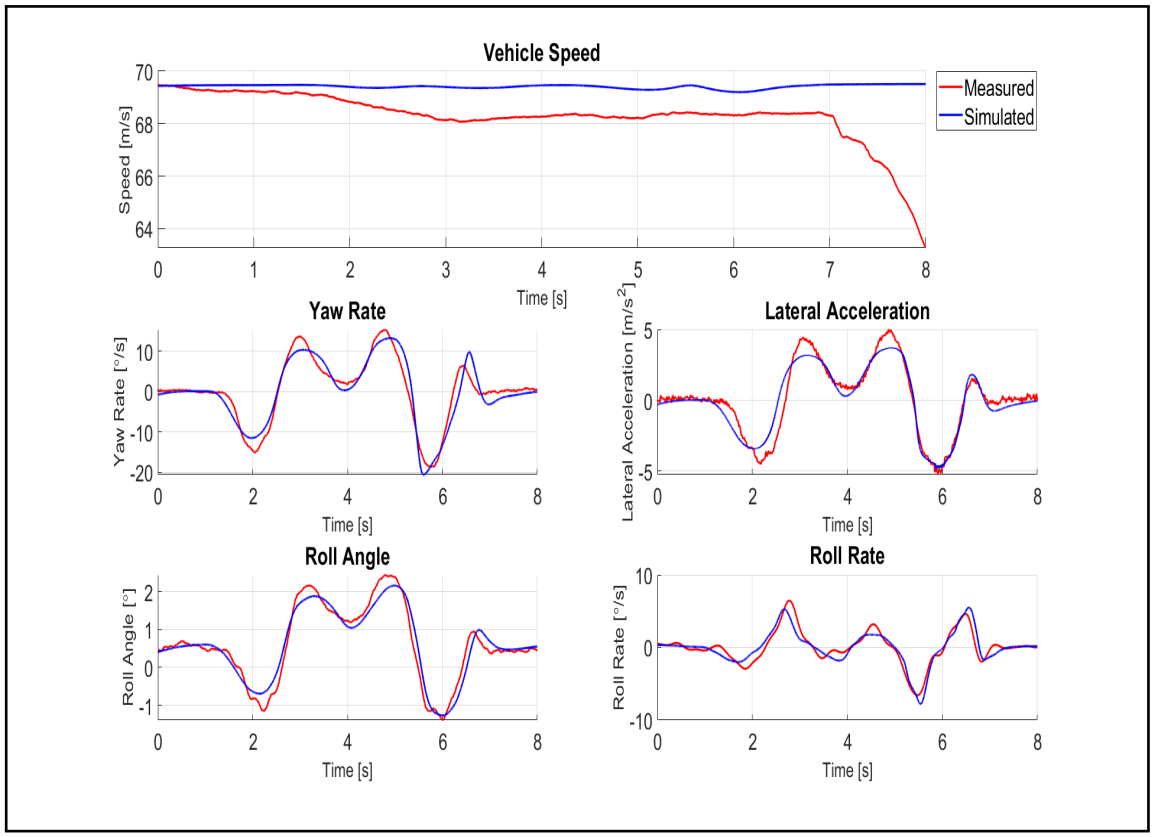

Figure 4.7: 70 km/h hard suspension setting validation

of the error between the simulated data and the experimental data is below the RMSE value. The average percentage below the RMSE values indicates that on average a good correlation between the data sets is visible (all average percentages are higher than 70%). Overall, the trends of the two data sets line up very well. Therefore, the simulation model used is fully validated and can be used as a method to represent the real-world behaviour of a vehicle during lateral dynamic manoeuvres.

4.4 Full Vehicle Cross Validation

In section 4.3 the validation of the highly non-linear full vehicle model was done. There it was proved that the results from the simulation model can be trusted and will accurately represent the behaviour of the real-world vehicle. The purpose of this section is to cross validate the vehicle model with camber control methods implemented to the validated vehicle model used in section 4.3. The newly developed vehicle model with camber control will utilize the Pirelli Scorpion tyre described in section 2.4.3. A modified full vehicle model based on the baseline model will be used for the comparison in this chapter with the baseline and the camber models. This modified vehicle model will be referred to the modified baseline model (baseline model with Pirelli FTire tyre model).

The process of cross validation has started in section 4.3, where the baseline model was cross validated with experimental data gathered by **Peenze (2020)**. The baseline model was originally validated by **Peenze (2020)**, but for this study, the validation was done to ensure the validity of the baseline model. The layout of the camber model was graphically depicted in Figure 4.4 and Figure 4.5 with schematic diagrams.

4.4.1 Cross Validation

This section will be used to conduct the cross validation of the camber model with the baseline model. The results from the cross validation will determine how accurate the camber model is to the baseline model and how trustworthy the data will be. It is particularly important to note that the tyre models are not the same for the camber and the baseline models. Thus, the modified baseline model will also be cross validated. Ideally, the modified baseline model should correlate exactly with the camber model because they used the same tyre models (the camber model includes the camber DOF where the modified baseline does not). By conducting this cross validation, a sanity check is performed where the changes that were made to the validated baseline model was checked to not affect the behaviour of the model in any way. This is done to ensure that there is confidence in the vehicle model and the tyre models being used.

The cross validation is conducted with a DLC manoeuvre at 50, 60 and 70 km/h. At this point, the driver controller is the driver model that was developed by **Botha (2011)**. The drive force controller is the one developed by **Hamersma (2014)**. The two models to be used for the cross validation have the same inputs, in terms of the steering, path and vehicle speed. The only difference between the baseline model and the camber model is the addition of a camber joint and the tyre on the model.

The cross validation for the soft suspension setting at 70 km/h is illustrated in Figure 4.8 and for the hard suspension setting in Figure 4.9. Visually, the correlation between the modified baseline model and the camber model is identical. Thus, indicating that

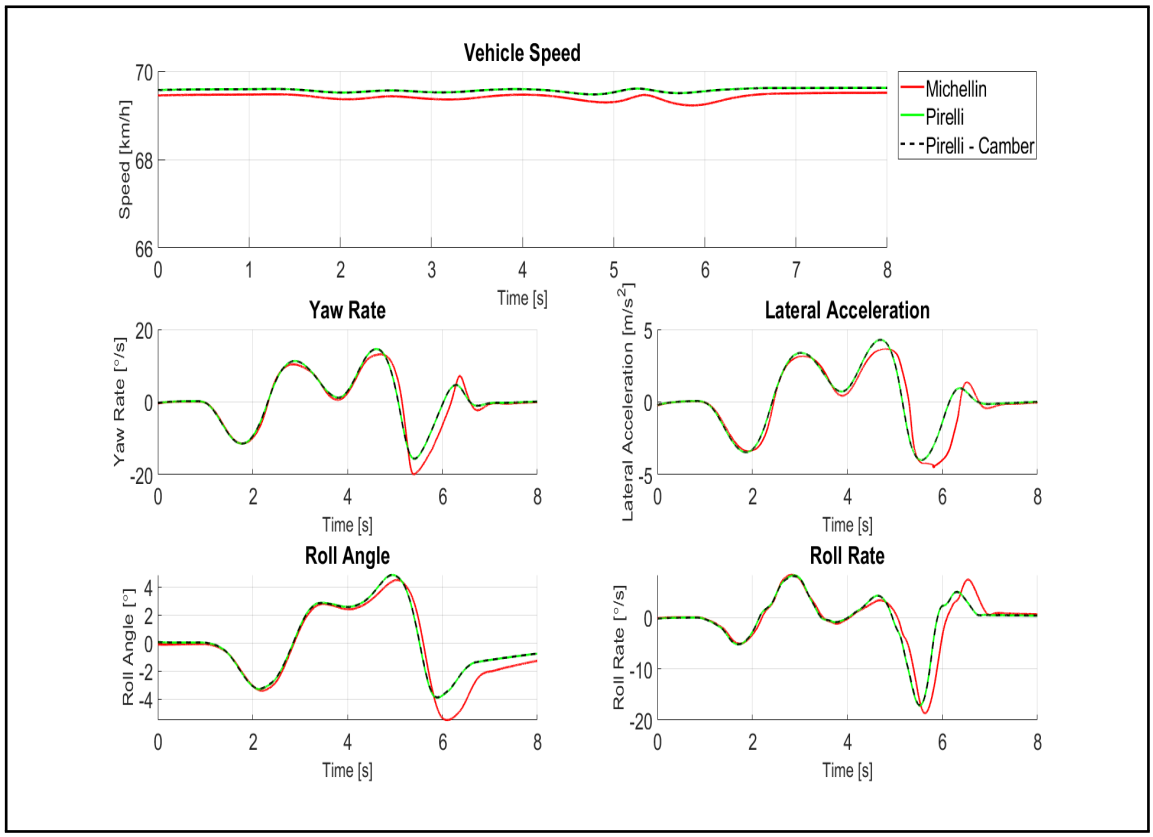

Figure 4.8: 70 km/h soft suspension setting cross validation

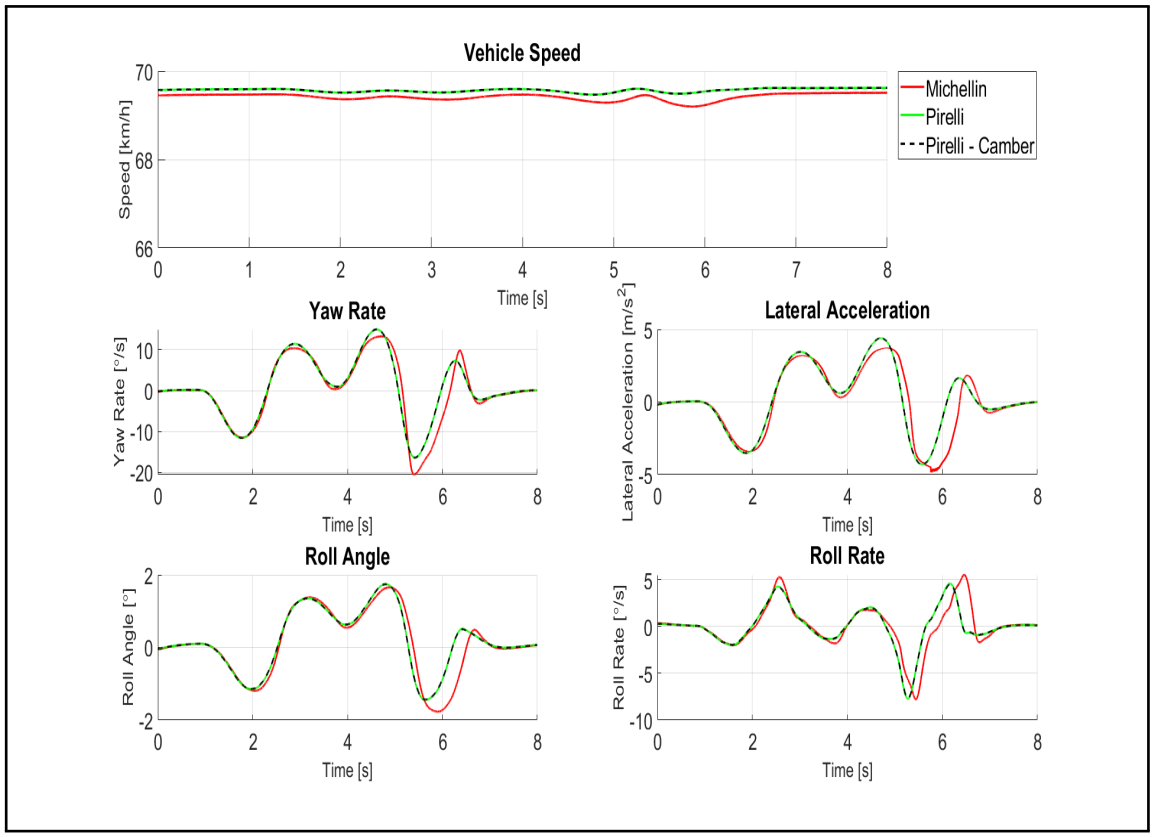

Figure 4.9: 70 km/h hard suspension setting cross validation

the addition of the camber DOF with the Pirelli tyre FTire model has no effect on the model's lateral dynamic behaviour. The discrepancy comes in between the baseline model and the camber model. This is expected because the tyre is a highly non-linear component and the difference between the Michelin and Pirelli tyres contribute the greatest to the discrepancies between the two models. However, despite the slight deviation between the two models, the trends of the data sets line up extremely well.

4.5 Conclusion

From the results, it was concluded that the lateral dynamics of the simulation model correlates very well with the experimental data gathered by **Peenze (2020)**. Therefore, fully validating the simulation model. However, due to the changes being made to the simulation model, a cross validation was conducted to validate the new camber model. From the results it was also found that the new simulation model, referred to as the camber model, is also validated and shows trustworthy data that correlates well with the baseline model. Therefore, it is concluded that the new camber model can be trusted to accurately represent the behaviour of the vehicle in real world conditions and will deliver trustworthy results. It is also important to note that the baseline model was validated at system level and the Michelin tyre has been validated at component level. By introducing a new tyre model, the Pirelli tyre model, which has been validated on component level, it is safe to assume that the multi-body dynamics full vehicle model with the Pirelli tyre remains valid at system level.

It was concluded that the discrepancies between the baseline model and the experimental data was partly contributed to by the lack of modelling of the friction in the suspension system due to years of service. The other cause of the discrepancies is due to the difficulty in controlling the gas charging procedure of the $4S4$ suspension system. Resultantly, if the mass of the gas inside the strut is incorrect, even by a small error, it can adversely affect the behaviour of the suspension system, especially on the hard setting. The vehicle's speed difference was also found to contribute to the lag in the two datasets and the use of the non-perfect driver model also contributed to the discrepancies between the datasets. It was concluded that the differences between the baseline model and the camber model is due to the non-linearities in the two different tyre models that was used.

From this chapter, it is concluded that a fully validated vehicle model, with provisions for camber control, has been developed and will be used for further simulations throughout the remainder of the study. The camber model will provide reliable and trustworthy results.

Chapter 5

Development of Camber Control Algorithm

In Chapter 5, the development of a simple camber control algorithm will be discussed in more detail. The aim of the development of a camber controller is to reduce the friction power developed by the tyres of a vehicle, without compromising the vehicle's dynamic behaviour. The camber control method will be implemented on the validated camber model described in chapter 4. From here on out, the simulations will be conducted with the validated camber model with the Pirelli tyre model.

5.1 Camber Controller

This section sets out to develop the camber control method that will be used to reduce the power loss in the tyres. From the introduction to the different camber control strategies in the previous section, it was concluded that there is only one relevant control strategy. This strategy is the one presented by **Sun et al. (2018)**. This is because the aim of this study is to investigate the possibility of using a camber control algorithm to reduce the power losses in the tyres of a vehicle. The work done by **Sun et al. (2018)** will therefore be a great guide for developing a control algorithm for changing the camber angle.

To determine the behaviour of the validated vehicle model at various camber angles, an array of simulation experiments was conducted to get a complete picture of the behaviour of the vehicle model with the Pirelli Scorpion FTire tyre model. The non-linearities in the tyre, vehicle suspension, driver controller and the combination of all these elements will influence the behaviour of the vehicle model. The simulation experiment layout is shown in Table 5.1. The simulation experiments are limited by the camber angle allowed on the vehicle. The camber angle will be limited to $\gamma = -6^{\circ}$.

The values in Table 5.1 are chosen such that there are no instabilities in the simulations due to the manoeuvres being too severe for the vehicle to handle. Things such as a sudden change of steering angle that results in the sudden spike in roll angle and resultantly, the inside wheels lifting from the ground. Cases where the sudden change in lateral acceleration influences the driver controller.

The path followed for the simulation experiments is a constant radius curve with a radius

Table 5.1: Simulation Experiments Input Parameters

$\mathbf{V_x}$[km/h]	R[m]	γ [°]
40	50	0, -0.5, -1.0, -1.5, -2.0, -4.0, -6.0
	100	
50	50	0, -0.5, -1.0, -1.5, -2.0, -4.0, -6.0
	100	
60	50	0, -0.5, -1.0, -1.5, -2.0, -4.0, -6.0
	100	
70	100	0, -0.5, -1.0, -1.5, -2.0, -4.0, -6.0
80	100	0, -0.5, -1.0, -1.5, -2.0, -4.0, -6.0

(R) as specified in Table 5.1. The speed of the vehicle is kept constant throughout the simulation. An example of the simulation results is illustrated in Figure 5.1. Figure 5.1 illustrates the path followed, lateral acceleration, total friction power of all four wheels and the change in the friction power between the simulation runs with a constant camber angle of $\gamma = -1°$ and $\gamma = 0°$ applied to all four wheels. Figure 5.2 illustrates the same as in Figure 5.1 but with a constant camber angle of $\gamma = -6°$ and $\gamma = 0°$ applied to all four wheels.

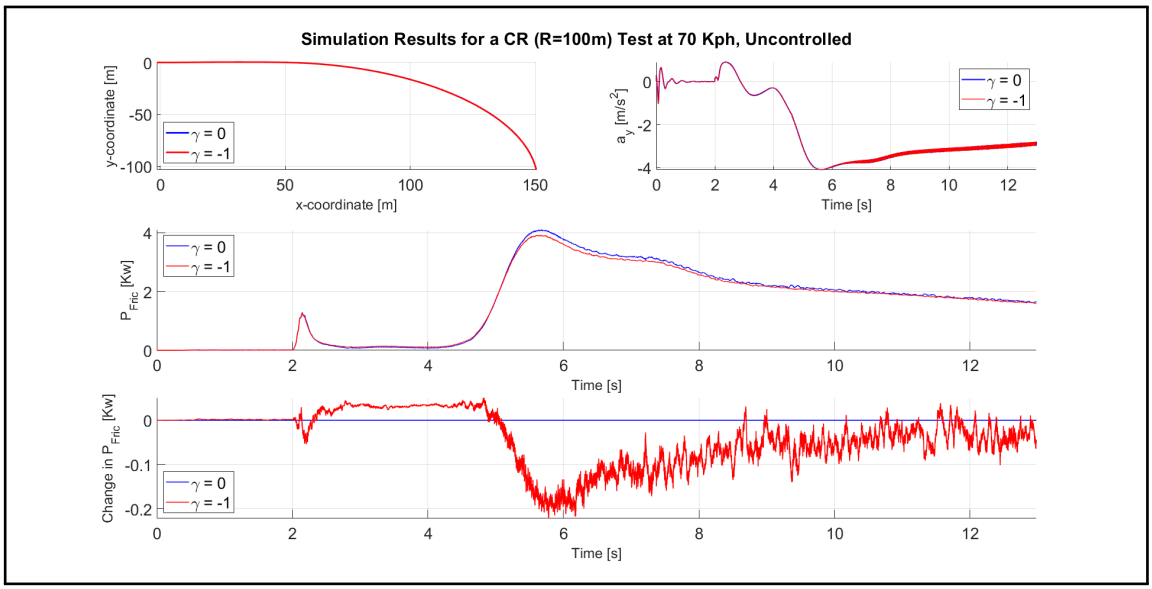

Figure 5.1: Simulation results for 70 Kph, R=100m and $\gamma = -1°$ (From top left clockwise: Vehicle path Followed, Lateral Acceleration, Total Friction Power on All Four Wheels & Total Change in Friction Power)

In both Figures 5.1 and 5.2, there is a slight decrease in the lateral acceleration as the simulation progresses. This could be attributed to the fact that a non-perfect driver model was used for the simulations, as was stated in Chapter 4.

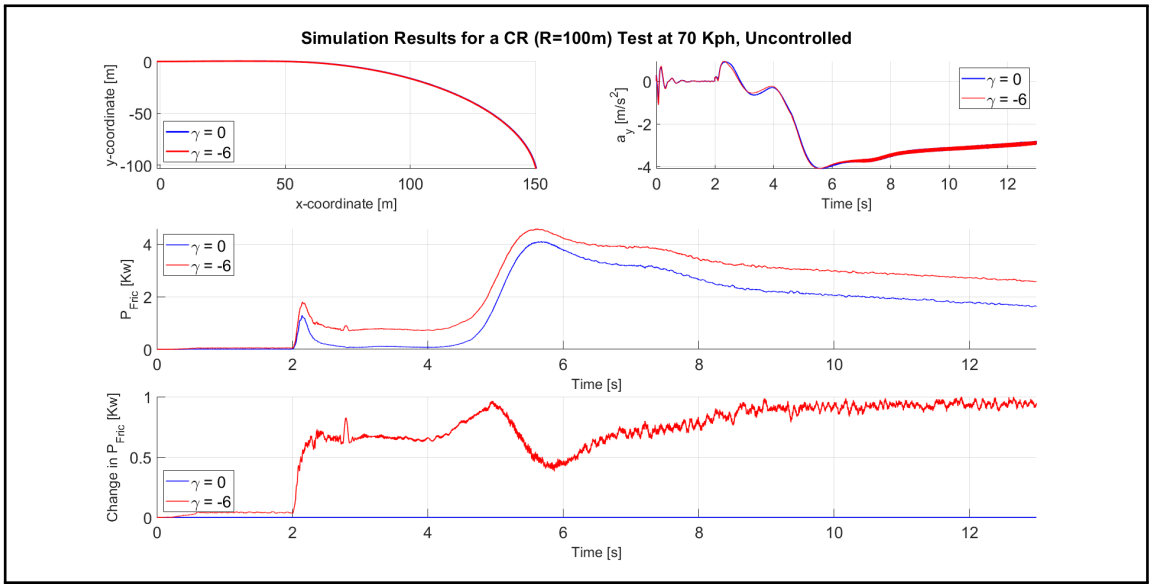

Figure 5.2: Simulation results for 70 Kph, R=100m and $\gamma = -6°$ (From top left clockwise: Vehicle path Followed, Lateral Acceleration, Total Friction Power on All Four Wheels & Total Change in Friction Power)

From the simulation results represented in Figures 5.1 and 5.2, it is evident that with the addition of a camber angle, there is a small difference between the lateral acceleration and the path followed, between the baseline and cambered tests (not visible in the graph in Figure 5.1 and 5.2). The average lateral offset between the baseline (no camber) and the cambered simulations is illustrated in Figure 5.3. The average lateral offset is calculated from the CG of the vehicle. The maximum average lateral offset observed is 0.3877m. This is 20.81% of the total width of the vehicle. Under normal driving conditions ($a_y < 5m/s^2$), the maximum average lateral offset is 0.289m or 15.5% of the width of the vehicle. The lateral offset is calculated with equation 5.1, where $cg_{,y1}$ is the lateral position of the CG for no camber (uncontrolled) simulation and $cg_{,y2}$ is the lateral position of the CG for a cambered (controlled) simulation.

$$\Delta y_{,off} = cg_{,y1} - cg_{,y2} \tag{5.1}$$

The average lateral offset depicted in Figure 5.3, therefore illustrates that with camber angle, the CG of the vehicle will be offset to effectively reduce the radius of the CR curve. Therefore, the steering angle input can be reduced which will reduce the lateral offset compared to the baseline simulation (no camber). The lateral offset means that effectively, the camber angle enables the steering angle input to be less, resulting in the steering system to overcome smaller tyre loads and resultantly reduce the power required to navigate a dynamic cornering manoeuvre. This lateral offset could be minimised by extending the driver controller developed by **Botha (2011)** to consider the addition of camber angle on the wheels and to adjust the steering angle input accordingly.

Figure 5.1 and 5.2 also illustrates the total friction power on all four wheels and the change in total friction power. It is important to note that there will be a give and take for the friction power, with the addition of camber on all four wheels. When negotiating the constant curve with cambered wheels, the outside wheels become loaded as the weight is transferred outwards and the camber angle is resultantly reduced. The inside wheels

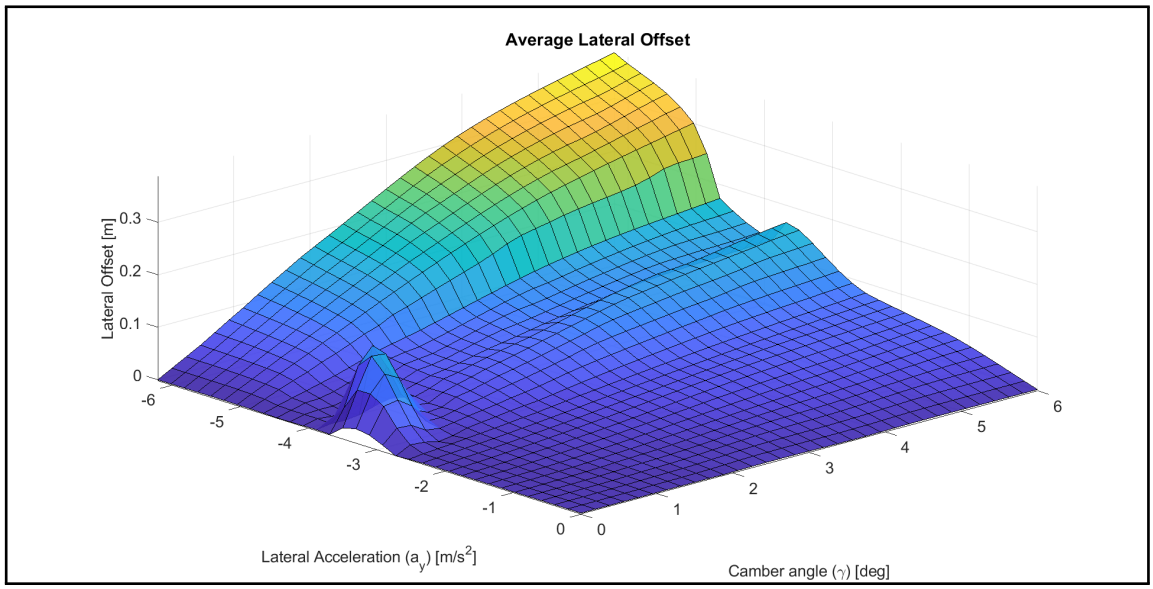

Figure 5.3: Average Lateral Offset between Baseline and Cambered Simulations

become unloaded, and the camber angle is increased. This is done by means of adding a camber DOF to the simulation model, as discussed in Chapter 4, and invoking independent camber angles on the left and the right side of the vehicle (remember that $\gamma_L = \gamma_R$). The idea is that the savings on the outside wheels outweigh the losses from the inside wheels, without compromising the lateral dynamics of the vehicle.

The total friction power is calculated with equation 5.2 and the energy reduced due to the friction power on all four tyres is represented by equation 5.3.

$$P_{Fric,all} = P_{Fric,FL} + P_{Fric,FR} + P_{Fric,RL} + P_{Fric,RR} \tag{5.2}$$

$$\Delta E_{Fric} = \int P_{Fric,all}(\gamma_L \neq 0, \gamma_R \neq 0)dt - \int P_{Fric,all}(\gamma_L = 0, \gamma_R = 0)dt \tag{5.3}$$

A reduction in the energy losses in the tyres is represented by a negative value for ΔE_{Fric}. Therefore, from Figure 5.1, the majority of the friction power in the tyres is either below zero, or equal to zero. In fact, the percentage of friction power below or equal to zero is 79.9%. The total energy saved for the 13 second simulated manoeuvre is 510.1484 J. Figure 5.2 on the other hand shows that by having too much camber angle can have a negative impact on the friction power saved. Not only does it cost power to change the camber angle, but the friction energy in the tyres is increased (worsened) by 41.8% or 8890 J, for the 13 second simulation time. Therefore, it is especially important to determine the correct camber angle for the correct lateral accelerations.

The metrics that will be used to quantify if the friction power can be reduced is the percentage power saved, represented by equation 2.27 and the total friction energy saved, represented by equation 5.4.

$$Total, E_{Fric} = -1 \times \Delta E_{Fric} \tag{5.4}$$

$$Total, E_{Fric} = \int P_{Fric,all}(\gamma_L = 0, \gamma_R = 0)dt - \int P_{Fric,all}(\gamma_L \neq 0, \gamma_R \neq 0)dt \tag{5.5}$$

In both equations 2.27 and 5.5, $\int P_{Fric,all}(\gamma_L \neq 0, \gamma_R \neq 0)dt$ represents the results from a non-zero camber angle simulation. The results from the simulations, with parameters described in Table 5.1, will be discussed in more detail.

The first metric that will be discussed is the percentage of friction power saved. The percentage of friction power saved is calculated with a modified version of equation 2.27. The adjusted equation is illustrated by equation 5.6 and equation 5.7.

$$\eta = \frac{Total, E_{Fric}}{\int P_{Fric,all}(\gamma_L = 0, \gamma_R = 0)dt} \times 100\% \tag{5.6}$$

$$\eta = \frac{\int P_{Fric,all}(\gamma_L = 0, \gamma_R = 0)dt - \int P_{Fric,all}(\gamma_L \neq 0, \gamma_R \neq 0)dt}{\int P_{Fric,all}(\gamma_L = 0, \gamma_R = 0)dt} \times 100\% \tag{5.7}$$

The results from the percentage of friction power saved is graphically depicted in Figure 5.4. The results indicate that by inducing too much camber at lower speeds can yield a negative outcome. From the results depicted in Figure 5.4, the percentage of friction power saved is hard to visualize due to the vertical range of the graph. For this study, the interest only lies within the range of positive vertical values (power saving range). Thus, a more focused view of Figure 5.4 is depicted in 5.5.

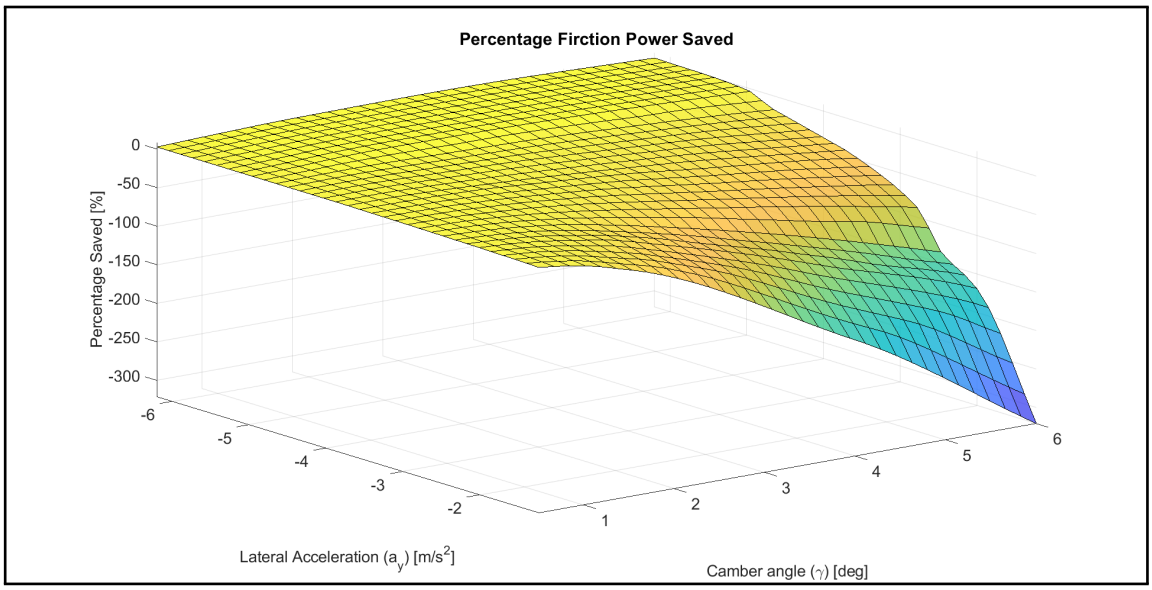

Figure 5.4: Percentage Friction Power Saved

By adjusting the vertical axis limits to show the results of interest, the graph in Figure 5.5 is created. The results indicate that as the lateral acceleration of the vehicle is increased, the allowable camber angle increases. In other words, at a lateral acceleration of $6m/s^2$, friction power can be saved at camber angles of up to 6 degrees, although it is not necessarily the highest friction power saving. The results also indicate that across the lateral acceleration ranges, the highest saving values are observed in the mid-range camber values ($\gamma = -2°$ to $\gamma = -4°$) for the Pirelli Scorpion tyre. The percentage of friction power saved

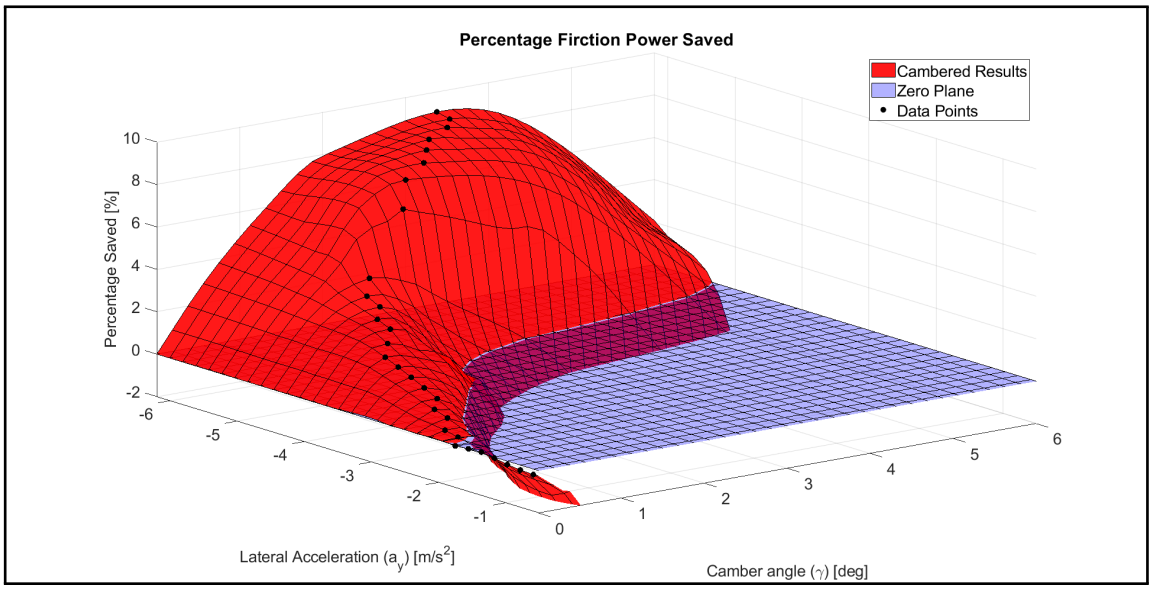

Figure 5.5: Percentage Friction Power Saved (Focused)

is a good metric to consider because over the lifetime of the vehicle, the savings will add up.

A set of simulation experiments where conducted based on the parameters that was described in Table 5.1. From each simulation, when the vehicle has settled in the corner, the lateral acceleration and camber angle was noted along with the friction power output from the FTire software. The total friction energy saved and the percentage of friction power reduced was calculated and are represented in Figures 5.6 and 5.5 respectively. By using a simple line search method on the results depicted in Figure 5.5, the camber angle and corresponding lateral acceleration values which resulted in the highest percentages of friction power saved (black data points in Figure 5.5), where extracted. Therefore, a relationship between the camber angle and the lateral acceleration was found for each camber angle of interest, in this study. These values would become the inputs for the camber controller.

Next metric to consider would be to quantify the amount of energy that could be saved. To compute the total energy saved, equation 5.5 is used. The results from the calculation of the total energy saved is graphically depicted in Figure 5.6.

From the top view of Figure 5.6, represented in Figure 5.7, it can be seen that similarly with Figure 5.5, the higher the lateral acceleration, the larger the camber angle can be and still result in a reduction in the total friction energy. Similarly as in Figure 5.5, the total friction energy change results in higher values at mid-range camber values. It is also concluded that a large change in the camber angle, will not necessarily result in the greatest overall friction energy saving.

From the results presented in this chapter, it is concluded that the greater the lateral acceleration is, the greater the camber angle can be, but there is a limit to the amount of allowable camber angle that will result in a high percentage of friction power saved.

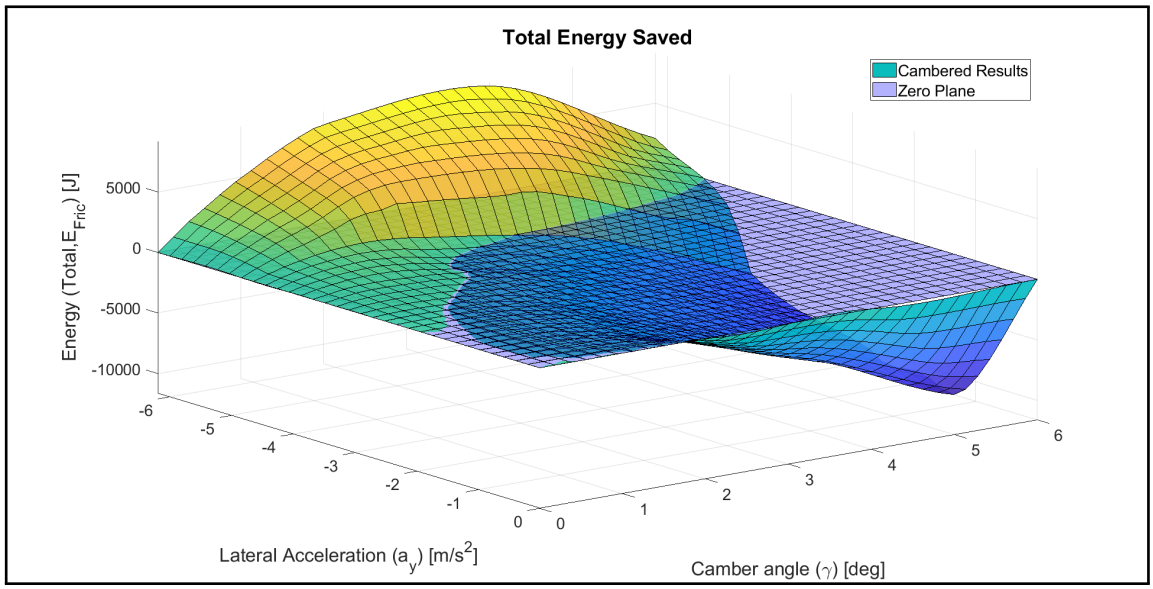

Figure 5.6: Total Energy Saved

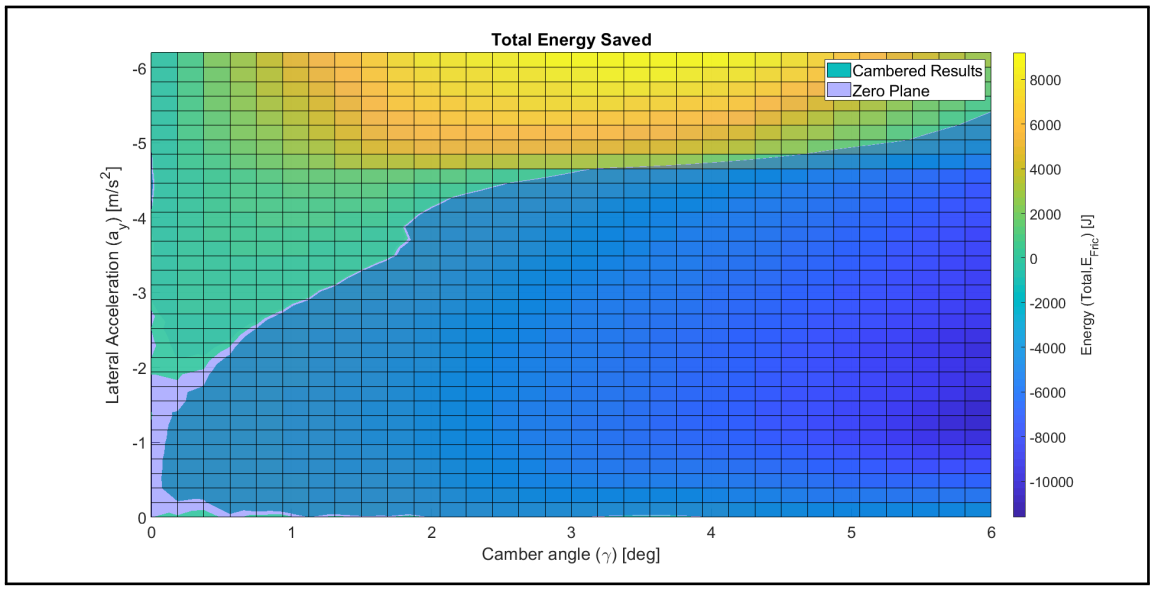

Figure 5.7: Total Energy Saved (Top View)

The lateral acceleration versus camber angle data that represented the highest percentage saved (black dots in Figure 5.5) was gathered and a line that best describes the relationship between the lateral acceleration and the camber angle was found (red line in Figure 5.8). The line depicted in Figure 5.8 represents the input for the simple camber control algorithm.

A linear line was fit through the non-zero camber angle data to best represent all the data points, but still have a linear relationship between the lateral acceleration and camber angle. The goodness of fit parameters is illustrated in Table 5.2.

The goodness of fit parameters indicates how well the line of fit describes the data points. The higher R-square and adjusted R-square values indicate a good fit. Overall, the line of fit is a good representation of the data points. The linearization of the data points with a line of best fit is done to reduce any instabilities in the camber controller. The

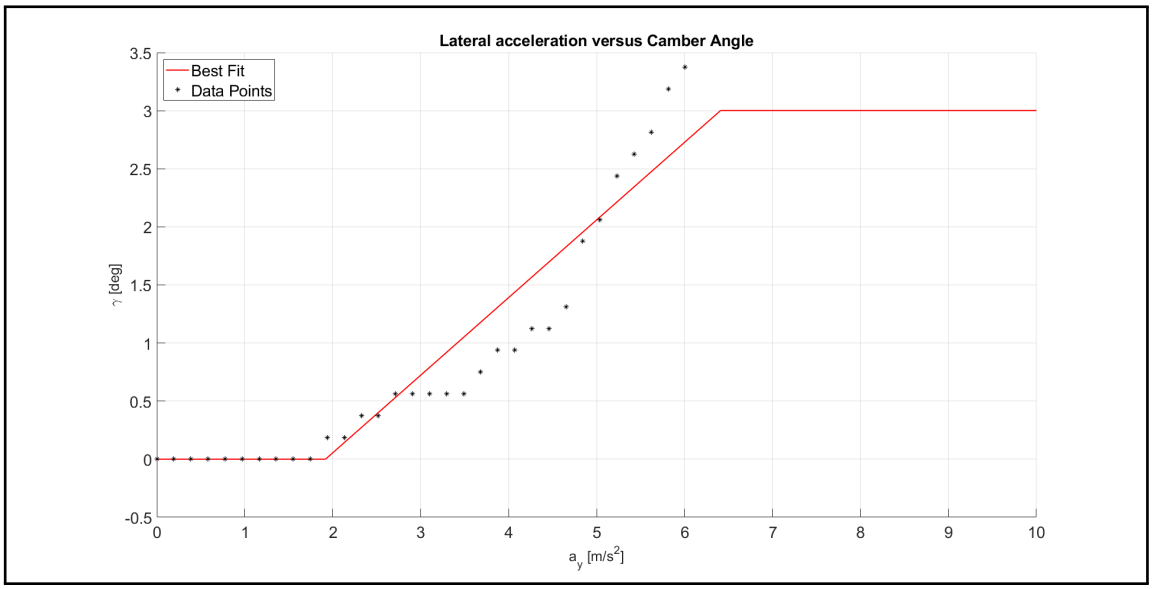

Figure 5.8: Lateral Acceleration versus Camber Angle

Table 5.2: Goodness of Fit Parameters

Goodness of fit Parameter	Parameter Value
SSE	1.845
R-square	0.848
Adjusted R-square	0.8227
RMSE	0.5545

controller uses a lookup Table with the information in Figure 5.8 as the input to the simulation. The advantage of using a lookup Table is that it is numerically efficient and will be beneficial in real world implementations. The initial testing indicated that with a non-linear relationship between the lateral acceleration and the camber angle, instabilities in the simulation arose, especially at high lateral accelerations.

5.2 Full-Vehicle Simulations with Camber Controller

Now that the camber controller is setup, the full vehicle camber-controlled simulations can commence. The camber control algorithm is implemented on the full-vehicle model with a simple lookup Table. The camber angle of both the front and the rear wheels are being changed equally ($\gamma_L = \gamma_R$). The camber angle is limited to negative values only ($\gamma \leq 0°$). The limiting factors for the camber-controlled simulations is:

$$-3.5° \leq \gamma \leq 0° \tag{5.8}$$

With the limiting factors defined, the simulation parameters are outlined in Table 5.3. The simulations with the camber controller implemented will be compared to a baseline, zero-camber model with the same simulation input parameters.

The camber controller is setup such that during a cornering manoeuvre, albeit a CR or

Table 5.3: Camber Controlled Vehicle Simulation Parameters

Type of Manoeuvre	**Vehicle Speed** [Kph]	**Radius of Curve** [m]
DLC	40	N/A
	50	N/A
	60	N/A
	70	N/A
	80	N/A
CR	40	50
		100
	50	50
		100
	60	50
		100
	70	100
	80	100

DLC manoeuvre, the friction power produced by the tyre road contact, should be reduced, or kept the same as for a zero-camber case. To check this, the percentage of friction power below the zero-camber baseline value is calculated. The percentage below zero indicates the percentage of data samples in the data set of the total friction energy, which has an energy value that is either reduced or remains zero. This data was gathered by comparing the friction energy values to those of the baseline zero camber cases. In other words, if the data set has 1000 data samples and 700 data samples represent friction energy values that are either lower or equal to zero when compared to the baseline zero camber case. These 700 data point therefore represent that 70% of the data samples have been reduced.

The percentage data samples reduced is graphically depicted in Figure 5.9, for the simulation experiments listed in Table 5.1, for the constant curve simulations at constant camber angles.

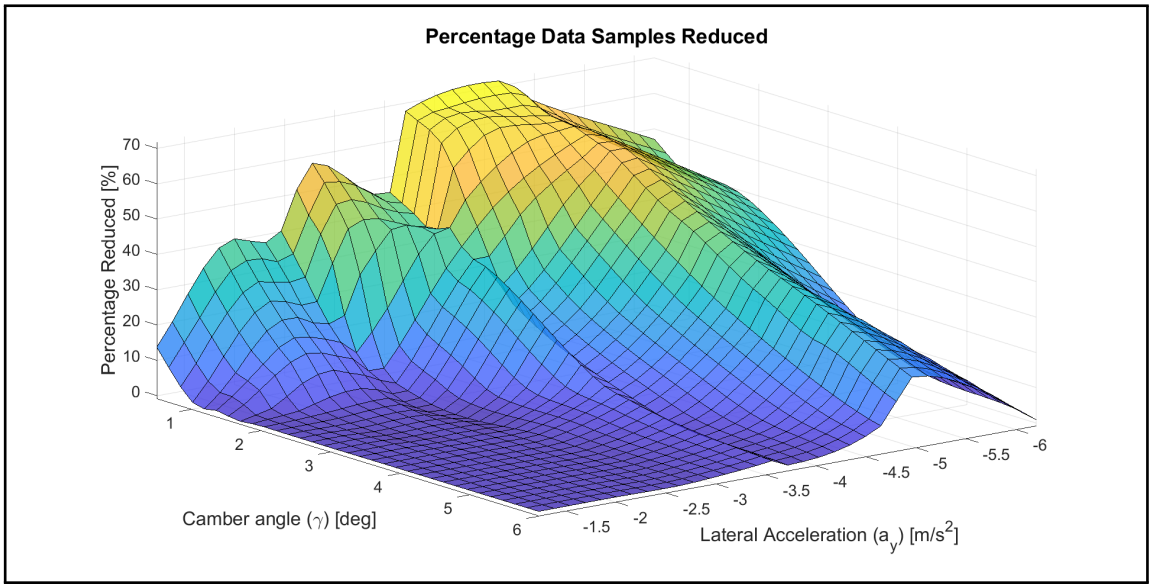

Figure 5.9: Percentage of Friction Power Data Samples Reduced

Figure 5.9 shows that the lower camber angle range ($\gamma \leq 4°$) demonstrates the highest

percentage of friction power reduced. The higher the lateral acceleration value, the greater the percentage of friction power reduced. However, the upper limit of lateral acceleration ($a_y > -5m/s^2$) shows a drop off in the percentage saved. Therefore, the camber controller should theoretically show an increase in the percentage friction power reduced.

The results from the camber-controlled simulation are compared to the results from the simulation experiments, discussed in the previous section. The data can be compared because the same vehicle speed and path was maintained for both sets of simulations. This comparison will therefore only be completed for the constant curve test. The comparison results are illustrated in Table 5.4.

Table 5.4: Comparison between Baseline and Camber Controlled Vehicle Simulations

Curve Radius [m]	**Vehicle Speed [Kph]**	**Percentage of Data Samples Reduced (Controlled) [%]**	**Maximum Lateral Acceleration $[m/s^2]$**
50	40	0	2.53
	50	76.64	3.93
	60	98.62	7.50
100	40	0	1.30
	50	0	2.04
	60	92.30	3.02
	70	87.24	4.11
	80	97.31	5.34

From the results in Table 5.4, with the camber controller implemented, the percentage of friction power reduced shows that in every case the controlled results are greater than for the uncontrolled cases (which are all 0 because no camber was induced). It is important to note that the percentage of friction power reduced is calculated by considering all values that reman identical or is less than that of the baseline values (no camber angle). Therefore, in Table 5.4, the cases that show a 0% reduction in friction power, actually indicate that the results were kept identical to the baseline value (i.e. no camber angle change). This is due to the lateral acceleration falling in the lower range of the controller input, illustrated by Figure 5.8. At lateral accelerations below $1.9m/s^2$, the camber controller keeps the camber angle equal to zero. This is because it was found that at lower lateral accelerations, the addition of camber does not result in any friction power saving, but increases the friction power developed in the tyres.

Further results from the camber controller will be discussed in two parts. The first will look at the results from CR simulations, and the second from DLC simulations.

5.2.1 Constant Radius Simulations

Some results from the simulations were depicted in Table 5.4, which already indicated a good increase in the percentage of friction power reduced. The next section will compare the results from implementing the camber controller, to the baseline simulation results (no camber). The expected outcome is that the camber controller should be able to decide as to when to change the camber angle, based on the lateral acceleration experienced by the CG of the vehicle. Therefore, at lower lateral accelerations, no camber angle should

be present, as we have seen that it negatively affects the friction power in the tyres. At higher lateral accelerations, the controller should change the camber accordingly, to reduce the friction power in the tyres. The results from the camber-controlled simulations are illustrated in Table 5.5.

Table 5.5: Camber Controlled Constant Radius Simulation Results

Radius of Curve [m]	**Vehicle Speed [Kph]**	**Average Lateral Offset [m]**	**Percentage Saved [%]**	**Total Energy Saved [J]**
50	40	0	0	0
	50	0.0086	1.22	212.05
	60	0.0466	4.63	1.83E+03
100	40	0	0	0
	50	0	0	0
	60	0	-0.051	-4.74
	70	0.0068	1.05	200.8014
	80	0.0233	2.98	1.18E+03

From the results, if the speed increases, the lateral offset increases. Resultantly, as mentioned before, the steering angle can be reduced, which reduces the amount of power required to steer the vehicle. The percentage friction power saved, illustrated in Table 5.5, indicates the total friction power reduction, as a percentage value. This directly corresponds to the actual total friction energy saving in Table 5.5. The percentage saved and the actual total friction energy saved shows significant savings, especially towards higher speeds. An example of the lateral offset for an entire simulation run is illustrated in Figure 5.10. An example of the difference between the steering angles for the controlled and uncontrolled cases are illustrated in Figure 5.11.

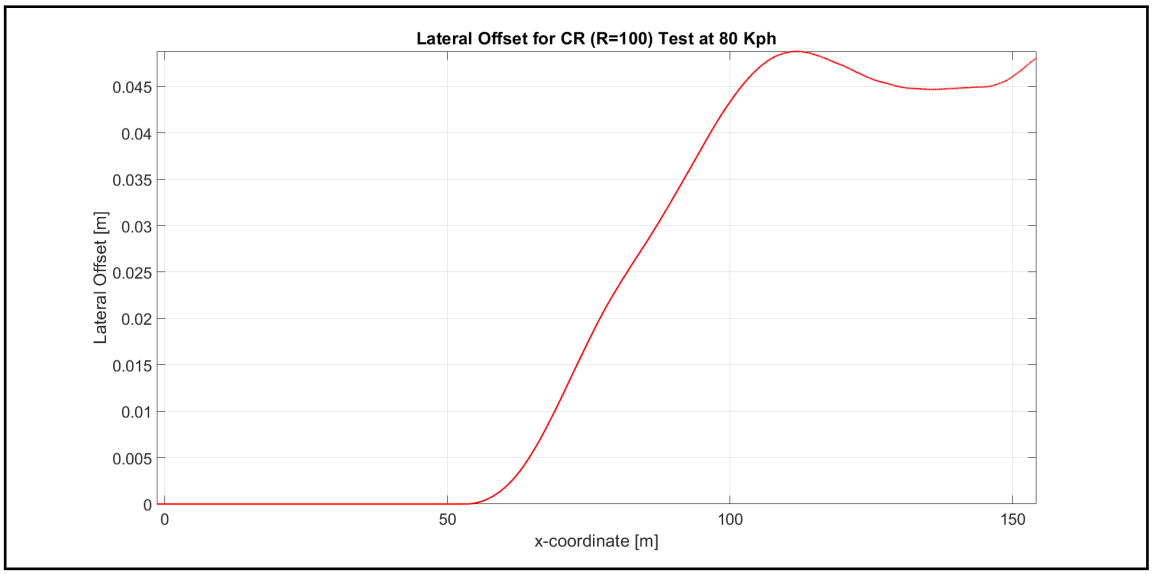

Figure 5.10: Lateral Offset for CR ($R = 100m$) Test at $80Kph$

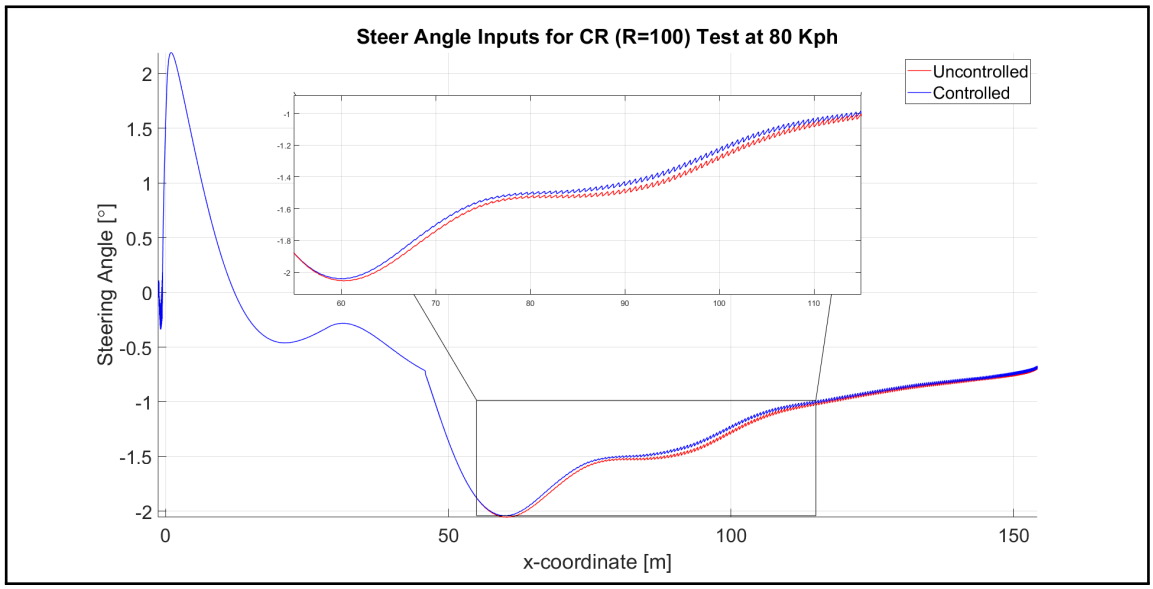

Figure 5.11: Steering Angle for Controlled and Uncontrolled CR Test at $80Kph$

In this case the average lateral offset of the CG is $0.0233m$ or 1.25% of the width of the vehicle. Here, the lateral offset is not as significant as in the previous discussion. This is due to the controller setting the camber angle equal to zero when small lateral acceleration is present, resulting in no lateral offset due to camber. However, when considering that the lateral offset will result in a smaller steering angle input required, then this value is significant. This difference between the steering angles for the controlled and the uncontrolled cases are graphically depicted in Figure 5.11. The differences are noticeable but still quite small.

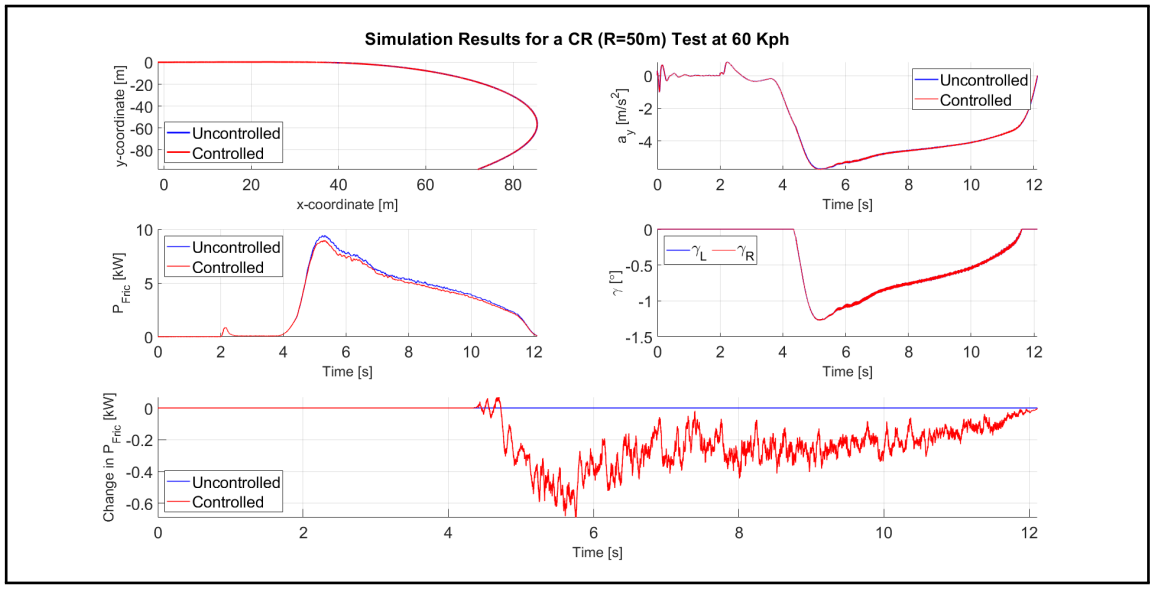

Figure 5.12: Simulation Results for a $R = 50m$ CR Test. (From top right clockwise: Lateral Acceleration, Camber Angle, Total Change in Friction Power, Total Friction Power on All Four Wheels & Vehicle path Followed)

Consider the case of $60Kph$ and a radius of $50m$, graphically depicted in Figure 5.12. We observe the percentage of friction power saved to be 4.63%. This saving is significant, especially when considering the lifetime of the vehicle. The corresponding energy saved

is $1830J$, for the 13 second simulated manoeuvre. From the comparison in Figure 5.12, it can be seen that despite a single overshoot in the change in friction power graph at $\approx 4.5sec$, the majority of the values are either equal to or less than the baseline values (no camber). For this case, the percentage reduced was 98.62%. This means that 98.62% of the data points representing the total friction power on all four wheels have been reduced when compared to the baseline simulation. From the camber angle graph, it is shown that the camber angle on the left and the right side are identical.

Therefore, with regards to the discussion of the simulation results for the constant radius test, the expected outcome was reached. The controller only changed the camber angle when there are savings to be made, otherwise the camber was kept at zero.

5.2.2 Double Lane Change Manoeuvre

The constant radius tests showed impressive results from the simulations with the camber controller implemented. However, the investigation with a Double Lane Change test will also be considered. The DLC manoeuvre is usually used to assess the lateral dynamics of a vehicle. However, for the purposes of investigating the power saving in electric vehicle, the DLC manoeuvre will provide some insight into the behaviour of the camber controller in extreme handling situations. The DLC tests will provide insight into how the camber controller behaves when a rapid change in the lateral acceleration is experienced.

The expected outcome is like that of the CR tests. The controller should make the required camber adjustments at all speed ranges and result in a reduction in the total friction power in the tyres. The results from the camber-controlled simulations are illustrated in Table 5.6.

Table 5.6: Camber Controlled Double Lane Change Simulation Results

Vehicle Speed [Kph]	**Lateral Offset [m]**	**Percentage Below 0 [%]**	**Percentage Saved [%]**	**Total Energy Saved [J]**
40	0	99.82	-2.07E-04	-0.0059
50	0	95.48	0.83	37.30
60	0	98.85	0.70	42.62
70	0	96.58	1.09	78.31
80	0.0069	92.02	4.41	518.23

Due to the varying lateral acceleration during a DLC manoeuvre (from positive to negative), the lateral offset looks a bit different to that of the CR test. The lateral offset changes between positive and negative values. But when considering the layout of the path, the lateral offset of a DLC manoeuvre at $80Kph$, illustrated in Figure 5.13, is representative of a lateral offset that will require less steering angle input from the driver. This phenomenon is graphically depicted in Figure 5.13 and 5.14.

However, the average lateral offset will have to be computed with the absolute of the lateral offset. The calculated average lateral offset for the DLC manoeuvre is negligibly small for all speed ranges, as illustrated in Table 5.6. Resultantly, the reduction in the steering angle required is significantly small. However, as shown in Figure 5.14, the steering angle difference is noticeable.

The simulation results in Table 5.6 indicate that as the speed of the vehicle is increased,

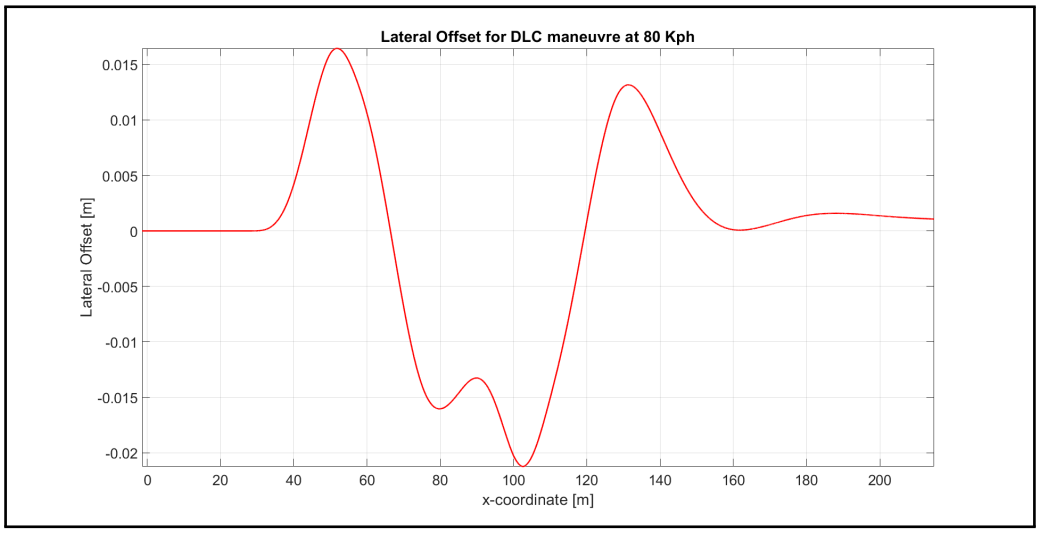

Figure 5.13: Lateral Offset for DLC Manoeuvre at $80Kph$

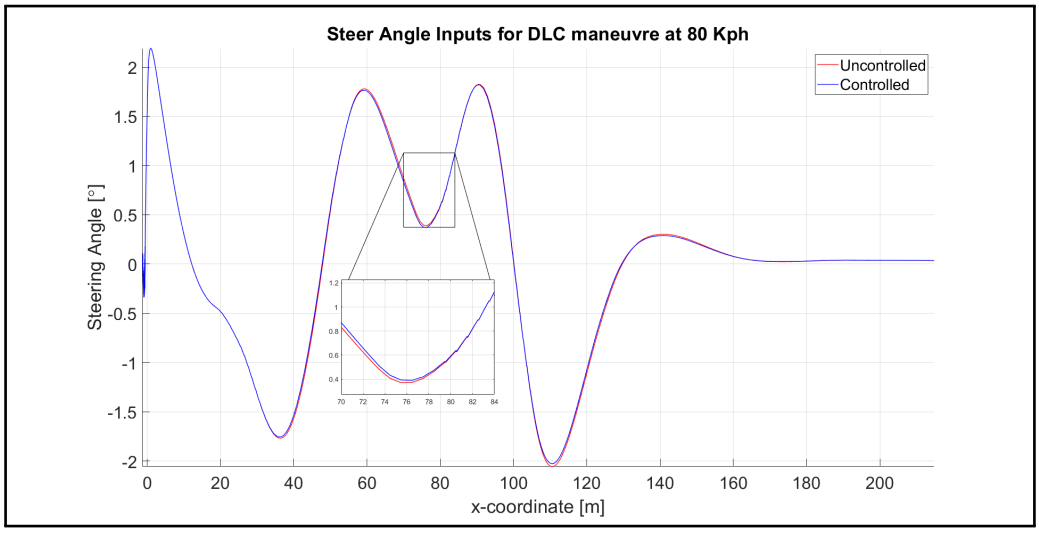

Figure 5.14: Steering Angle for Controlled and Uncontrolled DLC Manoeuvre at $80Kph$

the percentage of friction power saved increases. There is however a significant spike between $70Kph$ and $80Kph$. At $80Kph$ the percentage saved is 4.41%, which means that not only does the lateral offset indicate that there are no noticeable effects on the position of the vehicle during the DLC manoeuvre, but there is a noticeable improvement in the energy losses at the same time. The total energy saved during the simulation was $518.23J$. This value is significant when considered over the entire lifespan of the vehicle. A DLC manoeuvre is not the type of manoeuvre that will be done daily, but it is good to know that the controller will behave properly in these types of situations. The results from the simulation of a DLC manoeuvre at $80Kph$ is graphically depicted in Figure 5.15.

From the simulation results in Figure 5.15, it is clear that the camber controller behaved exactly as anticipated. The change in friction power graph illustrates that the camber controller succeeded in maintaining or reducing the friction power over the simulation period. There are slight overshoots, but this can be attributed to the initial change in the camber angle, resulting in a sudden spike in the friction power produced in the tyres.

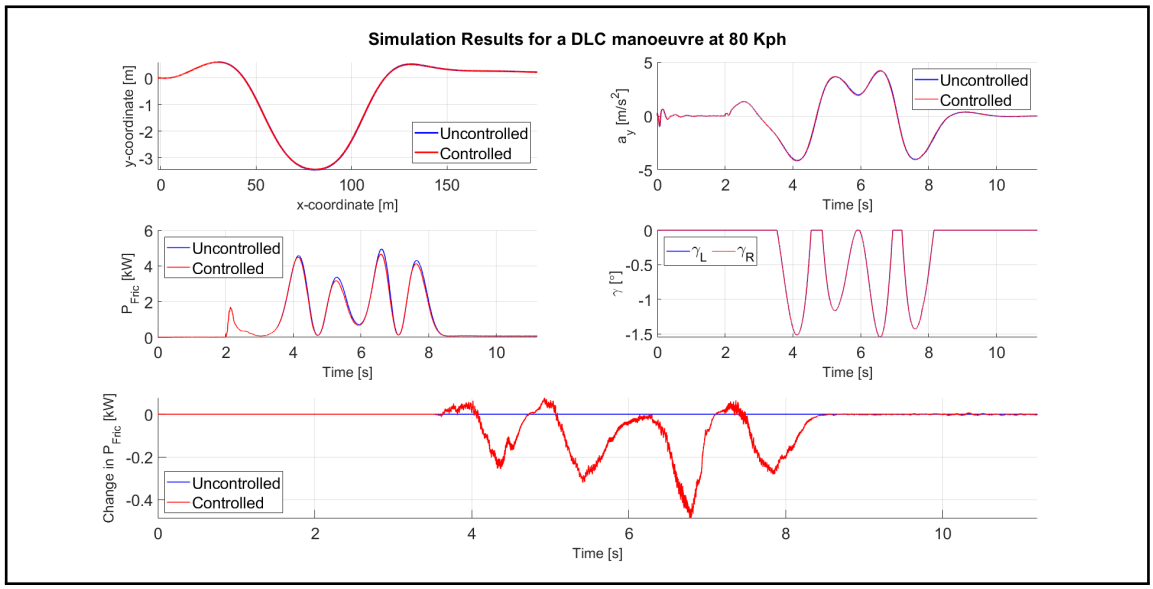

Figure 5.15: Simulation Results for a DLC manoeuvre at 80Kph. (From top right clockwise: Lateral Acceleration, Camber Angle, Total Change in Friction Power, Total Friction Power on All Four Wheels & Vehicle path Followed)

5.3 Conclusion

In this chapter, the process of designing and implementing a simple camber controller on a fully validated full-vehicle ADAMS model was executed. The process started with a large array of simulations based on a constant curve test. The simulation results from these tests were used to determine the best relationship between the lateral acceleration and the camber angle of the vehicle. The optimal values for the lateral acceleration versus the camber angles was illustrated in 5.8. With regards to the optimal lateral acceleration versus camber angle values, a linear estimate was done to best represent all the data. A linear relationship was chosen such that any instabilities are reduced or eliminated.

From the actual simulation outcomes, it was concluded that the camber control method was able to reduce the friction power loss in the tyres of the vehicle. Consequently, it was noticed that with the addition of camber, the lateral offset of the vehicle with respect to the baseline values was improved in certain cases. Thus, indicating that the steering angle input can be reduced. With a smaller steering input, the tyres would have to overcome smaller loads to steer the vehicle. Thus, the possibility of reducing the power required to steer the vehicle as well. For future work it is recommended to extend the driver controller to consider the inputs from the camber controller and adjust accordingly. This will ensure full coherence between the two controllers resulting in the optimal trade-off between lateral dynamics and energy saving in the vehicle tyres.

Overall, the development and the implementation of the camber control algorithm showed impressive results with good savings for both the CR test and the DLC manoeuvre.

Chapter 6

Conclusions and Recommendations

6.1 Conclusion

This study set out to investigate the possibility of using the camber angle of a vehicle to reduce the power losses during dynamic handling simulations. Several new control methods have been surfacing in recent years, with the rapid increased popularity for electrically propelled vehicles. These control strategies are mostly aimed at improving the vehicle dynamics or ride comfort and are generally represent by a simplified or linearized vehicle model. Recently, interest with regards to camber control have gained some momentum. The control strategies currently available however represent a more simplified and linearised vehicle model with a simple approach to camber control. The goal for this project was to investigate and develop a camber control system that is based on a highly non-linear multi-body dynamics full-vehicle model. The control system was developed to be used as a tool to investigate the possibility of reducing the power losses in a vehicle, without compromising the vehicle's lateral dynamics.

A MSC ADAMS/VIEW model of a drum test rig at the University of Pretoria was developed to simulate the behaviour of the tyre at various slip angles and camber angles. This model was created to simulate and understand the behaviour of the fully validated Pirelli Scorpion tyre and the corresponding FTire simulation model. From the simulations completed on the drum model, it was found that by introducing a camber angle on a vehicle's tyre during cornering, could result in a reduction in the power losses in the tyre contact patch. The results indicated that to maintain a certain lateral force in the tyre, various combinations of camber angle and slip angle could be used. It was concluded that at a certain lateral force on a tyre, the steering angle input could be reduced by introducing more camber. This could prove beneficial in reducing the power required to overcome the tyre loads when steering the vehicle.

A simple control algorithm was developed on a Land Rover Defender 110 TDi SUV. This vehicle was chosen because the University of Pretoria have developed a fully non-linear multi-body dynamics full-vehicle model that could be used for simulating the real-world behaviour of the Land Rover Defender. The Land Rover Defender was developed in MSC ADAMS/VIEW and accurately captures the lateral and vertical dynamics of the vehicle. The ADAMS/VIEW model has been experimentally validated in various other

projects at the University of Pretoria. Therefore, making it a great tool to use in the investigation for this study. The full-vehicle model uses the highly non-linear FTire tyre software to accurately simulate the tyre dynamics. The MSC ADAMS/VIEW full-vehicle model was adjusted to include a method for actively changing the camber angle, without compromising the suspension geometry. The model was adapted to include a camber control algorithm.

A cross validation approach was taken to provide the necessary confidence in the MSC ADAMS/VIEW full-vehicle model. The validation data already gathered by previous students was used to validate the newly developed full-vehicle camber model. The cross-validation was performed on an ISO 3888:2018 severe double lane change manoeuvre. The simulation results were compared to the experimental results gathered by previous students. The results from the cross validation indicated that the full-vehicle model with camber provisions provides the necessary confidence to produce valuable and reliable simulation results.

A simple control algorithm was developed to test the theory that camber angle control can be used to reduce tyre power losses. The camber control algorithm used the best relationship between the lateral acceleration and camber angle of the vehicle, to provide the best possible camber angles at various lateral accelerations.

Both constant radius tests and severe double lane change manoeuvres were used to test the efficiency of the camber controller. From the results it was concluded that for both the CR test and the DLC manoeuvre, the camber controller was able to reduce the power losses in the tyres and improve the lateral offset between the controlled vehicle path and the baseline (no camber) vehicle path. The improved lateral offset indicates that the steering angle input can be reduced when the camber controller is implemented on the vehicle model. Therefore, resulting in the possibility of reducing the power required to steer the vehicle.

6.2 Recommendation

There are multiple aspects which could improve the efficiency and accuracy of the camber control algorithm and the full-vehicle, MSC ADAMS/VIEW camber model. These improvements include:

- Validating the FTire tyre model for higher camber angles. Camber angles higher than four degrees would be beneficial for future studies. The current Pirelli tyre model was fully validated up to four degrees of camber.
- Validating the FTire tyre model for dynamic simulations, currently only the stiffness at camber angle is validated. The validation for dynamic simulations should validate the friction and power losses in the tyre.
- Fully testing the vehicle tyre on the drum test rig to validate the correlation between the simulated tyre drum model and the actual tyre drum model. This will enable us to understand and validate the behaviour of the tyre at higher camber angles.
- The development of a highly non-linear camber control algorithm which can handle very large lateral acceleration, with an improved control algorithm. It will be

beneficial to develop a control system that takes multiple inputs from the vehicle to make the best possible decision for what the camber angle should be.

- Developing a controller that works in combination with the non-linear driver controller on the full-vehicle model which can adjust the driver's control inputs, based on the camber controllers' inputs.
- Designing and developing a quarter car model to simulate the behaviour of a vehicle under various driving conditions. Experimentally validating the quarter car model with the use of the tyre test trailer and actuators for controlling the camber angle.

The performance of the camber controller in combination with the driver controller might be improved by implementing and performing these recommendations.

Bibliography

Arrive Alive (2019), 'Rollover crashes, crash reconstruction and safer driving'.
URL: *https://www.arrivealive.co.za/Rollover-Crashes-Crash-Reconstruction-and-Safer-Driving*

Beckers, C. J., Besselink, I. J. and Nijmeijer, H. (2020), 'Assessing the impact of cornering losses on the energy consumption of electric city buses', *Transportation Research Part D: Transport and Environment* **86**, 102360.
URL: *https://www.sciencedirect.com/science/article/pii/S1361920920305472*

Bosch, H.-R. B. (2016), Ftire model parameterization and validation of an all-terrain suv tyre.

Botha, T. R. (2011), 'High speed autonomous off-road vehicle steering'.
URL: *http://hdl.handle.net/2263/29665*

Cronjé, P. and Els, P. (2010), 'Improving off-road vehicle handling using an active anti-roll bar', *Journal of Terramechanics* **47**(3), 179 – 189.
URL: *http://www.sciencedirect.com/science/article/pii/S0022489809001207*

Dassault Systems (2020), 'Dassault solidworks'.
URL: *https://www.solidworks.com/*

Davari, M. M. (2017), Exploiting over-actuation to reduce tyre energy losses in vehicle manoeuvres, PhD thesis, KTH, Vehicle Dynamics. QC 20170524.

Edrén, J. (2014), Motion modelling and control strategies of over-actuated vehicles.

Els, P., Theron, N., Uys, P. and Thoresson, M. (2007), 'The ride comfort vs. handling compromise for off-road vehicles', *Journal of Terramechanics* **44**(4), 303 – 317.
URL: *http://www.sciencedirect.com/science/article/pii/S0022489807000213*

Gerotek (2020), 'Gerotek'.
URL: *https://www.armscor.co.za/?page*$_i d = 3967$

Ghazaly, N. and Moaaz, A. (2014), 'The future development and analysis of vehicle active suspension system', *IOSR Journal of Mechanical and Civil Engineering (IOSR-JMCE)* **11**, 19–25.

Gillespie, T. (1992), 'Fundamentals of vehicle dynamics'.

Gipser, M. and Hoffmann, G. (2016), *FTire-Flexible Structure Tire Model*, 3 edn, Cosin.
URL: *https://www.cosin.eu/support/documentation/*

González, R. G. (2019), 'Camber angle'.
URL: *http://www.drawfolio.com/en/portfolios/ramongarciagonzalez/picture/50118*

Hamersma, H. H. A. (2014), 'Longitudinal vehicle dynamics control for improved vehicle safety'.
URL: *http://hdl.handle.net/2263/40829*

Hirano, Y. (2012), Integrated vehicle control of an in-wheel-motor vehicle to optimize vehicle dynamics and energy consumption, *in* 'Proceedings of the 10th World Congress on Intelligent Control and Automation', pp. 2335–2339.

Insurance Institute for Highway Safety (IIHS) (2018), 'Fatality facts 2018, passenger vehicle occupants'.
URL: *https://www.iihs.org/topics/fatality-statistics/detail/passenger-vehicle-occupantsrollover*

ISO3888 (2018), International standard iso 3888-1975: Road vehicles – test procedure for a severe lane-change manoeuvre, Technical report, International Organisation for Standardisation. ISO/TR 3888-2018.

Kavitha, C., Shankar, S. A., Karthika, K., Ashok, B. and Ashok, S. D. (2019), 'Active camber and toe control strategy for the double wishbone suspension system', *Journal of King Saud University - Engineering Sciences* **31**(4), 375–384.
URL: *https://www.sciencedirect.com/science/article/pii/S1018363917302799*

Loveday, E. (2013), 'leaf-skidpad'.
URL: *https://insideevs.com/photo/3922623/range-increasing-low-rolling-resistance-tires-falling-out-of-favor-with-drivers/*

Mathworks (2020), 'Products and services'.
URL: *https://www.mathworks.com/products.html?s$_t$id = gn$_p$s*

Merkx, L. (2004), *Overturning moment analysis using the flat plank tyre tester*, DCT rapporten, Technische Universiteit Eindhoven. DCT 2004.078.

MSC Software (2013), 'Help document for adams/tire'.
URL: *https://simcompanion.mscsoftware.com/infocenter*

Oosten, J. (2011), *How to get tire model parameters*, MSC Software Office, Munich, Germany.

Pacejka, H. B., Bakker, E. and Lidner, L. (1989), A new tire model with an application in vehicle dynamics studies, *in* 'Autotechnologies Conference and Exposition', SAE International.
URL: *https://doi.org/10.4271/890087*

Park, S.-J. and Sohn, J.-H. (2012), 'Effects of camber angle control of front suspension on vehicle dynamic behaviors', *Journal of Mechanical Science and Technology* **26**.

Peenze, A. J. (2020), Model predictive suspension control on off-road vehicles, Master's thesis, University of Pretoria.

Shyrokau, B., Savitski, D. and Wang, D. (2014), Influence of active subsystems on electric vehicle behavior and energy characteristics, Vol. 1.

Smith, N. D. (2004), 1 dynamics understanding parameters influencing tire modeling.
URL: *https://www.semanticscholar.org/paper/1-Dynamics-Understanding-Parameters-Influencing-Smith/9e6e6f9b1bf0a0c8f52a641a0a2f22b22c83d2f2*

Stallmann, M. J. (2014), Tyre model verification over off-road terrain.
URL: *https://www.semanticscholar.org/paper/Tyre-model-verification-over-off-road-terrain-Stallmann/6762e70aba5712a8d7b2e229888b24d005d22290*

Sun, P., Stensson Trigell, A., Drugge, L. and Jerrelind, J. (2020), 'Energy-efficient direct yaw moment control for in-wheel motor electric vehicles utilising motor efficiency maps', *Energies* **13**(3), 593.
URL: *http://dx.doi.org/10.3390/en13030593*

Sun, P., Trigell, A., Drugge, L., Jerrelind, J. and Jonasson, M. (2018), 'Exploring the potential of camber control to improve vehicles' energy efficiency during cornering', *Energies* **11**, 724.

Thoresson, M., Uys, P., Els, P. and Snyman, J. (2009), 'Efficient optimisation of a vehicle suspension system, using a gradient-based approximation method, part 1: Mathematical modelling', *Mathematical and Computer Modelling* **50**(9), 1421 – 1436.
URL: *http://www.sciencedirect.com/science/article/pii/S0895717709002520*

Uil, R. T. (2008), Tyre models for steady-state vehicle handling analysis.
URL: *https://www.semanticscholar.org/paper/Tyre-models-for-steady-state-vehicle-handling-Uil/38179b98f93b7fdfb799cc82a6d51dd9ba6d3801*

Uys, P., Els, P. and Thoresson, M. (2007), 'Suspension settings for optimal ride comfort of off-road vehicles travelling on roads with different roughness and speeds', *Journal of Terramechanics* **44**(2), 163 – 175.
URL: *http://www.sciencedirect.com/science/article/pii/S0022489806000474*

Wright, K. R. S. (2017), The effects of age and wear on the stiffness properties of an suv tyre.
URL: *http://hdl.handle.net/2263/62196*